Developing Raman microscopy as a routine spectroscopic technique for morphology and microstructure characterization of plastics

Vom Fachbereich Chemie
der Technischen Universität Darmstadt
zur
Erlangung des akademischen Grades eines

Doktor-Ingenieurs (Dr.–Ing.)

genehmigte
Dissertation

vorgelegt von

M. Tech. Abhishek Sanoria
aus Noida, Indien

Referent: **Prof. Dr. Matthias Rehahn**
Korreferent: **Prof. Dr. Markus Busch**
Tag der Einreichung: 26. September 2016
Tag der mündlichen Prüfung: 12. December 2016

Darmstadt 2016
D 17

To my Mom, Dad and Sister

For all the support and encouragement

Acknowledgements

It is a pleasure to thank all the people who have accompanied and supported me throughout this scientific work. I am honoured to pay my sincere thanks to my research supervisor Prof. Dr. Matthias Rehahn for giving me the opportunity to work in his research group.

I most gratefully record that the work imbibed in this project is solely due to deep insight and vision of my guide and supervisor, Dr. Robert Brüll. Besides being morally supportive all through the execution of my work, his critical discussions and meticulous approach towards my experimental work have not only proved valuable for the project but they, I am sure, will go a long way to mold my future career and for this I shall ever remain indebted.

I acknowledge Dr. Daniel Ulbricht for his excellent guidance which was instrumental for the success of this research.

I would like to express my gratitude to Karsten Rode, Dr. Tobias Schuster, Dr. Tibor Macko, Dr. Frank Malz and Dr. Subin Damodaran for their friendship, moral support and scientific contributions during this study. Lastly, I would like to thank all the past and present colleagues at Fraunhofer LBF for the pleasant working atmosphere and making my stay in Germany enjoyable.

Most importantly, I am ever so grateful to my dearest Mom, Dad and Sister for their moral support, endless love, trust, and understanding during my study. Their motivational nature and enthusiasm in both good and difficult times will remain in my memory. Without them this would not be possible.

Diese Arbeit wurde unter der Leitung von Herrn Prof. Dr. Matthias Rehahn und Dr. Robert Brüll am Bereich Kunststoffe des Fraunhofer LBF (zuvor DKI) in der Zeit vom August 2013 bis zum June 2016 durchgeführt.

This study is a result of the work carried out from August 2013 to June 2016 at Plastic Division, Fraunhofer LBF under the supervision of Prof. Dr. Matthias Rehahn and Dr. Robert Brüll.

Publication List

Journal articles

1. **'Raman spectroscopy as a non-destructive tool to quantify the comonomer content in ethylene/1-olefin copolymers'**

Abhishek Sanoria, Tobias Schuster and Robert Brüll

Analytical Methods. **2015**, 7, 5245-5253

2. '**Monitoring crosslinking inhomogeneities in ethylene vinyl acetate photovoltaic encapsulants using Raman microscopy'**

Abhishek Sanoria, Daniel Ulbricht, Tobias Schuster and Robert Brüll

RSC Advances. **2015**, 5, 93522-93529

3. '**Investigating the morphological variations due to processing and thermo-mechanical treatment of polypropylene using Raman microscopy'**

Abhishek Sanoria, Subin Damodaran, Tobias Schuster and Robert Brüll

Macromolecular Chemistry and Physics. **2016**, Accepted Manuscript

4. '**Studying the Interaction between Porous Graphitic Carbon and Polyethylene using Raman Spectroscopy'**

Kavamani Nagar Prabhu, Abhishek Sanoria, Dieter Fischer, Robert Brüll, Klaas Remerie, Jacques Tacx, Priya Garg and Anton Ginzburg

Journal of Raman Spectroscopy. **2016**, Submitted Manuscript

5. **'Ageing study of different types of long-term pressure tested PE pipes by IR-microscopy'**

Raquel Maria, Karsten Rode, Tobias Schuster, Guru Geertz, Frank Malz, Abhishek Sanoria, Harald Oehler, Robert Brüll, Mirko Wenzel and Kurt Engelsing

Polymer. **2015**, 61, 131-139

6. **'Monitoring the effect of chlorine on the ageing of polypropylene pipes by infrared microscopy'**

Subin Damodaran, Tobias Schuster, Karsten Rode, Abhishek Sanoria, Robert Brüll, Mirko Wenzel and Martin Bastian

Polymer Degradation and Stability. **2015**, 111, 7-19

7. **'Measuring the orientation of chains in polypropylene welds by infrared microscopy: A tool to understand the impact of thermo-mechanical treatment and processing'**

Subin Damodaran, Tobias Schuster, Karsten Rode, Abhishek Sanoria, Robert Brüll and Neda Stöhr

Polymer. 2015, 60, 125-136

8. **'Determining the interaction of polymer additives with graphitic fillers using Raman spectroscopy and NMR studies'**

Abhishek Sanoria, Frank Malz, Tobias Schuster, Robert Brüll

2016 (In preparation)

Conference posters

1. **'Raman spectroscopy as a non-destructive tool for additive analysis in polyolefins'**

Abhishek Sanoria, Tobias Schuster, Subin Damodaran and Robert Brüll

5th International Conference on Polyolefin Characterization (ICPC), Valencia, Spain, 23rd Sept. 2014

2. **'Raman spectroscopy as a tool to investigate micro defects in polymers'**

Abhishek Sanoria, Tobias Schuster, Subin Damodaran and Robert Brüll

11th Confocal Raman Imaging Symposium, Ulm Germany, 29th Sept. 2014

3. **'Studying the morphology of polypropylene extruded materials using Raman microscopy'**

Abhishek Sanoria, Tobias Schuster, Subin Damodaran and Robert Brüll

8th International Conference on Advanced Vibrational Spectroscopy, Vienna Austria, 12-17th July 2015

"…I cannot teach anybody anything, I can only make them think"

Socrates

Contents

Table of Contents

Acknowledgements iii
Publication List v
Contents ix
1. Summary in German 15
2. Introduction and Preface 18
3. Characterization of polymers using spectroscopic techniques 21
3.1 NMR Spectroscopy: 22
3.1.1 NMR of polymers 24
3.2 FT-IR spectroscopy 25
3.2.1 FT-IR ATR 26
3.2.2 FT-IR in transmission mode 26
3.3 Raman spectroscopy 29
3.3.1 Raman spectroscopy in polymer analytics 31
3.3.2 Confocal Raman microscopy 32
3.3.3 TrueSurface® chromatic sensor for Raman measurements 33
3.3.4 Raman microscopic analysis of polymers (fluorescence and sample burning) 36
4. Theoretical Consideration 38
4.1 Determining the comonomer content in ethylene-1-olefin copolymers using Raman spectroscopy 39
4.2 Determining the percentage crosslinking in EVA photovoltaic modules using Raman microscopy 42
4.2.1 Chemical Methods for determining Xc 45
Soxhlet Extraction 45
4.2.2 Thermal Methods for determining Xc 45
4.2.3 Spectroscopic methods for determining Xc 46
4.3 Investigating the morphological variations due to processing and thermo-mechanical treatment of polypropylene using Raman microscopy 48
4.3.1 Morphology of PP 50
4.3.2 Applications of polypropylene 55
4.3.3 Processing and welding of PP and the effect of the morphology and X_C . 56
5. Experimental Section 59
5.1 Determining the comonomer content in ethylene-1-olefin copolymers using Raman spectroscopy 59
5.1.1 Samples: 59
5.1.2 Experimental parameters 60
5.2 Determining the percentage crosslinking in EVA Photovoltaic modules using Raman microscopy 61
5.2.1 Samples 61
5.2.2 Experimental Parameters 62

5.3 Investigating the morphological variations due to processing and thermo-mechanical treatment of polypropylene using Raman microscopy 64
5.3.1 Samples 64
5.3.2 Experimental Parameters 64
6. Results and Discussions 67
6.1 Determining the comonomer content in ethylene-1-olefin copolymers using Raman spectroscopy 67
6.1.1 Quantification of the comonomer content in Copolymers of Ethylene with Cyclic Olefin Copolymers (COC) 80
6.1.2 Conclusions 81
6.2 Determining the percentage crosslinking in ethylene vinyl acetate photovoltaic encapsulants using Raman microscopy 83
6.2.1 Conclusions 99
6.3 Investigating the morphological variations due to processing and thermo-mechanical treatment of polypropylene using Raman microscopy 100
6.3.1 Conclusions 115
7. Summary 117
8. Bibliography 121
Curriculum Vitae 130
Eidesstattliche Erklärung 132
Erklärung 133

Abbreviations	
PE	Polyethylene
PP	Polypropylene
LLDPE	Linear Low Density Polyethylene
PP-H	Polypropylene homo polymer
PP-R	Polypropylene random polymer
iPP	Isotactic polypropylene
aPP	Atactic polypropylene
sPP	Syndiotactic polypropylene
α	Alpha
β	Beta
γ	Gamma
IR	Infrared
ATR	Attenuated total reflectance spectroscopy
μFT-IR	Infrared microscopy
NMR	Nuclear Magnetic Resonance
DSC	Differential scanning calorimetry
PLM	Polarized light microscopy
PV modules	Photovoltaic modules
E_{BUT}	Ethylene/1-butene
E_{HEX}	Ethylene/1-hexene
E_{OCT}	Ethylene/1-octene
E_{OCTD}	Ethylene/1-octadecene
E_{NOR}	Ethylene/norbornene
XC	Percentage crosslinking
NU-100	N-N'-dicyclohexyl 2-6-naphthalene dicarboximide
AFM	Atomic force microscopy
SAXS	Small Angle X-Ray Scattering

WAXS	Wide angle X-Ray Scattering
PP-D_W	Two material welded system of PP-H and PP-R
Physical constants	
h	Planks constant
C_l	Velocity of light
Physical variables	
ν	Frequency
$\tilde{\nu}$	Wavenumber
A	Absorbance
I	Transmitted intensity
I_0	Incident intensity
ε	Molar absorption coefficient
c	Content
d	Path length
D	Dichroism
r	Chain axis
μ	Transition moment vector
α_T	Angle between the chain axis and the transition moment vector
θ	Angle between the preferred direction (Z axis) and the chain axis
A_{II}	Electric vector parallel to Z axis
$A_{\perp}$	Electric vector parallel to y axis
f	Hermans orientation function
f_F	Fraser's orientation function
z	Atomic charge
ΔH_f	Enthalpy of fusion
ΔH_f^0	Enthalpy of fusion of a sample with 100 % crystallinity

$\mathbf{X_c}$	Crystallinity
$\mathbf{K_\alpha}$	Content of α
$\mathbf{K_\beta}$	Content of β
ΔH_α	Enthalpy of fusion of α-phase
ΔH_β	Enthalpy of fusion of β-phase
$\mathbf{M_n}$	Number average molar mass
$\mathbf{M_w}$	Weight average molar mass
B	Birefringence
ΔE	Energy difference between two excited states in NMR
γ	Gyromagnetic ratio
B	Strength of magnetic field
P	Polarization
α*	Molecular (dipole) polarizability
λ	Wavelength of light
$\boldsymbol{\alpha_c}$	relative fraction of segments present in the orthorhombic phase of PE
$\boldsymbol{\alpha_a}$	relative amount of segments forming the liquid like amorphous phase of PE
$\boldsymbol{\alpha_b}$	The interfacial phase in PE
$\mathbf{M_1}$	Mass of sample in Soxhlet extraction
$\mathbf{M_2}$	Mass of residue in Soxhlet extraction
ΔHo	Enthalpy of a non-crosslinked sample of EVA
ΔHs	Enthalpy of the cross-linked sample of EVA
XC	Percentage crosslinking
$\mathbf{XC_{SE}}$	Percentage crosslinking determined through Soxhlet extraction
$\mathbf{XC_{DSC}}$	Percentage crosslinking determined through DSC
$\mathbf{XC_R}$	Percentage crosslinking determined through

	Raman microscopy
I_{BR}	Band ratio 2934 cm^{-1}/2885 cm^{-1} in the Raman spectrum of EVA
MMT	Million metric tonnes

1. Summary in German

Raman-Spektroskopie bietet gegenüber anderen spektroskopischen Methoden wie Kernspinresonanz- und Infrarotspektroskopie potentielle Vorteile, die sich vor allem durch minimale Probenvorbereitung und schnelle Messzeiten äußern. In Kombination mit einem Mikroskop (Raman-Mikroskopie) stellt die erhöhte Auflösung einen zusätzlichen Vorteil gegenüber der Infrarot-Mikroskopie da. Die Aspekte der Probenvorbereitung und Messzeiten wurden ausgenutzt, um den Comonomergehalt in Ethylen / 1-Olefin-Copolymeren zu quantifizieren. In der vorliegenden Arbeit wird der Aspekt der räumlichen Auflösung für vernetzte Ethylen / Vinylacetat (EVA) Laminate und Schweißnähte zwischen Polypropylen (PP) untersucht. Die Ergebnisse sind im Folgenden zusammengefasst:

Die Quantifizierung des Comonomergehaltes in Ethylen/1-Olefin-Copolymeren ist wichtig, um Struktur↔ Eigenschaftsbeziehungen zu erarbeiten und Proben eindeutig zu identifizieren. Für diese Zwecke wird häufig die Kernspinresonanzspektroskopie eingesetzt. Quantitative Bestimmungen erfordern jedoch erhebliche Mengen an Probe, was eine Einschränkung in Fällen darstellt, in denen nur begrenzte Menge des Analyten verfügbar sind, wie beispielsweise bei Fraktionen der Flüssigkeitschromatographie oder in der Forensik. In dieser Arbeit wurden die experimentellen Bedingungen für die Raman-Spektroskopie entwickelt, um den Comonomergehalt in Copolymeren von Ethylen mit 1-Olefinen, die von 1-Hexen bis zu 1-Octadecen reichen. Mit zunehmendem Comonomergehalt zeichnet sich eine kombinierte Wirkung aus der Abnahme des Ethylengehaltes und der damit einhergehenden Veränderung in der Phasenzusammensetzung des Polyethylens und der zusätzlichen Streuung der Comonomer-Sequenzen ab. Das für das Comonomer charakteristische Bandenensemble kann nicht allein zur Quantifizierung verwendet werden, da die Intensität der Spektren vom Fokus der Probe und der spektralen Erfassungszeit beeinflusst wird. Daher ist ein interner Standard zur Normalisierung der Intensität des Bandenensembles erforderlich. Für diesen Zweck wurde die Intensität der C-C Schwingungsbande bei 1295 cm^{-1} als geeignet identifiziert. Dieses Methode wurde auch zur Bestimmung des Comonomergehaltes von einem Copolymer aus Ethylen und einem cyclischen Comonomer (Ethylen / Norbornen) mit geringer

Kristallinität erweitert, wo die Banden durch Streuung aus den Comonomersequenzen dominieren. Aufgrund der geringen Probenvorbereitung, der kurzen Datenerfassungszeit sowie der zerstörungsfreien Natur hält der Raman-spektroskopische Ansatz Potenzial für die Qualitätskontrolle. Ein starker Bedarf für eine solche Technik besteht auch in der Flüssigkeitschromatographie, wo die Probenmengen isolierter Fraktionen generell sehr klein sind.

EVA-Harze werden weit verbreitet zur Verkapselung von Photovoltaikmodulen verwendet. Der Vernetzungsgrad spielt dabei eine kritische Rolle bei der Zelleffizienz. Eine entscheidende Frage bei Prozess↔Eigenschafts-Beziehungen für das Verfahren der Verkapselung ist, wie der Grad der Vernetzung, XC, und insbesondere dessen räumliche Verteilung und Inhomogenitäten identifiziert werden können. Techniken wie DSC, FT-IR-Spektroskopie und Soxhlet-Extraktion wurden bisher für diesen Zweck verwendet. Doch all diesen Ansätzen fehlt eine räumliche Auflösung, so dass sie daher auf die Mittelwertbestimmung von XC begrenzt sind. Lokale Inhomogenitäten können nicht ermittelt werden. In den Untersuchungen konnte gezeigt werden, dass die Empfindlichkeit von FT-IR und DSC-Analysen, die auf der Analyse der Menge der restlichen Vernetzer beruhen, nur eine begrenzte Anwendbarkeit haben. Als Modell wurden zwischen Teflonplatten vernetzte Laminate verwendet. In der vorliegenden Studie wurde ein Verfahren, basierend auf Raman-Mikroskopie entwickelt, um lokale Schwankungen bei der Vernetzung von EVA zu analysieren. Die Intensität der jeweiligen νCH_2 Schwingung bei 2934 cm^{-1} und der νCH_3 Schwingung bei 2885 cm^{-1} spiegeln die Umwandlung der Methylgruppen des VA Comonomers in Methylenbrücken als Folge der Vernetzung wider. Um diese relativen Werte in absolute Werte zu übersetzen, wurde eine Kalibrierung, basierend auf einer hoch und einer nicht vernetzten EVA Probe als Referenz verwendet und mit den Ergebnissen der Soxhlet-Extraktion korreliert. Das entwickelte Verfahren wurde dann angewendet, um Inhomogenitäten des Vernetzungsgrades in zwischen Glasscheiben laminierten EVA-Folien zu untersuchen. In diesem Fall ergab die Quantifizierung der Vernetzung deutlich höhere Werte für XC im Vergleich zu den Modell EVA-Laminaten. Dies kann durch Unterschiede in der Kühlrate des Glaslaminats erläutert werden, was

zur Bildung von mehrfachen Vernetzungen führt, die dann durch Raman-Spektroskopie ebenfalls erfasst werden, und zeigt somit die Grenzen der Übertragung vom Modellsystem in den realen Prozess auf.

PP wird verbreitet zur Herstellung von Rohren für das Bauwesen und Konstruktion verwendet. Die Verarbeitung von PP führt jedoch regelmäßig zu scherbedingten Anisotropien in der Schmelze, die sich im verfestigten Produkt in Form von Variationen hinsichtlich des Grades der Kristallinität (Xc), der Kettenorientierung und der polymorphen Zusammensetzung zeigen. Die räumlichen Variationen in der Polymermorphologie wurden durch das Raman-Spektrum des α- und β-Polymorphen von PP identifiziert und analysiert. Änderungen der polymorphen Zusammensetzung zeigen sich in einer Verschiebung der Banden bei 809 und 841 cm^{-1}. Daher wurde ein neues Verfahren entwickelt, um selektiv die Anwesenheit des α-Polymorphen in PP-Platten festzustellen. Unter Verwendung der Bandenverschiebung bei 2954 cm^{-1} konnten Schwankungen des Kristallinitätsgrades über den Querschnitt eines Sphärolithen beider Polymorphen qualitative ermittelt werden. Dieses Verfahren wurde verwendet, um die Kristallinitätsprofile für beide Polymorphe zu vergleichen. PP Schweißungen zeigen einen großen Einfluss der Verarbeitungsbedingungen auf die Morphologie und stellen somit notorische Schwachstellen dar. Techniken wie DSC (in Kombination mit mechanischer Probenabtragung) und FT-IR-Mikroskopie weisen eine begrenzte Schrittweite auf. Daher können komplexe Änderungen in den Schweißnähten nicht mit der erforderlichen Ortsauflösung erfasst werden. Hier bietet die Raman-Mikroskopie eine Alternative, welche es ermöglichte über den Schweißkanal zwischen zwei stupfgeschweißten PP-Platten einen Gradienten der Kristallinität von etwa 18 % zu beobachten. Die Auswirkung des Schweißens auf die Morphologie wurde ebenfalls untersucht. Die Abkühlzeit in der Schweißkernregion begünstigt die Bildung der β-polymorphen Form. Die morphologischen Veränderungen eines binären Schweißsystems aus einem PP-Homopolymer (PP-H) und einem statistischen Propylen/Ethylen Copolymer (PP-R) wurden über die Schweißnähte untersucht. Für PP-R ergab sich eine höhere Kristallintät des Schweißkerns und es wurde keine Ausbildung der β-polymorphen Form beobachtet. Der Schweißkern der PP-H Probe zeigte jedoch ein ähnliches Profil wie bei der

vorherigen Probe. Die Verwendung von Raman-Mikroskopie ermöglichte es auch die räumliche Verteilung der beiden Polymere zu charakterisieren und eine klare Grenzschicht zu beobachten, was darauf hinweist, dass keine Interkalation der beiden Komponenten beim Schweißen erfolgt.

Die obige Arbeit zeigt neue Perspektiven der Raman-Mikroskopie zur Charakterisierung von Kunststoffen auf. Die experimentellen Protokolle können in der Qualitätskontrolle von Ethylen/1-Olefin-Copolymeren hinsichtlich des Gehaltes an Comonomer eingesetzt werden. Die Homogenität der Vernetzung von EVA-Laminaten, wie sie zur Verkapselung von Photovoltaikmodulen verwendet werden, kann erstmals ortsaufgelöst bestimmt werden. Die Auswirkungen der Verfahrensparameter auf die Morphologie von Schweißnähten in PP wurden detailliert analysiert und Strukturinformationen, die zuvor nicht gewonnen werden konnten, sind nun leicht zugänglich.

2. Introduction and Preface

Plastics offer a unique portfolio of properties: they can be used in a wide range of temperature, are chemically and light resistant, are strong and tough, can be easily extruded into thin films and molded into the shape of a universe of products based on the application. Due to these attractive features, paired with their low costs, the annual worldwide demand for plastics reached 300 MMT in 2013 and is growing continuously. Common examples of plastics include flexible films for packaging, crates for transport, containers for storage, building materials such as door frames and window panes, glass replacement for optical materials, pipe materials and several more. Due to the diversified number of uses, plastics have become an integral part of everyday life.

Amongst the multitude of plastic materials available, polyolefins are, by volume, the most important commodity polymers with an annual production of 170 MMT by the year 2013. Due to their versatile application properties paired with an excellent cost/performance ratio, polyolefins continue to find acceptance in novel applications,

where they successfully compete with traditional materials like metals or ceramics. Even more, their cost/performance ratio enables polyolefins to compete with more costly engineering plastics, thus contradicting forecasts from the late 20th century. An important driver for this success story is the ability to tune the molecular heterogeneities as a result of rapid advances in catalysts and process technologies.

The end properties of semi-finished goods are as a rule affected by the type of conversion process and the parameters used herein to shape the resin to the final product. Processing a polymer into the final product regularly infers anisotropies in the melt due to shear forces, which then result in structural variations in the solidified specimen. The latter embody themselves in the form of spatial variations in morphology, with their length scale and variance depending on the specific process and conditions. These in turn have a significant impact on the macroscopic properties, such as mechanical properties and crack propagation. Hence, investigating the polymer morphology in a comprehensive manner is of pivotal importance in order to establish process→structure→property relationships, which then can be used to optimize manufacturing. Thus, there is a continuous need of developing analytical techniques which give access to the spatial distribution of the microstructure and morphology, to be able to predict their impact on the macroscopic properties governing the end use. Several analytical techniques are used to determine the variations in the morphology of polymers but the information obtained by such techniques is averaged out over the sample analyzed, and obtaining a highly resolved spatial profiling of the morphology through the sample still remains a challenge.

Raman spectroscopy is a highly sensitive technique to structural and morphological variations, which is predestined for analyzing the morphology in plastics. The technique has been used extensively in non-invasive medical diagnostics, in-vivo blood glucose quantification, non-destructive analysis of art objects, and contaminant identification in pharmaceuticals. Yet, applications of Raman spectroscopy as a routine analytical method in characterization of plastics are fairly limited, compared to infrared microscopy. This can be attributed to the problem of fluorescence, burning of the polymer samples due to laser irradiation and inter-mixing of the scattered

radiation from the surroundings, all of which impact the Raman spectrum obtained. Due to these either the sample cannot be analyzed, or a mixed spectrum is obtained in most cases where it is difficult to ascertain the individual components.

With the coupling of light microscopes and the rapid advancements in instrumentation ensuring a high confocality by eliminating the scattered surrounding radiation, the potential of Raman microscopy for analysis in plastics is immense. This has also been augmented by the coupling of power meters to control the laser intensity using which samples sensitive to burning such as thin polymer films can easily be investigated. The coupling of a light microscope allows spatially resolved profiling of morphological or chemical variations. This has been exploited in the determination of blend domain size distributions, the functionalization of micro-polymer particles in colloids, and the identification of unknown materials/contaminations in quality control.

The aim of the work presented in this thesis is to develop Raman microscopy as a routine technique for characterization of plastic materials and obtain valuable information about the morphology which could not be determined using other competitive analytical techniques. Obtaining high resolution information about the subtle variations in the macromolecular arrangement and composition occurring during the process such as cross linking, crystallization and blending is very difficult. This information about structural variations obtained through techniques such as μFT-IR is insufficient to develop structure→property relationships due to its limited theoretical spatial resolution $\sim$10 μm.

Another important aspect is to develop an analytical method which allows for non-destructive measurement of analytes indifferent to the presence of glass/water as surrounding media. This would be valuable for carrying out in-situ measurements on plastics materials embedded in glass such as in photovoltaic encapsulants, where uniformity in properties such as crosslinking is necessary for high efficiency of the module. This method could then be applied for quality control purposes in such modules, where the current techniques involve destruction of the module prior to

assessment of the encapsulant properties rendering these methods unsuitable for any online evaluation. Another challenge is encountered during the synthesis of copolymers such as ethylene/1-olefins and characterization of such materials where sample amount is limited such as in thin films, tapes etc. Here, a strict control of the comonomer content is required for optimal properties in the final product and there is currently no method available which can provide a rapid assessment of the comonomer content requiring small amounts of samples suitable for quality control investigations. Raman spectroscopy as a technique will be probed to utilize its high sensitivity, low measurement times, low requirement of sample and minimal sample preparation to address some of these issues faced regularly in the analytical assessment and creation of defect-free plastic materials.

This thesis can be divided into five parts. The first one comprising of Chapter 3 which provides a general overview of the state of the art in spectroscopic characterization techniques used to investigate the microstructure and morphology of plastic materials. This chapter also details about the advancements in the field of Raman spectroscopy making it as a technique suitable for analytical investigations in polymer analytics. The second part formed by Chapter 4 details the background of the research work forming the introduction. The third part formed by Chapter 5 comprises of the experimental section and gives a details of all the samples analyzed during the investigations. Chapter 6 showcases the research work conducted in the thesis and comprises of the results and discussions. Finally, Chapter 7 summarizes the conclusions from the research conducted as part of the thesis.

3. Characterization of polymers using spectroscopic techniques

Polymers, though constituted from simple repeating units, show a large variation in terms of chemical composition, molecular arrangement, thermal properties and mechanical properties which ultimately defines the end usage. Processing polymers into the final product may infer anisotropies in the melt due to shear forces, which then result in structural variations in the solidified polymer. The latter are seen as spatial variations in morphology, with their length scale and variance depending on

the specific process and conditions. These in turn have a significant impact on the macroscopic properties, such as crack propagation. [1-3] Blending/copolymerization of two or more polymers or incorporation of fillers/ additives in polymers to improve one or more of the properties including the finish, mechanical properties and durability, also leads to the development of heterogeneities with regard to blend domain size and copolymer/additive distribution. These heterogeneities further lead to deterioration in end properties. Further, polymers may crystallize in several polymorphic forms, such the α-, β- and γ- polymorph known for polypropylene, and crystallization into a particular polymorph is governed by the processing parameters, which in turn also effect the final properties. Hence, it is important to understand and assess the variations incorporated in the macromolecular arrangement in a comprehensive manner in order to establish process→structure→property relationships and then use these to optimize manufacturing.

The major spectroscopic techniques used in the industry for polymer characterization are as listed below.

1) NMR spectroscopy
2) FT-IR spectroscopy
3) Raman spectroscopy

3.1 NMR Spectroscopy:

NMR spectroscopy is a powerful technique in chemical analysis with applications ranging from inorganic and organic chemistry, biochemistry to medical sciences. The basic concept underlying NMR involves the interaction of the magnetic properties of nuclei with an external magnetic field. In the absence of an external magnetic field the magnetic spin of the nuclei are aligned in a way that the magnetic dipoles are randomly oriented. However, when an external magnetic field is applied, the dipoles orient in different energy states based on an energy difference, ΔE, governed by Eq. 1

$$\Delta E = \left(\frac{h\gamma}{2\pi}\right)\mathrm{B} \qquad 1$$

Where, γ = *gyromagnetic ratio*

h = *Planck's constant*

B = *the strength of the external magnetic field*

The energy states with and without an external magnetic field for ^{1}H are shown in Figure 1 as an example.

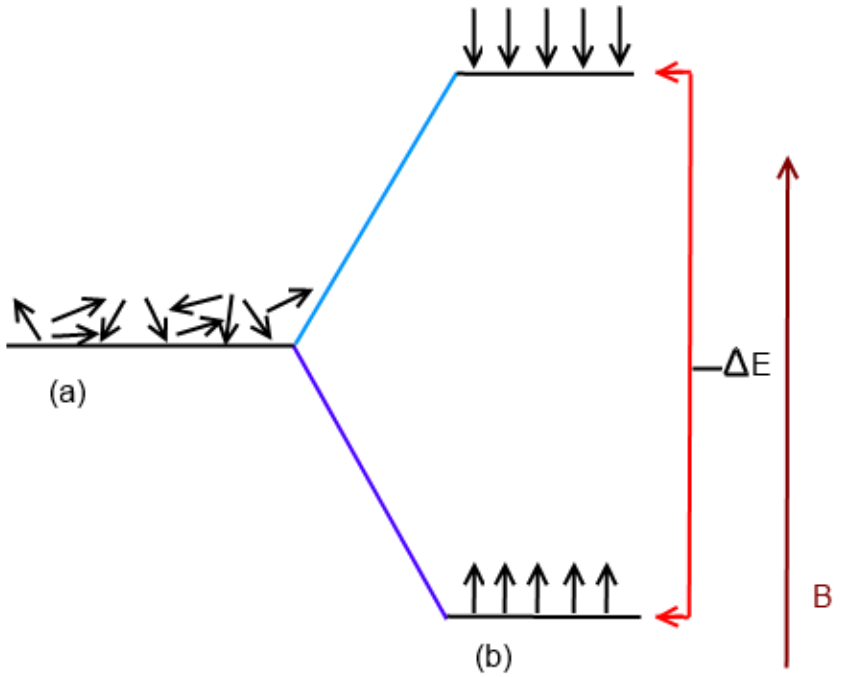

Figure 1: Representation of spins of ^{1}H atoms under a) no magnetic field and b) an external magnetic field B.

In addition to the nucleus, the applied magnetic field also interacts with the electrons spinning around the nucleus. The spinning electrons induce a secondary magnetic field which also influences the total magnetic field experienced by the nuclei. Therefore, the local electronic environment surrounding the nucleus impacts the magnetic field experienced by the nucleus, which is called 'shielding'. This in turn

causes a slight change in the energy levels which requires a different energy for the magnetic dipoles to orient themselves, thus affecting the NMR spectrum. This effect due to shielding allows the structure elucidation of molecules, delivering vital information about the molecular arrangement. Each peak in the NMR spectrum depicts a distinct molecular environment and the area of the peak corresponds to the number of nuclei present in the respective state. Several nuclei having different *gyromagnetic ratio* such as ^{1}H, ^{13}C, ^{15}N, ^{19}F, ^{31}P etc., are applied for NMR measurements based on the requirements. Among these ^{1}H and ^{13}C are the most commonly used for NMR measurements in polymers and are widely used.

3.1.1 NMR of polymers

Over the last few decades, NMR spectroscopy has emerged as an indispensable tool for structure elucidation in polymers. Structural information is deduced from the *chemical shift (ppm)* which reflects the ΔE with reference to the reference proton used for excitation (e.g., ^{1}H in Figure 1). A reference is chosen for which the chemical shift is assigned 0.00 ppm and the different resonances obtained are arranged in accordance with the IUPAC recommended δ chemical shift scale. NMR can provide information about

- Chemical structure in single and multiphase systems: Useful in structure identification for multi component systems and miscibility in polymer blends [4, 5].
- Stereochemistry and isomerism: Information about polymer conformation and configuration including polymer tacticity can be easily deduced [6-8]
- Molecular Structure: Comonomer sequences in copolymers and unsaturation in polymer chains structures can be identified [7, 9-12].
- Cross linking, functional groups and end groups: NMR is useful in determining the end groups, functionalization and the presence of crosslinking in in synthetic polymers. [13-16]
- Intermolecular interactions: Intermolecular interactions in biochemistry including proteins and trace impurities extensively use NMR evaluations [17, 18]

- Reaction monitoring: Monitoring the reaction progress and controlling the polymerization synthesis is also carried out with the help of NMR [19, 20]

3.2 FT-IR spectroscopy

FT-IR is a powerful vibrational spectroscopic technique in polymer analytics. The technique is well suited to elucidate the molecular structure, the chemical composition and the bonding arrangement in a copolymer, composite or a polymer blend. Apart from this, FT-IR is routinely used in bio-analytics where it is widely used for structure elucidation and identification of sample impurities [21]. The IR method provides a rapid assessment of samples and accurate interpretation about the sample composition can be acquired, reflected in the IR-spectra obtained.

FT-IR is based on the absorption of infrared radiation by the molecule. A normal vibrational mode in a molecule gives rise to an absorption of electromagnetic radiation only when the transition is induced by the interaction of the electric vector **E** of the incident beam with the dipole moment of the molecule. This implies that the dipole moment for the molecule should be nonzero for showing IR absorption. The change in the dipole moment of a molecule can occur due to molecular motions, such as vibrations and rotations. The absorption of IR radiation causes transitions between rotational and vibrational energy levels, and the difference in energy between the ground (E_0) and the excited (E_1) level is proportional to the frequency (ν) of the incident radiation (Eq. 2)

$$\Delta E = E_1 - E_0 = h\nu \qquad 2$$

where h is Planck's constant. The frequency of IR absorption is directly proportional to the wavenumber.

$$\tilde{\nu} = \frac{\nu}{c_1} \qquad 3$$

where c_l is the velocity of light. A vibrating molecule absorbs an energy corresponding to ΔE, which is typically depicted in the form of a spectrum with the wavenumber on the x-axis and the intensity of the absorption in the y-axis. The IR absorption spectrum of a compound is a unique property and apart from optical isomers no two compounds can have an identical IR spectrum, making the technique suitable for identification of unknown materials and contaminations. FT-IR is generally carried out in two basic modes i.e. Attenuated Total Reflectance (ATR) and in transmission mode.

3.2.1 FT-IR ATR

ATR is a surface technique, as the spectral information is retrieved from a few microns below the sample surface. Infrared reflection in this case is attenuated by absorption within a surface layer a few micrometer deep inside the sample. In this case however, the technique is useful for analysis of most polymer samples, as it requires minimal sample preparation and it allows for measurements of samples in the form of powders, films, gels and even liquids. Thus, it is well suited for sample identification and for qualitative assessments in analytics. The major drawback for the technique is however, that the obtained spectra are affected by a number of experimental parameters such as the applied pressure, the surface area of contact and the change in the refractive index with the penetration into the sample [22]. This therefore limits the utilization of the ATR method for quantitative analysis.

3.2.2 FT-IR in transmission mode

The absorption characteristics of infrared radiation transmitted through a specimen provides information about the whole sample volume and can be used to quantify the sample constituents. The initial intensity (I_0) of the beam and its intensity after passing the sample (I) are related to the absorbance (A) of the sample according to Eq. 4

$$A = -\ln \frac{I}{I_0} = \varepsilon \cdot c \cdot d \qquad 4$$

ε is the molar absorption coefficient, d the path length, and c is the content of the absorbing moiety.

A is a measure for the loss of energy from the incident radiation by the sample. Samples are often reshaped to a defined geometry in order to keep d constant. Since ε and d are constants, A is directly proportional to c and thus can be used to quantify a specific substance. For this purpose an absorption band specific for the component to be quantified is identified using reference spectra or spectroscopic databases. However, ε has to be determined by calibrating the absorbing moiety in the sample being investigated.

Apart from determining the sample composition in a quantitative manner, IR measurements in transmission mode can be utilized to measure the sample morphology. The latter includes orientation of the macromolecular chains and the degree of crystallinity. A quantitative assessment of the chain orientation and the crystallinity can then be correlated to the macroscopic properties of the samples such as the mechanical properties.

The basic model to calculate the orientation of polymer chains was developed by Fraser and Beer [23-25]. Fraser's model relies on the principle of dichroism (D), where D is defined as the ratio of the absorbance of a vibration when the electric vector of the incident linear polarized light is parallel (A_{II}) to the one with perpendicular direction ($A_{\perp}$) (Eq. 5).

$$D = \frac{A_{II}}{A_{\perp}} \qquad 5$$

Fraser's orientation function (f_F) is expressed as

$$f_F = \frac{D-1}{D+2} * \frac{D_0+2}{D_0-1} \qquad 6$$

where D is the ratio of the absorption coefficients of the absorptions ($A_{\parallel}$) and ($A_{\perp}$). D_0 is related to the angle between the chain axis and the transition moment vector α_T by Eq.7.

$$D_0 = 2 * \cot^2 \alpha_T \qquad 7$$

This approach can only be used if the chain orientation is symmetric with respect to the Z axis. As a result, the parallel and perpendicular directions of the sample have to be defined. However, most of the processing techniques induce an orientation of the polymer chains in semi-finished products, which is not known. To solve this, an extended Fraser's model, that permits the calculation of 'f' with respect to the three coordinates, was introduced [26]. In this, the absorbance of linear polarized light along the three perpendicular axes of the sample is measured. Thus, f_F along the Z axis can be calculated according to Eq. 8.

$$f_F = \frac{3 * \frac{A_z}{A_x + A_y + A_z} - 1}{2} * \frac{D_0 + 2}{D_0 - 1} \qquad 8$$

with A_x, A_y and A_z being the absorbances along the X, Y and Z axis, respectively.
To obtain the average chain orientation in all three dimensions, the functions f_x and f_y have to be calculated by exchanging the numerator term "A_z" in eq. 8 to A_x and A_y respectively. The angle between the preferred direction (Z axis) and the chain axis (θ) for the Z axis is calculated by equating the extended f_F with f as follows;

$$\frac{3 * \frac{A_z}{A_x + A_y + A_z} - 1}{2} * \frac{D_0 + 2}{D_0 - 1} = f_z = \frac{3 * \langle \cos^2 \theta_z \rangle - 1}{2} \qquad 9$$

Similarly the crystallinity across polymer samples can also be quantitatively analyzed using IR-spectroscopy by utilizing bands specific for showing the crystallinity across

the samples. The technique has been widely used to determine the X_c of PP [27]. The bands at 841 cm^{-1} (absorption from the crystalline phase) and 974 cm^{-1} (absorption from both the crystalline and amorphous phase) have been used for this purpose. The absorbance of these bands from three mutually perpendicular directions (MD, ND and TD) is averaged since these bands are sensitive to dichroism. Consequently, A_0^{841} and A_0^{973} along the three mutually perpendicular axes are then used to calculate the X_C according to Eq. 10.

$$X_c^{IR} = \frac{\alpha_{974}}{\alpha_{841}} \cdot \frac{A_0^{841}}{A_0^{974}} \cdot 100 \qquad 10$$

where α_{974} and α_{841} are the absorption coefficients of the respective bands, and the ratio between these has been reported to be 0.79 [28] for the case of PP.

3.3 Raman spectroscopy

Raman spectroscopy is another vibrational spectroscopic technique based on the inelastic scattering of light by matter which was first discovered by C.V. Raman in 1928 [29]. In 1930, he was awarded the Nobel Prize for his work on the inelastic scattering of light and for the effect which was named after him.

Raman scattering is a process of re-radiation of scattered light by dipoles induced (**P**) in the molecules by the incident light and modulated by the vibrations of the molecules. In Raman scattering by molecules in isotropic media, the dipoles are simply those which result from the interaction of the electric field component of the incident light with the sample molecules

$$P = \alpha^* E \qquad 11$$

Where α^* is the molecular (dipole) polarizability.

The mechanism for the Raman effect lies in the irradiation of the sample with monochromatic light, causing a change in the vibrational quantum states of the molecules being illuminated. As a result a small fraction of the scattered radiation is shifted to frequencies which correspond to the sample's vibrational transitions. With sample illumination being monochromatic, most scattering taking place is elastic with no loss of energy and, therefore, no frequency change. This type of elastic scattering, which appears as an intense, unshifted component of the scattered light is called Rayleigh scattering. Raman scattering, however, is due to the inelastic scattering of incident photons, wherein the energy is transferred to or received from the sample due to changes in the vibrational or rotational modes of the sample molecules, causing a change in the energy, and therefore the frequency of the scattered light. Lines shifted to energies lower than the source are generated by molecules in the ground-state, while the slightly weaker lines at higher frequency are due to molecules in excited vibrational states. These lines, the result of inelastic scattering of light are referred to as Stokes and anti-Stokes lines, respectively (Figure 2).

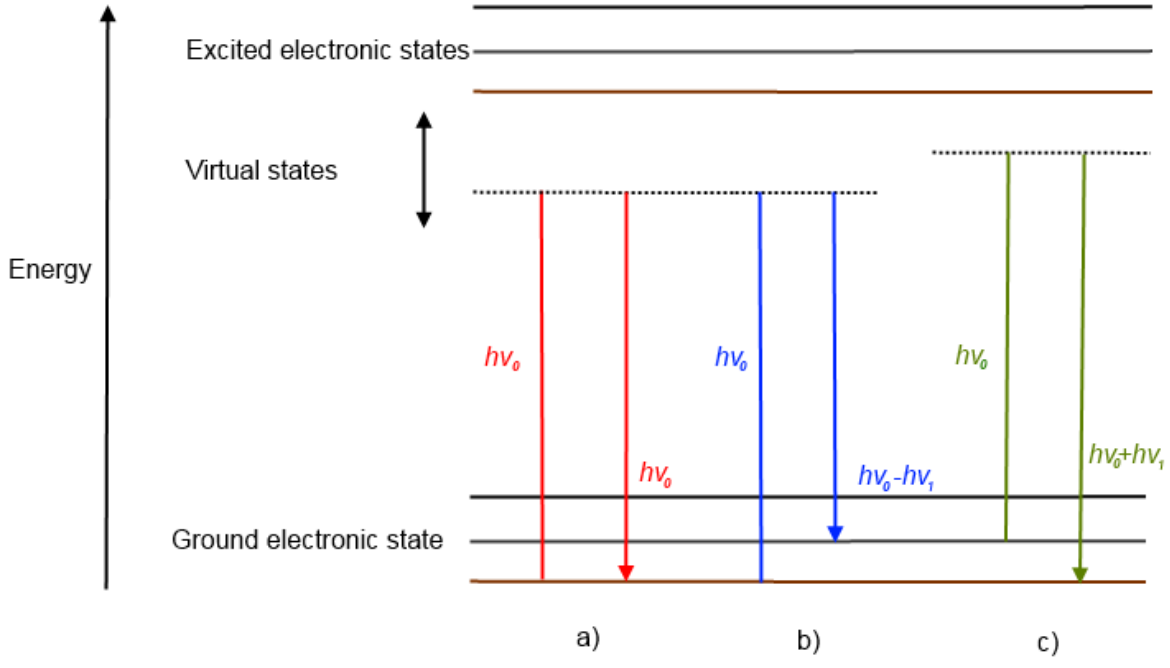

Figure 2: Inelastic light scattering

In this inelastic scattering, the molecule is excited to a virtual state, which corresponds to a quantum level relating to the electron cloud distortion created by the electric field of the incident light. A virtual state does not correspond to a real vibrational or electronic energy level of the molecule, but rather is a sum over all eigenstates of the molecule (Figure 2). The molecule scatters light at the incident frequency; however, it vibrates with its own unique frequencies. If these molecular motions produce changes in the polarizability, the molecule further interacts by superimposing its vibrational frequencies on the scattered light either at higher or lower frequencies, thereby leading to a unique vibrational signature.

3.3.1 Raman spectroscopy in polymer analytics

Raman spectroscopy has been used as an analytical tool for the last few decades. The technique finds widespread usage in bio-analytics as most biological samples require measurements carried out in solution, which is generally water. Raman scattering being unaffected by the presence of water allows measuring of biological samples without any scattering from the solution affecting the spectrum obtained[30]. Another major factor in favor of Raman spectroscopy for measurements is the ease of sample preparation. As there are not specific requirements with regard to shape or surface of the specimen, powders, pellets, molded polymers, fibers and films can be analyzed with ease [31]. The Raman spectra being highly sensitive to the chemical composition, structure and morphology provide a wide variety of information for analytical investigations. Apart from this, the amount of time required for spectral acquisition can be down to a few minutes. All these make it very suitable for online quality control purposes [32].

Raman spectroscopy in spite of being a very sensitive technique has still not been able to develop itself as a routine technique for polymer characterization. The major disadvantages arise when visible laser radiation is used to excite the Raman scatter. The absorption of visible light may result in fluorescence which completely engulfs the Raman signal and renders measurements impossible. Presence of colored pigments,

oils, lubricants, degraded polymers or samples with a large amount of impurities cause a large absorption of visible light and are a major cause of causing fluorescence which renders Raman measurements difficult. The fluorescence needs to be suppressed before the Raman spectra can be obtained for productive measurements. This can be achieved by using a higher excitation wavelength since then the fluorescence is shifted to longer wavelengths relative to the Raman scatter. However, a major drawback is the fact that the Raman scattering decreases as $(1/\lambda)^4$, which in turn results in a lower signal intensity. Another major problem encountered with Raman measurements is the burning of samples upon laser excitation. The risk is especially higher for solid samples with a low melting point and thin films which might burn or can also degrade due to the initiation of thermal degradation by the laser radiation. While investigating the Raman spectra of thin films and polymer blends another problem encountered is the amalgamated effect of all the components present in the sample to contribute to the spectrum obtained. This limits the chemical information generated about the sample composition as, a combined spectra of all the components is obtained. The above problems hindered the use of Raman as a routine technique for polymer analytics.

3.3.2 Confocal Raman microscopy

Combing confocal microscopy with Raman spectroscopy has emerged as an excellent solution to monitor minor structural variations and allows for characterization of highly resolved polymer structures and films. Confocal measurements also greatly reduce the scattered (stray) radiation, which improves the image quality and reduces any out of focus information mixing with the spectra. This also allows for controlling the depth field and measurements can be carried out non-destructively through the samples making it suitable to measure multilayered samples. The setup of a confocal microscope is shown in Figure 3.

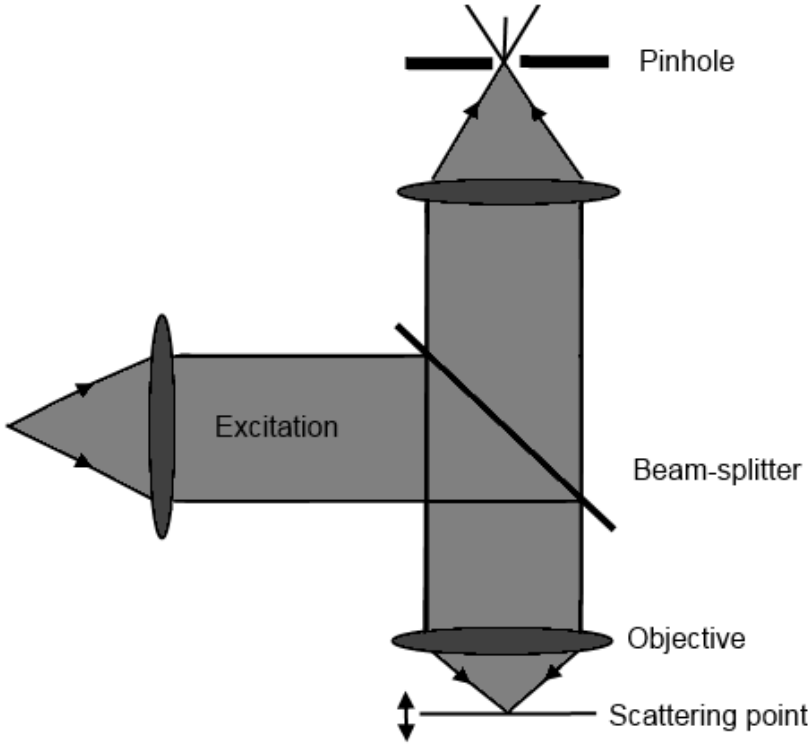

Figure 3: Arrangement of the pinhole controlling signal output

As seen from the figure, the pinhole controls the inflow of signal to the detector and blocks the scattered radiation from the surrounding, thus enabling depth profiling and 3D imaging of samples. Using a confocal microscope for Raman measurements also helps in reducing the fluorescence and hence is an instrumental augmentation in the utility of Raman microscopy compared to the traditional spectroscopic method without using a microscope for characterization.

3.3.3 TrueSurface® chromatic sensor for Raman measurements

The TrueSurface® technique for Raman microscopy measurements is offered by WITec, which allows measurements to be carried out using a topographic sensor coupled with the confocal Raman microscope. The sensor works in non-contact mode and uses the principle of chromatic aberration to map the surface topography. This enables to generate an optical profile of the sample to be measured preceding the

Raman measurements, thereby allowing the sample to remain focused throughout the measurements, which is mandatory in case of uneven surfaces. The working principle of the sensor is shown in Figure 4.

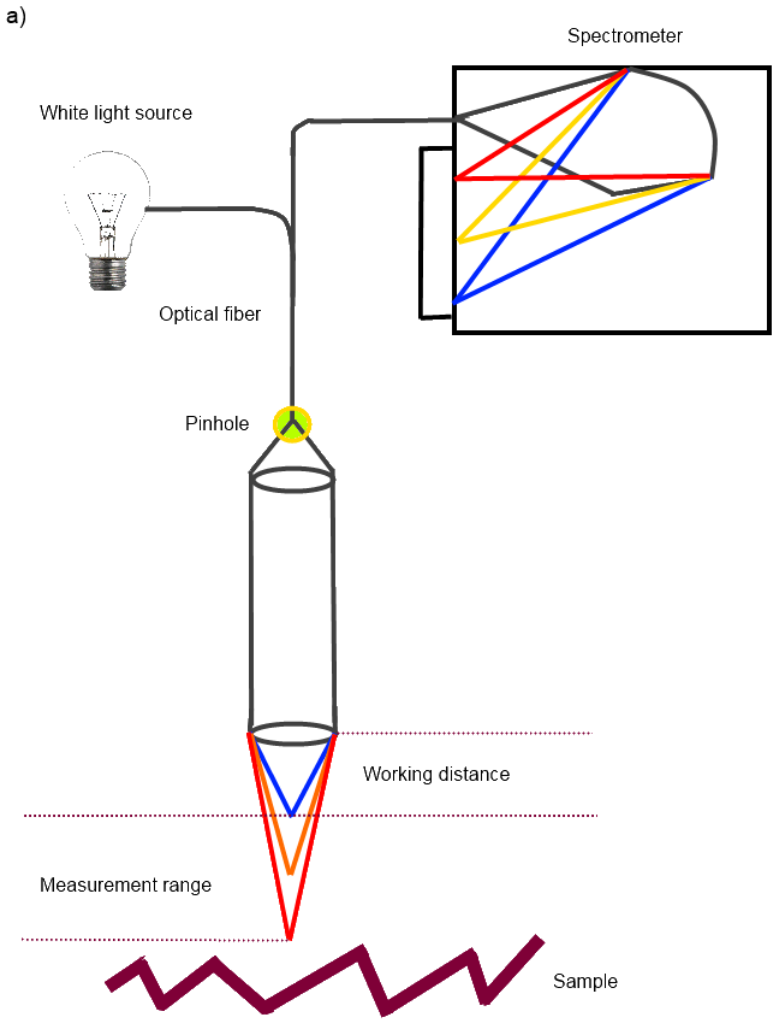

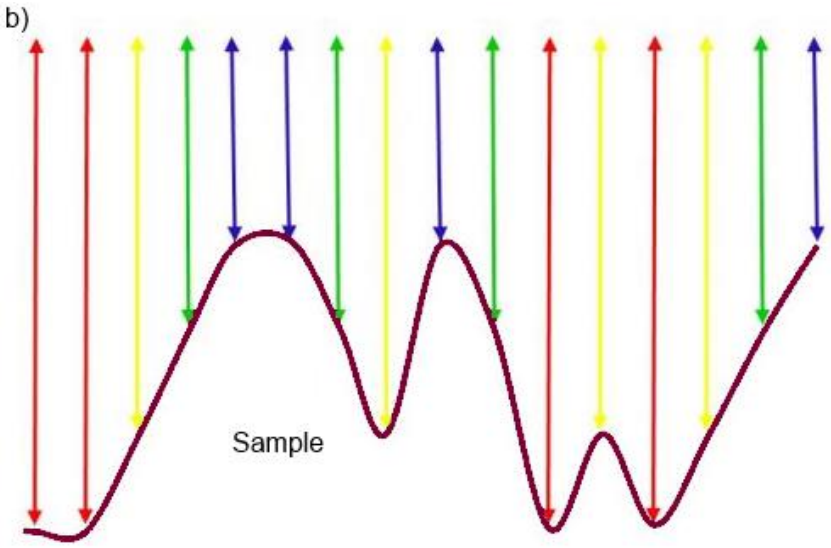

Figure 4: The TrueSurface® chromatic sensor a) working principle b) surface topography mapping with the help of difference in focal distance of each color

For surface profiling a white light point source is focused onto the sample via a hyperchromatic lens assembly which comprises of a lens system with a good mapping capability, but a strong linear chromatic error. Each color therefore has its own focal distance as shown in Figure 4b. The light reflected from the sample is collected with the lens and then focused through a pinhole into a spectrometer. As only one color is in focus at the sample surface, only this light can pass through the pinhole. The detected wavelength is hence correlated to the surface topography. This topographic image is then used while mapping the sample and the changes in sample height are accounted for by continuously keeping the laser in focus using this topographic map. This ensures that valuable information about the sample morphology is obtained even when the sample is rough or inclined. This also ensures that the signal is measured in the focal plane of the sample and scattering from the surroundings does not intermix with the spectra causing intensity fluctuation. The TrueSurface® sensor is attached to the microscope as shown in Figure 5.

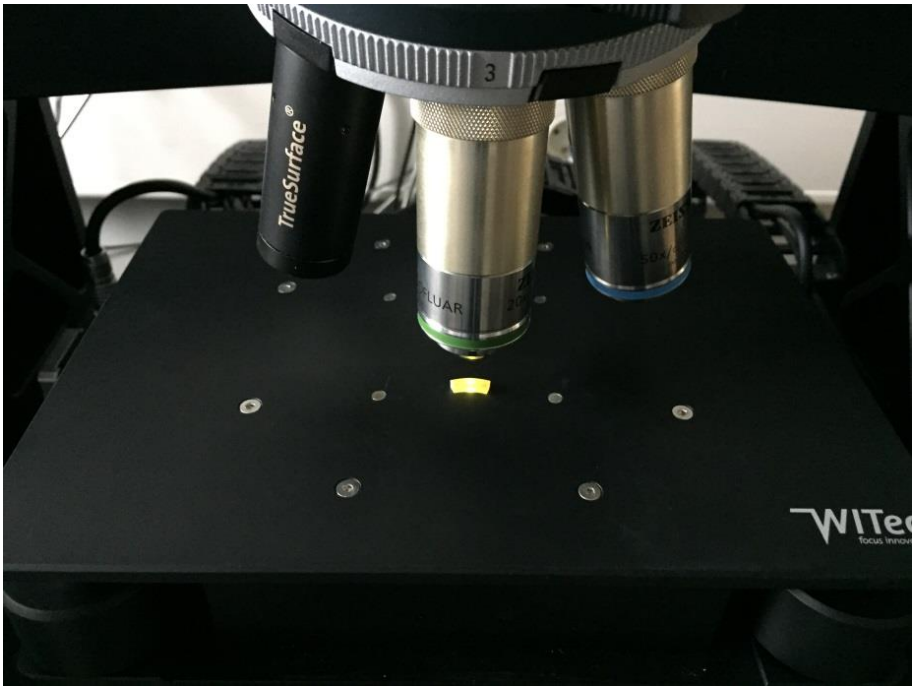

Figure 5: TrueSurface® sensor attached to the microscope assembly

Thus, using this technique the surface topography can be determined and Raman measurements can be carried out by incorporating the topographic adjustments.

3.3.4 Raman microscopic analysis of polymers (fluorescence and sample burning)

As discussed previously, two major problems which restricted the development of Raman spectroscopy as a routine analytical technique for polymer characterization were the presence of fluorescence and sample burning upon laser radiation. Fluorescence can in many cases be avoided by using a higher wavelength excitation. The choice of the laser excitation also depends on the sample being analyzed and the amount of fluorescence present in the sample.

An instrumental improvement for avoiding sample burning under exposure to the laser is by using a laser intensity coupler which is combined with the microscope (Figure 6).

Figure 6: Power meter showing the laser intensity which can be controlled and optimized before starting the spectral acquisition.

This helps in controlling the laser intensity down to a few μW, thereby preventing burning of the samples. Thin polymer films and microtome sections of polymers, which are often embedded in transparent resin systems to ensure easier handling also face the same problem. Another challenge faced during Raman measurements is while measuring samples in solutions, wherein, the analytes often move upon irradiation with the laser due to Brownian motion. Hence, an optimum intensity of the laser is needed for measurement to ensure the samples remain in focus, do not move due to high laser intensity and also do not burn during the measurement. Another critical parameter for measurement of samples sensitive to the laser intensity is the spectral acquisition time. Lowering the laser intensity also leads to a compromise in the spectral intensity, which can however be taken care of by using a higher spectral acquisition time and is especially valuable for measuring graphite filled materials where the sample have a tendency to burn easily upon exposure to the laser and need longer spectral acquisition time for obtaining the spectra (20 sec). Hence, with the control in the surface topography, the laser excitation wavelength, the spectral acquisition time and the laser intensity, a lot of avenues for characterization of polymers using Raman microscopy are open.

4. Theoretical Consideration

The following chapter comprises of the investigations and the method development carried out to utilize the potential of Raman microscopy for characterization of plastic materials and obtain valuable information about the microstructure and morphology which could not be determined using other competitive analytical techniques. The chapter can be subdivided into three sub-chapters. The first sub-chapter deals with underlining the need for developing a method for structure elucidation and quantification of the comonomer content in ethylene-1-olefin copolymers. The chapter goes ahead with giving a short background about ethylene-1-olefin copolymers and explaining the current state of the art techniques used for determining the comonomer content. Then, the need for using Raman spectroscopy for such quantification is detailed, and such a method would be valuable as a fast and non-destructive tool for quantification measurements in quality control during synthesis of these materials. The second sub-chapter studies the application potential of the Raman analysis approach to minute variations with regard to crosslinking of EVA which is used as an encapsulant for manufacturing PV modules. A short insight into the manufacturing process and the need for encapsulation of PV modules has been given. This proceeds with analyzing the current state of the art techniques used for investigating the percentage crosslinking in EVA.

The third sub-chapter deals with the need to develop a method to investigate the minor variations in the morphology of processed PP materials focusing on polymer welds. The structural arrangements of PP, its importance as a polymeric material and the polymorphs of PP have been discussed. This is followed by a detailed discussion about PP welds, the welding process and its impact on the morphology of the final product. The section also details about the current state of the art techniques used to investigate these changes in the weld morphology and lays the foundation of the need to develop a method using Raman Microscopy which would be able to ascertain the morphological variations in welds due to the processing and thermo mechanical treatment.

4.1 Determining the comonomer content in ethylene-1-olefin copolymers using Raman spectroscopy

Polyethylene (PE) is one of the most important industrial polymers finding a wide range of applications in durable and consumable goods, with a global consumption soaring to 76 million tons in 2010. An excellent cost/performance ratio, recyclability, ease of synthesis and processability have made the market for these polymers to grow continuously[343434]. PE can be classified into the homopolymer and semicrystalline copolymers of ethylene with 1-olefins typically containing up to 20 mol % of comonomer (Linear Low Density Polyethylene, LLDPE). Typically, 1-butene, 1-hexene and 1-octene are used as the comonomer with ethylene. Until the late 1980's PE was synthesized by free radical polymerization or by heterogeneous transition metal catalysts. The early 1990's saw the addition of metallocene catalysts to the portfolio of catalyst systems [33-37] which allow the production of copolymers which are narrowly distributed with regard to molar mass and comonomer incorporation [38]. Such and further advances in the catalyst and process technology thus helped in gaining a better control over the structure dependent performance attributes of ethylene 1-olefin copolymers, acquiring a better control over the structure dependent performance attributes of PE copolymerized with α-olefins as shown in Table 1 (11) [38].

Table 1: Performance attributes governed by the molecular structure of PEs

Performance attributes	Effecting parameters
Stiffness/modulus	Polymer density, % comonomer, crystal morphology
Toughness/ environmental stress/ crack resistance	Tie molecules, M_w, type of α-olefins
Processability, extrudability and melt strength	Long chain branching , molecular weight distribution
Optical properties	Crystallinity, density, comonomer

The comonomer content is a fundamental molecular parameter, which strongly influences the macroscopic polymer properties. As a consequence, there continues to be a need for analytical techniques, which are fast and require minimum effort with regard to sample preparation for quantification. The current techniques used for determining the comonomer content in ethylene-1-olefin copolymers are as follows.

Nuclear Magnetic Resonance (NMR)

NMR has been widely used for structure elucidation of ethylene/1-olefin-copolymers[39]. NMR is specific in terms of acquiring information about the microstructure such as tacticity [40], inverse insertion [12] and comonomer sequence distribution [6]. Being an absolute technique, NMR does not require a calibration, however quantitative measurements require significant amounts of sample, with the mass range depending on instrumentation and experimental parameters. Additionally, sample preparation may pose a bottleneck in high throughput environments.

Fourier Transform Infrared Spectroscopy (FT-IR)

FT-IR has also been shown capable of such quantification but has several limitations [41, 42]. The measurement can be carried out in Attenuated Total Reflectance (ATR) and transmission mode. The first one is a surface technique, as the spectral information is retrieved from a few microns below the sample surface. The obtained spectra are affected by a number of experimental parameters such as the applied pressure, the surface area of contact and the change in the refractive index with the penetration into the sample [22]. However, quantitative information can only be retrieved from measurements in transmission mode which requires significant quantities of sample, typically a few grams, and intensive sample preparation.

Determining the comonomer content using Raman spectroscopy

Raman spectroscopy is sensitive to sample composition and morphological parameters like orientation and degree of crystallinity. The interaction of PE with highly conductive fillers such as carbon nanotubes has been studied by analyzing the band shifts in the Raman spectra of the nanotubes upon intercalation of PE in the nanotube bundles [43, 44]. PE/ polypropylene (PP) blends have also been investigated and being thermodynamically immiscible [45], the domain size distribution and crystallinity for the individual blend components has also been determined [46].

The Raman spectrum of PE is well understood and the fundamental modes of vibration have been assigned [47-49]. The internal mode region of the spectrum has been grouped into three frequency regions, namely the C-C stretching region between 1000 cm^{-1} and 1200 cm^{-1}, the CH_2 twisting modes near 1300 cm^{-1} and the CH_2 bending modes between 1400 cm^{-1} - 1500 cm^{-1} [50]. Subtle changes in the Raman spectra of ethylene 1-olefins have been observed, but have not been developed into a tool to quantify the comonomer content.

For copolymers of propylene with 1-olefins, changes in the intensity of the bands at 809 cm^{-1} and 841 cm^{-1} were observed with increasing content of the incorporated comonomer [51]. The first of these bands corresponds to vibrations of the helically oriented PP chains in the crystalline phase, while the second one is associated with vibrations of the helically aligned PP chains with significant amounts of conformational defects, localized in the amorphous phase.

When 0-20 mol % of 1-olefinic comonomers are copolymerized with ethylene, the changes reflected in the Raman spectra are minute, and these finite details have not gained much attention to be useful for any quantification. For the case of ethylene/1-hexene copolymers changes in the Raman spectra were identified, but have not been developed as a tool for quantification of the comonomer content [52].

So far, analysis of PE by Raman spectroscopy has been limited to deriving the density, degree of crystallinity, and melting point from multivariate analysis of the Raman

spectra [53, 54]. Mauler et al. investigated the influence of comonomer content on the degree of crystallinity and dynamic mechanical properties of ethylene/1-octene copolymers [55]. The Raman spectra were analyzed and a decrease in the degree of crystallinity was observed. Henceforth, developing a fast, accurate and robust method to quantify the comonomer content in ethylene copolymers by Raman spectroscopy would extend this technique further than crystallinity and density measurements, making it suitable for a rapid identification of minute sample amounts. The need for such a tool exists for quality control in polymer synthesis. A further area where a compositional analysis of small amounts of sample is required can be found in liquid chromatography, where, after removing the chromatographic solvent, trace amounts of the remaining polymer have to be analyzed. The non-destructive nature of Raman spectroscopy renders it also a good potential in forensic analysis and the analysis of very small inhomogenities in processed samples e.g., multi-layer films. In this study, we exploit the subtle changes in the Raman spectra of PE upon comonomer incorporation and understand these changes to present a new method establishing Raman spectroscopy as a tool for comonomer quantification for several industrially important ethylene/1-olefins.

4.2 Determining the percentage crosslinking in EVA photovoltaic modules using Raman microscopy

Photovoltaic (PV) modules typically consist of two symmetric layers of solar cells which are encapsulated between two protective films. The latter are in turn mechanically stabilized on the rear side by a 'backsheet' and on the front side by glass or a suitable polymer film. The encapsulant material primarily protects the solar cells against weathering conditions and also provides mechanical stability. It also allows for sufficient isolation of the electrical components to maximize the optical coupling between the solar cells and the incident solar irradiation [56]. Therefore, the mechanical behavior of the encapsulant is one of the major properties defining the type of encapsulant used [57-59]. The setup of a PV module is shown in Figure 7.

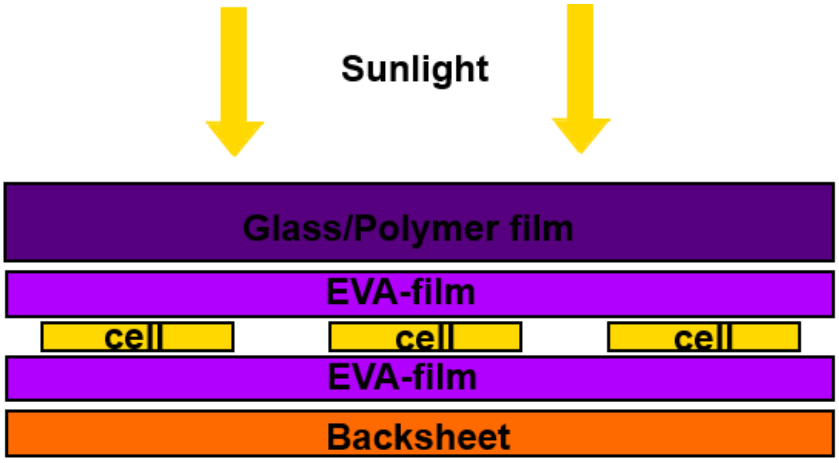

Figure 7: Setup of a PV module

As seen from the figure, the encapsulant material surrounds the PV cells and provides a rigid support structure. Essential criteria for the encapsulant are high rates of light transmission, low sensitivity to degradation by light, good adhesion to the backsheet, solar cell and front glass. [58]. To compensate the buildup of mechanical forces as a result of temperature fluctuation or mechanical load (e.g. wind), the encapsulant must have elastomeric properties. Materials used as encapsulant are silicones, polyvinyl butyral and transparent thermoplastics such as EVA and ionomers [60-63]. EVA, the most commonly used material, is a co-polymer of vinyl acetate and ethylene. Ionomers are copolymers of ethylene and methacrylic acid with a salt added to neutralize them. Ionomers can be used alone or in combination with ethylene 1-olefins comonomers. Encapsulant materials comprising both ionomers and ethylene 1-olefins have been previously reported [64, 65].

The technique of producing these encapsulant foils surrounding the cells is well known. In this procedure the additives and crosslinking agents are homogeneously mixed with the olefin-copolymer e.g., in an extruder, to yield a polymer film. For the encapsulation of the solar cells, the PV module production is typically carried out in a vacuumed lamination oven [66]. Therefore, the stacked setting of the PV-module is prepared first and then heated in the lamination oven. Thus, while the olefin-copolymer (e.g., EVA) is softening, the evacuation of the oven removes the air between the two encapsulant films, which is the most critical fabrication step, taking 4

to 6 minutes. An essential property of EVA is that it flows easily below its curing temperature attaining the shape of the surrounding module. [62, 67] In the next step pressure is exerted for several minutes via a membrane within the laminator, which leads to heat-sealing of the different layers within the PV-module and crosslinking of the encapsulant material. Typical lamination conditions favorable for production of PV-modules are temperatures between 140 °C and 155 °C with a holdup time between 12 min and 20 min. Maintaining uniform profiles with regard to temperature and pressure is important to ensure the production of high performance and air-bubble free modules [68].

Typically, a minute quantity of the cross linker (~ 0.7 wt. %) is used for crosslinking these laminates and being minute in quantity a thorough homogenization of the cross linker is required to ensure optimum properties of the laminates upon crosslinking [69]. Even minor fluctuations in the dispersion or in the processing conditions might have a large impact on the crosslinking developing in the form of crosslinking inhomogeneities. These variations can manifest itself in the form of minor (local) and larger fluctuations depending on the dispersion of the cross linker and the presence of a temperature gradient across the module, which ultimately can affect the efficiency of the PV modules. Homogeneity in terms of crosslinking is important to ensure a long service lifetime and continuous power output. Hence it is important to have a robust method to determine the crosslinking homogeneity in EVA modules, which can be used in an online mode for screening the crosslinking in modules.

The current methods used to study the crosslinking in EVA modules generally involve destruction of the module and extraction of the polymer encapsulant which is a cumbersome process. Also, due to the firm cohesion of the glass covering and the encapsulant, it is extremely difficult to separate the two components and the measurements can be affected by the presence of glass residues. The reference methods used for monitoring crosslinking can be segregated into three categories based on the working principle as:

4.2.1 Chemical Methods for determining Xc

Soxhlet Extraction

Soxhlet extraction is by far the most widely used method for assessing the percentage crosslinking in PV modules. The basic principle of the Soxhlet method is that the sample (M_1) is dissolved in a suitable solvent in a Soxhlet hull. The common solvent used for this purpose is toluene, which dissolves the non-cross-linked material and flushes it out. The cross-linked polymer is then left in a swollen state in the hull and the residual solvent is removed in vacuum at 100 °C. This left over material is then weighed (M_2) and the percentage crosslinking is determined as the ratio of the insoluble residue left in the hull to the initial mass of the sample.

Solvent swelling method

Another method of determining the X_c is by evaluating the swelling properties of the polymer. This solvent uptake by the polymer matrix is determined by the percentage crosslinking, which is expected to decrease with the increasing amount of crosslinking. Hence, for measuring crosslinking, the sample is dissolved in a suitable solvent (toluene) and then decanted. The weight of the swollen polymer is determined and the weight gain due to swelling of the polymer is calculated which gives an indication of the amount of crosslinking in the material.

4.2.2 Thermal Methods for determining Xc

Differential scanning calorimetry

The basic principle of the DSC is to determine the heat flow between a sample and a reference as a function of temperature. It thus allows probing the thermal transitions in the polymer including the glass transition temperature, melting, crystallization and endothermic / exothermic reactions involving degradations / oxidations and crosslinking reactions. Exemplarily, the first heating cycle of EVA is shown in Figure 8.

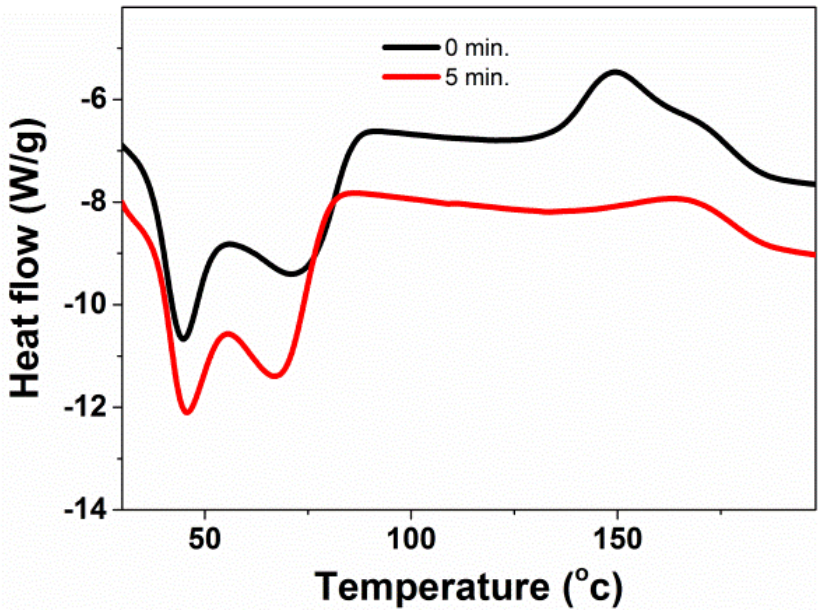

Figure 8: Thermogram of the first heating cycle of EVA

An endothermic double peak showing the melting of the EVA resin can be recognized between 40 - 100 °C and an exothermic event resulting from the consumption of the crosslinker can be seen between 120 - 190 °C in the thermogram. The latter is used to calculate the percentage of crosslinking according to equation 12 by taking the enthalpy of the non-crosslinked sample (ΔHo) as a reference according to[70-74], where ΔHs represents the enthalpy of the cross-linked sample.

$$XC_{DSC} = \frac{\Delta Ho - \Delta Hs}{\Delta Ho} \qquad 12$$

4.2.3 Spectroscopic methods for determining Xc

FT-IR spectroscopy

Infrared (IR) spectroscopy has also been used previously to determine the percentage crosslinking in EVA laminates [75]. Measurements are generally carried out in Attenuated Total Reflectance (ATR) mode as the EVA laminates used in PV modules are too thick (~1 mm) to be measured in transmission mode, showing a total absorption of the IR beam. The FT-IR spectrum of EVA is shown in Figure 9.

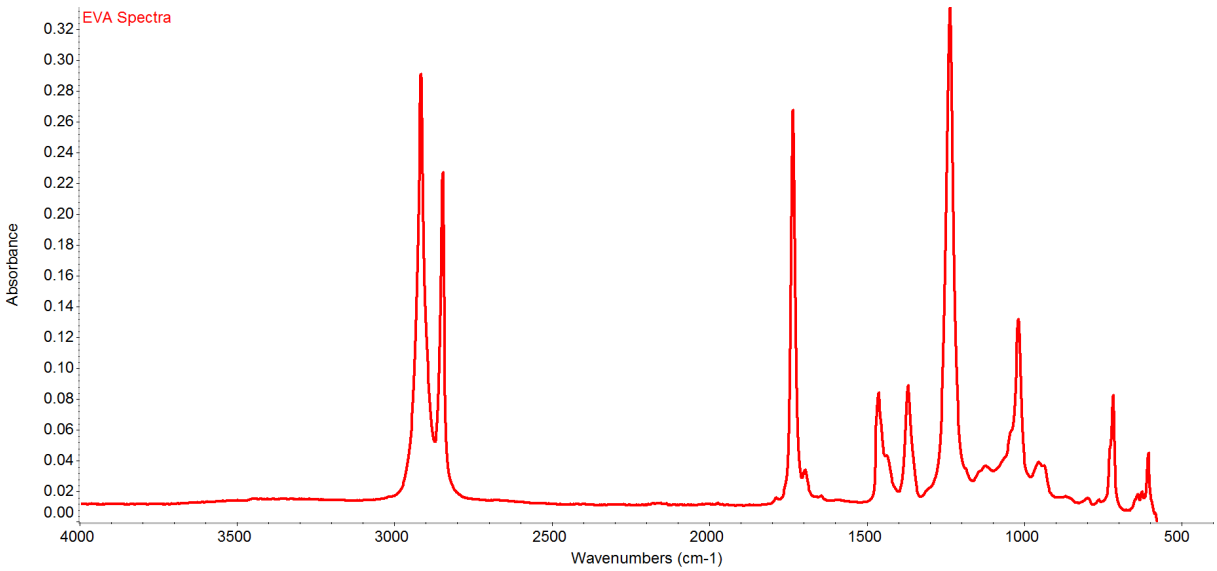

Figure 9: FT-IR spectrum of EVA in ATR mode

The changes due to crosslinking are minor compared to the characteristic bands for EVA. The process of crosslinking could be monitored by analyzing the band characteristic for the residual cross linker and its consumption with lamination time. However, the ATR spectra have been shown to be affected by experimental parameters such as the applied pressure, the surface area being measured and the change in the refractive index with the penetration depth [76] which limits its use for such quantification.

All the above methods for quantifying the percentage crosslinking involve the removal of the encapsulant, which strongly limits their applicability for use as a technique for online assessment of crosslinking in modules and production control. These are also bulk techniques and do not deliver any information about the spatial inhomogeneity in crosslinking.

The aim of this work is to study the crosslinking of EVA encapsulant films and develop a methodology for determining the crosslinking homogeneity in EVA modules, which can be used in an online mode for screening (also spatially determining) the crosslinking in modules non-destructively using Raman Microscopy. Thus, the essential criteria are accuracy as well as speed and ease of measurement.

4.3 Investigating the morphological variations due to processing and thermo-mechanical treatment of polypropylene using Raman microscopy

Polypropylene (PP) is commercially one of the most important synthetic polymers with an exceedingly good cost/performance ratio and ease of processability. PP finds use for a wide range of applications ranging from packaging, household applications and commercial applications such as in apparels, upholstery, floor coverings, geotextiles, car industry, automotive textiles, various home textiles, wall-coverings, pipes for infrastructure [77, 78]. PP also has exceptional mechanical properties such as high stiffness, elongation, tensile strength and resistance to crack propagation[79].

Based on the chemical composition, PP is classified as the homopolymer (PP-H) and a copolymer (PP-R) which is a copolymer of propylene and a low amount of 1-olefins, copolymerized using transition metal catalyst systems [80]. The most commonly used comonomer to form PP-R is ethylene, and the less commonly used 1-olefins include 1-butene or 1-hexene (~ 1.5 – 6 mol. %) as comonomer [27]. These comonomers are incorporated randomly among the propylene units which reduces the crystallinity (X_c) and thereby increases the impact strength [81].

PP is also classified into three categories based on the orientation of the pendant methyl group in the macromolecular chain as isotactic (iPP), syndiotactic (sPP), and atactic (aPP) as shown in

Figure 10.

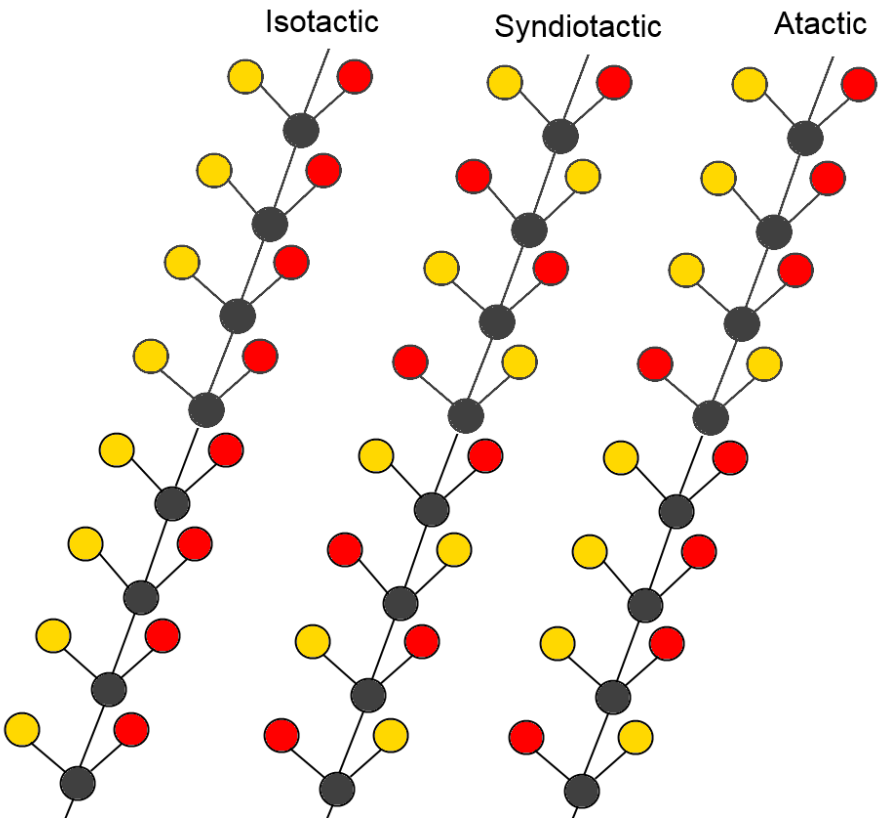

Figure 10: Classification of PP based on the tacticity

In iPP (

Figure 10) the pendant methyl groups point to the same side of the macromolecular chain, while in sPP, the pendant methyl groups arrange themselves in an alternating, repetitive pattern as shown. In aPP, the pendant methyl groups show a random orientation with respect to the macromolecular chain. Due to the random stereochemistry of molecules forming aPP it is difficult for the chains to pack themselves into a regular structure and hence it shows a lower crystallinity compared to iPP and sPP wherein the chains form a regular arrangement leading to higher crystallinity.

4.3.1 Morphology of PP

During the process of crystallization, macromolecular chains in PP pack themselves and arrange into a threefold helix which may be right (R) or left (L) handed, with the methyl groups pointing upwards or downwards as shown in Figure 11.

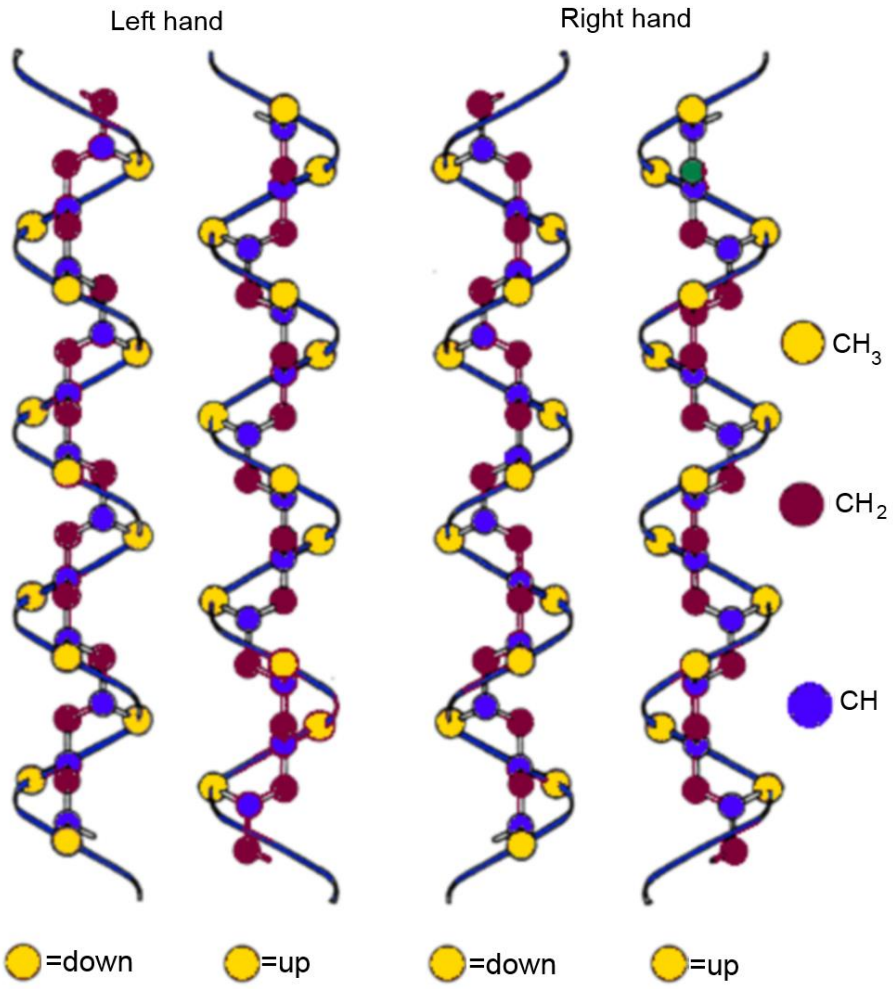

Figure 11: Helical structure of PP

The macromolecular chains arranged forming the helical strands arrange themselves back and forth to form the lamellae, which grow radially and tangentially. These helical strands emanate from a central nucleating center and form spherulites. The

non-crystallized polymer chains, also called as the tie molecules, interconnect the lamellar structures formed.

Based on the crystallographic structure it has been known that PP crystallizes in three different polymorphs namely the α-, β- and γ-form [82, 83]. Wide angle X-ray (WAXS) scattering has been used to identify these, and crystallization into a specific form depends on the processing conditions[84-88]. Nucleating agents may promote the formation of a particular polymorph as the mechanical properties of PP depend on the polymorphic composition [84, 85], and an enriched percentage of β-phase leads to higher tensile elongation and improved impact resistance [89].

4.3.1.1 Alpha (α-) form of PP

In the α- form of PP the macromolecular chains arrange themselves in the form of a monoclinic unit cell [87]. Lamellar growth in this polymorph takes place into the radial direction and the radial lamella undergo branching as cross hatching, which is a characteristic of the α-form. The branches formed on the lamellae are regarded as quadrites [88]. The crystallite axis/chain axis (c-axis) of the polymer chain is perpendicular to the plane of the radially growing lamellae. The polarized light microscope image of an α- spherulite and the spherulitic structure of the non-nucleated α-PP are shown in Figure 12.

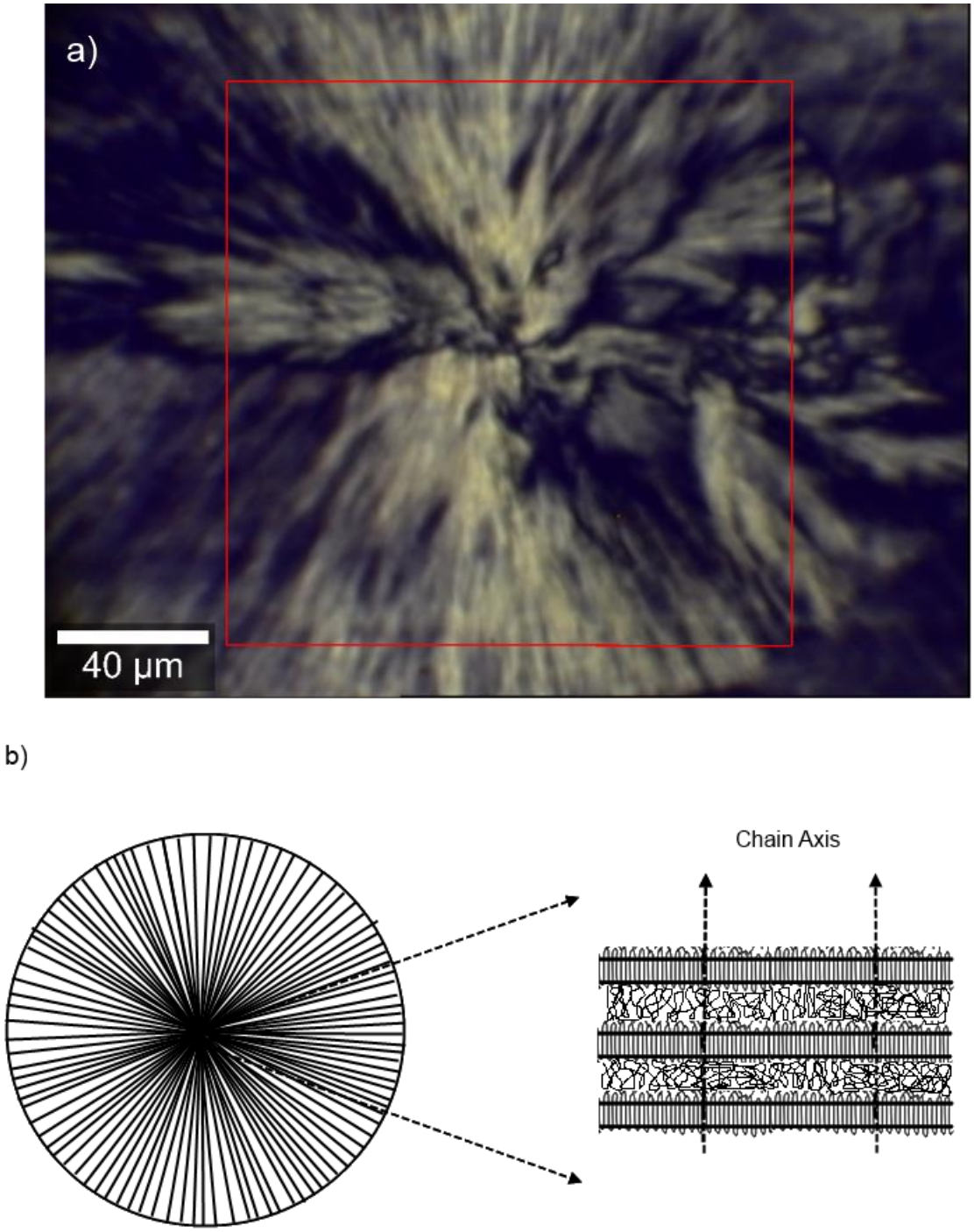

Figure 12: a) PLM image of the α-form of PP b) Schematic representation of the arrangement of polymer chains in lamellae and the direction of chain axis in an α- spherulite

The α- phase is the most predominant form of PP which shows a positive birefringence under polarized light. In α-PP, the macromolecular chains crystallize into a monoclinic unit cell structure and the latter has been shown to be the most thermodynamically stable of all the crystalline polymorphs of PP [90, 91].

4.3.1.2 Beta (β-) form of PP

The β- form of PP incorporates the macromolecular chains into a hexagonal unit cell wherein the lamellae are stacked radially from a nucleation point without cross hatching. The spherulitic structure in this case is known as sheaf like spherulitic structure. However, this form is less frequently observed being thermodynamically less stable and having a melting point which is 12-15 °C lower than that of the α-polymorph. The β- form generally appears under the application of shear stress or in the presence of certain nucleating agents such as NU-100®[92, 93]. β-spherulites are negatively birefringent under polarized light[94-96]. The PLM image of a β- spherulite and the arrangement of macromolecular chains are shown in

Figure 13.

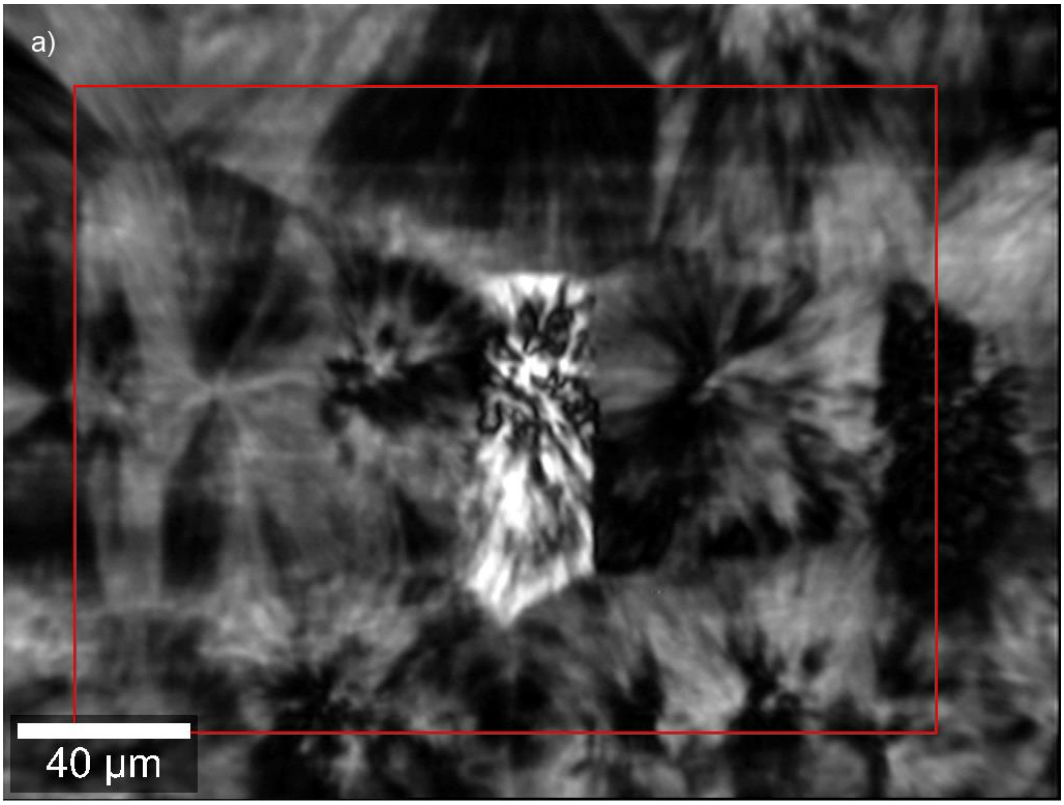

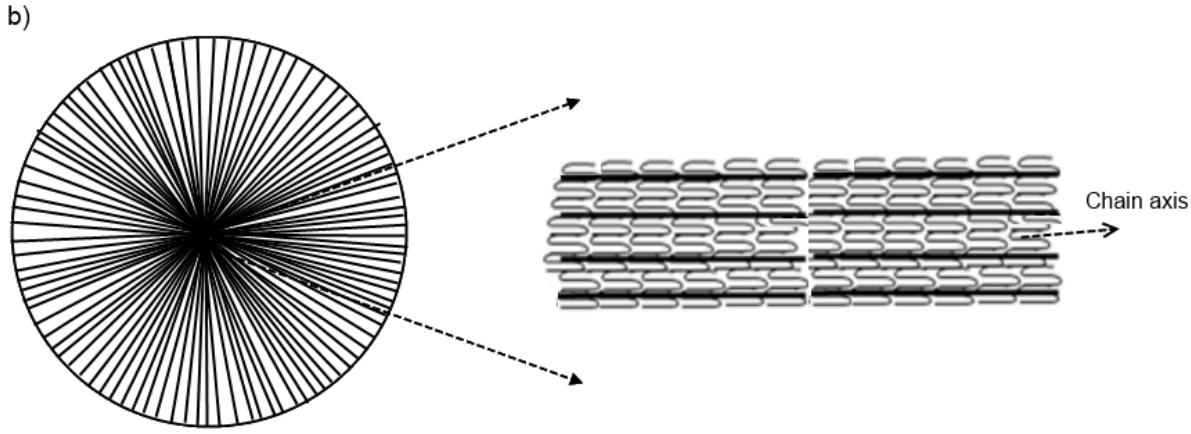

Figure 13: a) PLM image of the β -form of PP b) Schematic representation of the arrangement of polymer chains in lamellae and the direction of chain axis in a β spherulite

4.3.1.3 Gamma (γ) form of PP

The macromolecules in the γ-form of PP crystallize in an orthorhombic unit cell [97], which is usually associated with the α-form. The formation of the γ-phase is generally observed in low molar mass PP or when crystallization is carried out at elevated pressure [97, 98]. However, this form is rarely observed.

4.3.2 Applications of polypropylene

The versatility of PP in terms of its ability to adapt to a wide range of fabrication methods and applications has seen the demand for PP increasing steadily. PP can be processed by virtually all thermoplastic-processing methods such as: Extrusion, Blow Molding and Injection Molding. Hence, PP can be easily confectioned to films, non wovens, fabrics, and a wide range of semi-finished articles. The uses of PP envelop a wide range of industries covering automotive, construction, packaging and textiles (Figure 14)[99].

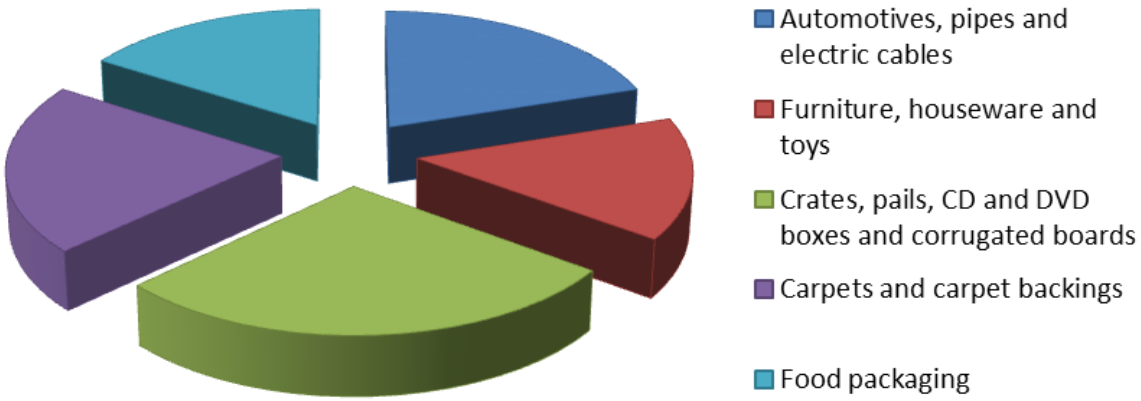

Figure 14: Schematic diagram showing the applications of PP in various industrial segments

PP is widely used [100] because it offers the chance for:

- Cost reduction
- Weight reduction
- Design opportunities

4.3.3 Processing and welding of PP and the effect of the morphology and X_C

Due to the ease of processing paired with properties such as a high temperature resistance, low density and heat conductivity, PP is widely used for manufacturing of pipes and plumbing components. Additional, advantages in this field of application are ease of installation, long term resistance towards internal pressure, a high resistance to chemical degradation and easy weld ability.

Welding is a widely used technique which involves merging or joining of two or more components. In welding of plastic materials, the joining takes place without the addition of any foreign material wherein the two materials are joined together, regularly under the application of thermal processes. However, welds are always weak points with regard to mechanical properties and are highly susceptible to cause failure of the sample under load. During the process of welding, the joint surfaces undergo melting followed by solidification. Different welding techniques like butt welding, IR welding, hot gas welding etc. are used to join plastics. Butt welding is a highly versatile welding process [49], which is regularly applied to join injection molded semi-finished products and pipes for installations. During butt welding, the two plastic components are brought in contact with a heated metallic plate until the polymer melts. The melted surfaces are compressed by applying a constant pressure until the melt solidifies. An image showing injection molded plates and the weld joining these is shown Figure 15.

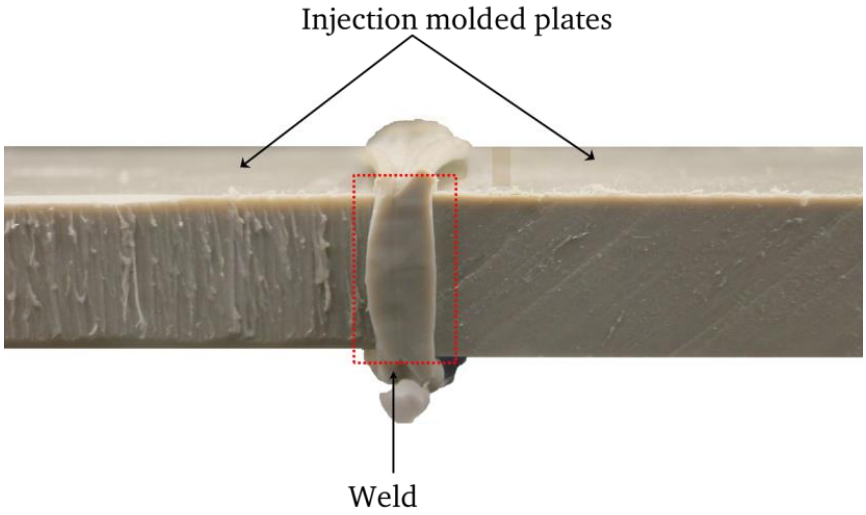

Figure 15: Welded sample showing the injection molded plates and the weld

Anisotropies are regularly induced in the melt during processing and welding of PP due to shear forces, giving rise to structural variations. The latter embody themselves in the form of spatial variations in morphology, with their length scale and variance depending on the specific process and conditions. These in turn have a significant impact on the macroscopic properties, such as mechanical properties and crack propagation[1-3]. Hence, spatially mapping the morphology in a comprehensive manner is an important task in order to establish process→structure→property relationships and use these to optimize manufacturing [101].

For identification of the polymorphs and determining the X_c in PP, Raman spectroscopy has been utilized previously being sensitive to both the crystalline and amorphous phases of the polymer as well as to the polymorphic composition [102, 103]. Thus, the technique has been used to probe the X_c of PP, and the band shifts in the spectra have also been used to distinguish between the α- and β-polymorph [103]. Nielsen et al. developed a method to calculate the X_c of PP by analyzing the spectrum in the range from 800-900 cm^{-1}. The band at 809 cm^{-1} was assigned to the chains in the helical conformation in the PP crystal [104]. The band at 841 cm^{-1} was assigned to shorter chains in the helical conformation and a band of low intensity at 830 cm^{-1} was assigned to chains in the non-helical conformation. X_c was hence calculated by taking

the ratio of the intensity of the band at 809 cm^{-1} to the total intensity of the bands at 809 cm^{-1}, 830 cm^{-1} and 841 cm^{-1}. The intensity sum was found to be constant over a wide range of temperature and was assigned as a reference for calculating the X_c. Hence the X_c of PP determined by the Raman spectra is given by

$$X_c = I_{809} / (I_{809} + I_{830} + I_{841}) \quad 16$$

Using the sensitivity of the Raman spectra to the polymorphic structure, Martin et al. have utilized a positive Raman shift in the characteristic bands of PP for identification of the β-polymorph [103].

Quantifying the crystalline morphology in a spherulite remains a big challenge and several attempts have been made to determine the distribution of X_c across a spherulite. Gatos et al. [105] studied the isothermal crystallization of iPP and evaluated the X_c as single point measurements along the diameter of a growing α-spherulite by using Raman spectroscopy. They mapped the crystalline domains in the whole spherulite by etching the amorphous regions within a spherulite with permanganate and then profiled the crystalline domains across the whole spherulite using Atomic Force Microscopy (AFM) in tapping mode. However, AFM measurements cannot generate quantitative information about the spherulite crystallinity as it is based on monitoring the surface density where quantification of the X_c is not possible. Small Angle X-Ray Scattering (SAXS) and Wide angle X-Ray Scattering (WAXS) have also been used to probe the X_c across PP spherulites. However, X-ray beams have a diameter of 0.1 - 2.0 mm and thus the structural information generated is spatially averaged, which is why the spatial resolution is insufficient to determine variations in X_c on the length scale of a spherulite [106]. Micro SAXS-WAXS has been used to investigate the morphology of PP spherulites, however a spatial profiling across the whole spherulite has not been reported[106-108]. This can be attributed to the requirement of a synchrotron beam source for achieving a higher resolution, making laboratory measurements unfeasible. Hence, it is valuable to have a method which can provide quantitative information about the X_c distribution across a spherulite at a high resolution and also distinctly identify the two different polymorphs of PP.

A strong need for such a method exists when investigating morphology variances on small length scales, e.g. in interfaces between materials. One example for this is across welds, where a complex interplay between the heating and cooling patterns as well as the mechanical forces due to shearing determines the morphology. The weld can often act as a weak point for sample failure, which makes it necessary to characterize the morphological structure in the weld channel [109]. The dimensions of the weld depend on the specific process used and typically lie in the range of a few mm for the case of butt welded PP. The major variation of the above mentioned parameters is expected along the weld seams, which are less than 100 μm in width. DSC, Polarized Light Microscopy (PLM) and Fourier Transform Infrared microscopy (μ FT-IR) have been used previously to study these variations in welded samples [109-112]. PLM cannot provide quantitative information about the changes in crystallinity and is indifferent to the sample composition. Mechanical abrasion→DSC and μ FT-IR on the other hand are limited to their spatial resolution, wherein the fine structure of the weld seams cannot be investigated.

In this study we want to show how Raman microscopy can be utilized to profile the morphology across welds at a high resolution. For this purpose bands will be identified, which allow to identify the polymorphic composition. Using this methodology the potential of Raman microscopy for the analysis of welds will be demonstrated.

5. Experimental Section

5.1 Determining the comonomer content in ethylene-1-olefin copolymers using Raman spectroscopy

5.1.1 Samples:

The samples used are detailed as in Table I below. All samples were synthesized using metallocene catalyst systems.

Table I: Sample description

Copolymer type	Notation	Content [Mol % NMR]	Dispersity	Supplier
ethylene/1-butene	E_{BUT}	1.57 – 10.32	3.2-4.3	Braskem, Brazil
ethylene/1-hexene	E_{HEX}	2.2 – 20.7	1.8-2.9	O. Boyron, Univ. of Lyon, Lyon France
ethylene/1-octene	E_{OCT}	0 – 13.9	2-2.2	The Dow Chemical Company, USA
ethylene/1-octadecene	E_{OCTD}	1.7-3.3	1.9-2.6	O. Boyron, Univ. of Lyon, Lyon France
ethylene/norbornene	E_{NOR}	24.5 – 60.75	1.8-1.9	Topas Advanced Polymers GmbH, Germany

5.1.2 Experimental parameters

Raman Spectroscopy

Raman measurements were carried out using a WITec alpha 500 spectroscopy system. For measurements on pellets/powders, a 20× (NA 0.4) microscope objective was used to focus the laser beam and to collect the scattered light. Laser radiation having a wavelength of 532 nm with a power of about 50 mW was employed as an excitation source. The scattered light was analyzed in a 600 mm^{-1} grating spectrometer at a spectral resolution of about 1 cm^{-1}. After focusing the sample manually with the microscope, the laser spot was positioned to accumulate a single spectrum with an acquisition time of 2 s and 10 accumulations were carried out per measurement. Each spectrum was smoothened by using a Savitzky-Golay method and background subtraction.

5.2 Determining the percentage crosslinking in EVA Photovoltaic modules using Raman microscopy

5.2.1 Samples

EVA encapsulant material

The EVA resin (Evatane 28-40 from Arkema, containing 28.3 mol % vinyl acetate, was conditioned with 1 wt. % *t*-butylperoxy (2-ethylhexyl)carbonate (TBPEHC from United Initiators; CAS: 34443-12-4) and 0.7 wt. % of the crosslinking booster triallyl isocyanurate (TAICROS® from Evonik; CAS: 1025-15-6), 0.3 wt. % of the adhesive promoter γ-methacryloxypropyltrimethoxysilane (Dynasylan® Memo from Evonik; CAS: 2530-85-0) as well as stabilizers in typical amounts.

The EVA/additive mixture was extruded on a lab-extruder (Collin) having a 10 cm flat film extrusion die. The extrusion temperature was 77 °C - 80 °C, whereas the melt temperature was 88 °C. The encapsulant film was winded up with a cooled chill-roll system. Lamination of the EVA encapsulant film (0.8 mm thick) was done between two Teflon sheets. According to the sample description below (Table 1) the lamination time was varied between zero and 20 min. The temperature setting was 150 °C and the pressure 0.7 kg/cm² (second step after applying vacuum).

Table 2: Sample description

Sample No.	Lamination time [min.]
V1	0
V2	3
V3	5
V4	8
V5	12

V6	15
V7	20
V8*	20
V9#	20

* Sample V8 was made with the same composition as above, but with 0.8 wt. % tert.-butylperoxy (2-ethylhexyl) carbonate, 0.5 wt. % of the crosslinking booster triallyl isocyanurate, and without any added adhesive promoter.

Sample V9 was made with the same composition as samples V1-V6. The lamination in this case was carried out between two sheets of quartz glass having a thickness of 1 mm.

5.2.2 Experimental Parameters

Soxhlet extraction

The percentage crosslinking was determined using toluene and 1 g (M_1) of the polymer in a Soxhlet hull (porosity 0.1 mm). The toluene dissolved the non-cross-linked material and flushed it out from the hull. The cross-linked polymer was then left in a swollen state in the hull and the residual solvent was removed in vacuum at 100 °C. This left over material was then weighed (M_2) and the degree of crosslinking was determined. Three measurements were carried out per sample.

Differential scanning calorimetry

Circular samples with a diameter of 5 mm (ca. 10 mg) were cut out from the EVA laminates and were analyzed using a Mettler Toledo DSC 822e, which was calibrated with high purity indium and zinc standards. All samples were measured using a heating rate of 10 °C/min under an inert atmosphere of nitrogen between 25 and 230 °C, and the first heating cycle was used for analysis. Five measurements were carried out per sample.

FT-IR Spectroscopy

The measurements were recorded in ATR mode on a Nicolet 8700 spectrometer equipped with a MCT-A detector. Three measurements were carried out per sample at a spectral resolution of 4 cm^{-1}. A background spectrum was recorded before each sample analysis, and 16 scans were carried out per measurement.

Raman Spectroscopy

Raman measurements were carried out using a WITec alpha 500 system. For measurements on samples a 50× (NA 0.8) microscope objective was used to focus the laser beam and to collect the scattered light. Laser radiation having a wavelength of 532 nm with a power of about 50 mW was employed as an excitation source. The scattered light was analyzed in a 600 mm^{-1} grating spectrometer at a spectral resolution of 1 cm^{-1}. After localizing the sample and focusing manually with the microscope, the laser spot was positioned to accumulate a single spectrum with an acquisition time of 2 s, and 10 accumulations were carried out per measurement. Each spectrum was smoothed using the Savitzky-Golay method and background subtracted. Ten independent measurements were carried out to obtain the spectrum from each EVA foil. The crosslinking inhomogeneities were measured by analyzing an area of 3000 x 3000 μm at a step width of 7.5 μm obtaining a total of 160000 spectra. The high resolution measurement to analyze minor crosslinking inhomogeneities was carried out by measuring an area of 100 x 100 μm with a step width of 0.5 μm obtaining 40000 individual spectra. The measurement under the glass laminate was carried out by measuring an area of 5000 x 5000 μm at a step width of 16 μm obtaining 90000 individual spectra.

5.3 Investigating the morphological variations due to processing and thermo-mechanical treatment of polypropylene using Raman microscopy

5.3.1 Samples

Plates made from a PP-H and PP-R (8 mol-% ethylene) by injection molding were joined by butt welding. The values of parameters used for injection molding and welding are tabulated in Table 1 and Table 2.

5.3.2 Experimental Parameters

Parameters used for welding

Table 3. Parameters used for injection molding the plates

Parameter	
Injection time (s)	1.64
Hold pressure time (s)	25
Cooling time (s)	25
Melt temperature (°C)	220

Table 4. Parameters used for welding

Parameter	
Hot plate temperature (°C)	220

Hold pressure time (s)	190
Cooling time (s)	180

Polarized light microscopy

A microscope (BX50 F, Olympus) equipped with UPlan objectives, a rotatable polarizer (U-POT), analyzer (U-AN360) and a compensator plate (U-TP530) was used for PLM. The microtome sections (cuts of 10 μm thickness) were fixed onto glass slides using an acrylate resin.

Differential scanning calorimetry

Circular samples with a diameter of 5 mm and a thickness of 300 μm (ca. 5 mg) were microtomed from the plates of PP-H and analyzed. All samples were measured using a heating rate of 10 °C/ min under an inert atmosphere of nitrogen between 25 and 230 °C, and the first heating cycle was used for morphological analysis. The heat of fusion of completely crystalline α- and β-crystalline iPP was taken as 177 J/ g and 168 J/ g, respectively [2].

X_c was calculated from the melting endotherm according to [2] (Eqs. 17-20).

$$X_c^{DSC} = \frac{\Delta H}{\Delta H^0} \cdot 100 \qquad 17$$

where ΔH is the actual enthalpy of fusion and ΔH^0 is the enthalpy of fusion for 100 % crystalline material. However, due to the presence of polymorphism in PP-H1, ΔH^0 consists of the contributions of both the α- (ΔH_α^0) and β- (ΔH_β^0) form (Eq. 18).

$$\Delta H^0 = K_\alpha . \Delta H_\alpha^0 + K_\beta . \Delta H_\beta^0 \qquad 18$$

The fractional percentages of the total X_c^{DSC}, K_α and K_β, were determined separately as defined in eq. 19 and 20.

$$K_\alpha = \frac{\frac{\Delta H_\alpha}{\Delta H_\alpha^0}}{\frac{\Delta H_\beta}{\Delta H_\beta^0} + \frac{\Delta H_\alpha}{\Delta H_\alpha^0}} \quad 19$$

$$K_\beta = \frac{\frac{\Delta H_\beta}{\Delta H_\beta^0}}{\frac{\Delta H_\beta}{\Delta H_\beta^0} + \frac{\Delta H_\alpha}{\Delta H_\alpha^0}} \quad 20$$

μFT-IR

Cuts of 50 μm thickness were prepared using a Reichert Jung rotary microtome. An IR microscope (Continuum, Thermo Nicolet (Madison, WI)) equipped with an MCT-A detector was used for analysis. It was coupled to a Nicolet-Nexus 670 FT-IR spectrometer as beam source. Hundred scans were accumulated per spectrum in transmission mode with an aperture of 50 x 50 μm^2. Line scans were performed with a step width of 25 μm. A micro-vice sample holder was used to fix the samples. X_c was calculated from μFT-IR using the method reported in [113] (Eq. 21).

$$X_c = \frac{\alpha_{974}}{\alpha_{841}} \cdot \frac{A_0^{841}}{A_0^{974}} \cdot 100 \quad 21$$

A_0^{841} and A_0^{974} are the absorbance of the peaks at 841 and 974 cm^{-1}, respectively. α_{974} and α_{841} are the absorption coefficients of the respective peaks, and the ratio between these has been reported to be 0.79 [28].

Raman Microscopy

A 50× (NA 0.8) microscope objective was used to focus the laser beam and to collect the scattered light. Laser radiation having a wavelength of 532 nm with a power of about 20 mW was employed as an excitation source. The scattered light was analyzed in a 600 mm^{-1} grating spectrometer at a spectral resolution of about 1 cm^{-1}. Each spectrum was smoothened by using a Savitzky-Golay method and background subtracted. Morphological variations in spherulites were investigated by mapping a region of 70 x 70 μm^2 for the β-spherulite, acquiring 44100 individual spectra at a step width of 0.3 μm. The α-spherulite was also mapped with the same resolution, and an area of 80 x 70 μm^2 was investigated acquiring a total of 56000 spectra. The weld fabricated from PP-H was investigated at a step width of 2 μm and a region of 800x 400 μm^2 was mapped obtaining 80000 spectra. The weld fabricated from PP-H and PP-R was investigated at a step width of ~1 μm and a region of 500 x 200 μm^2 was mapped obtaining 90000 spectra. The acquisition time for each individual spectrum was 0.1 s.

6. Results and Discussions

6.1 Determining the comonomer content in ethylene-1-olefin copolymers using Raman spectroscopy

The Raman spectra of E_{OCT} copolymers with a comonomer content ranging from 0 – 13.9 mol % in the range of the C-C stretching and the deformation vibrations of CH_2 and CH_3 groups are shown in Figure 16.

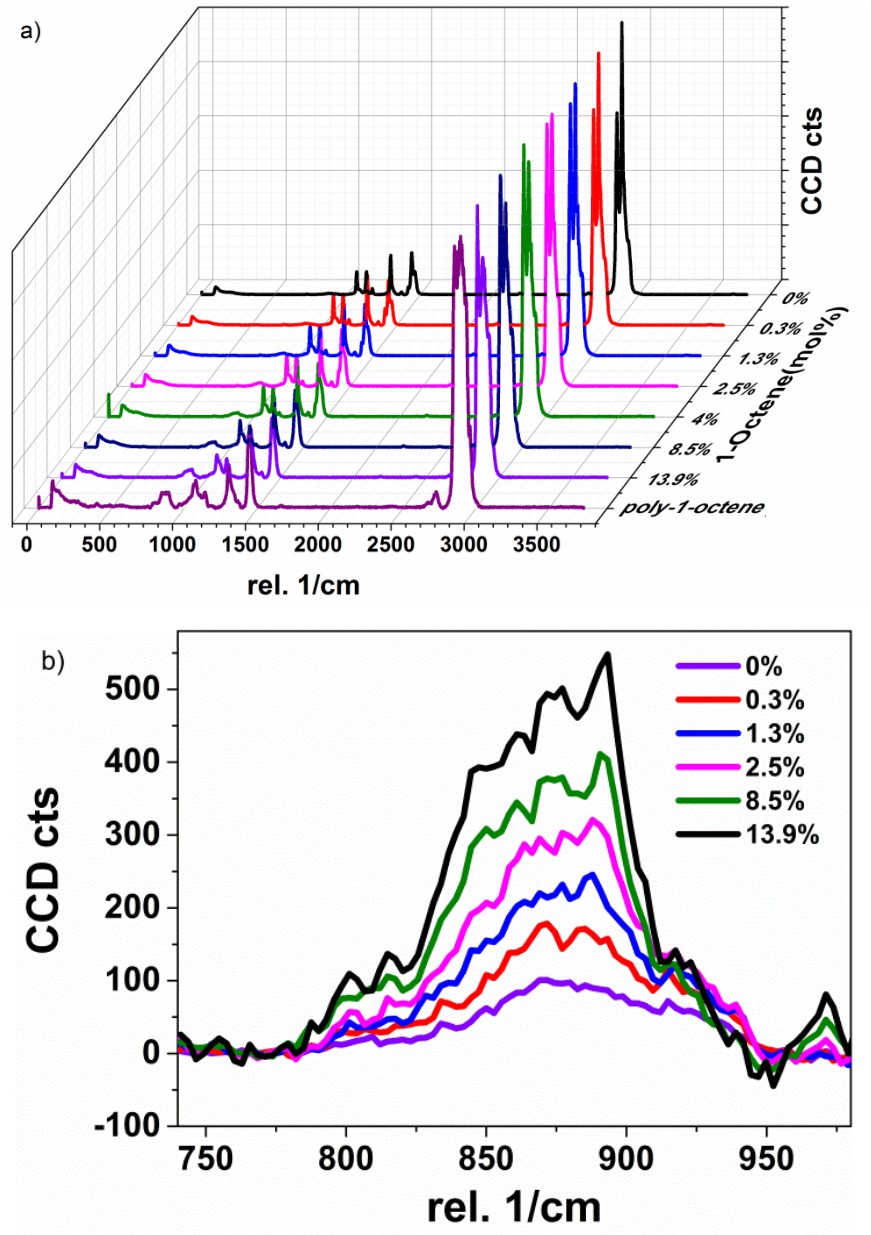

Figure 16 : a) Raman spectra of E_{OCT} with varying 1-octene content and b) Raman spectra of E_{OCT} showing the band ensemble below 1000 cm^{-1}

The spectra show pronounced changes with increasing content of the comonomer. The characteristic bands for the ethylene sequences show a marked decrease in intensity and simultaneously the intensity of the band at 1416 cm^{-1}, which has been widely used to measure the degree of crystallinity [50], also decreases. The bands in the C-C stretching region assigned at 1058 cm^{-1}, 1126 cm^{-1} and 1166 cm^{-1}, the twisting region at 1295 cm^{-1} and the bending region at 1439 cm^{-1} [49] follow a similar trend. Interestingly, the frequency region below 1000 cm^{-1} shows a band ensemble which is

characteristic for the 1-octene comonomer as can be recognized from the spectrum of poly-1-octene. This band ensemble, normalized with respect to the highest intensity band at 1058 cm^{-1}, shows a significant increase in intensity with comonomer incorporation (Figure 16 b).

A method to determine the crystallinity of PE by Raman spectroscopy was developed by investigating the spectra of bulk-crystallized PE [48]. The spectra were analyzed to determine the content of the three distinct polymorphs, namely the orthorhombic crystalline phase, a melt like amorphous phase, and a disordered anisotropic phase. The intensity of the band at 1416 cm^{-1} was used to deduce the relative fraction of segments present in the orthorhombic phase (α_c). The relative amount of segments forming the liquid like amorphous phase (α_a) was obtained from two bands centered in the twisting region at 1303 cm^{-1} or in the stretching region at 1080 cm^{-1}. The interfacial phase (α_b) was proposed as a domain wherein the chains are in the extended *trans*-configuration and have lost their lateral order[49]. The relative amount of segments forming this phase was calculated as $\alpha_b = 1 - \alpha_a - \alpha_c$. With increasing 1-octene content the Raman band characteristic for measuring the crystallinity in the ethylene segments at 1416 cm^{-1} decreases in intensity and remains as a small shoulder in the sample with 8.5 mol % 1-octene. Similarly, with the increase in comonomer content the band at 1166 cm^{-1} merges with the more intense band at 1126 cm^{-1}. The alkyl branches of the comonomer are not able to enter the crystal lattice [51], and hence an increase in the fraction of α_a and α_b is observed.

Thus, the Raman spectra reflect the effect of the decrease in band intensity of the characteristic bands from the PE segments due to the decrease in the ethylene content, the effect of the comonomer segments seen as a band ensemble and the associated changes in the phase composition due to comonomer incorporation. Broadening has also been observed in these characteristic PE bands, which is deduced to be due to the increasing content of 1-octene which shows several bands overlapping in the same frequency region as the PE segments (Figure 16b). The above three effects limit using solely the Raman bands of the ethylene segments to determine the comonomer content. However, before selecting suitable bands for

quantification it has to be taken into account that the intensity of the Raman spectra varies to a great extent with experimental parameters, taking in the first instance the acquisition time and the sample focus/depth [114]. For illustration, Figure 17 shows the Raman spectra of linear PE measured with different acquisition times after being focused with the microscope.

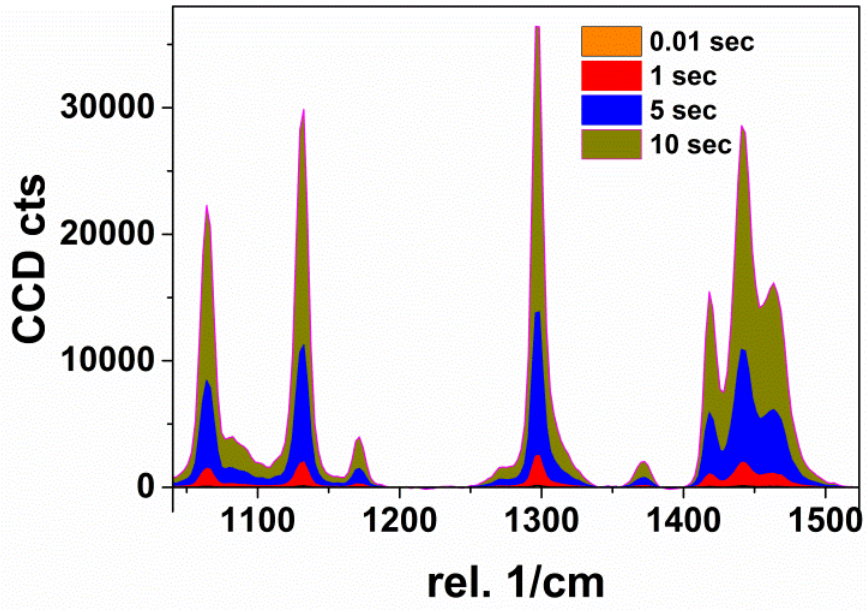

Figure 17: Variation in signal intensity of the Raman spectra of linear PE with spectral acquisition times.

A clear dependence of the signal intensity on the acquisition time can be seen, and the intensity of the Raman signal increases with the spectral acquisition time. Additionally, in order to maximize the signal intensity and reduce the signal/noise ratio, spectral acquisition has to be preceded by proper focusing of the sample. The latter is, however, a very subtle parameter often depending on the skill of the operator, and even a few microns shift in the sample focus can have a significant influence on the signal intensity. This in turn would have a direct impact on the height /area (I) of individual bands, thus again reducing their applicability as the sole criterion to determine the comonomer content in samples. Figure 18 shows this effect where a sample was focused manually (same spectral acquisition time) and then Raman spectra were acquired at one micrometer levels above and below the sample.

The intensity of the bands at 1295 and 1439 cm^{-1} has been plotted with the variation in sample height.

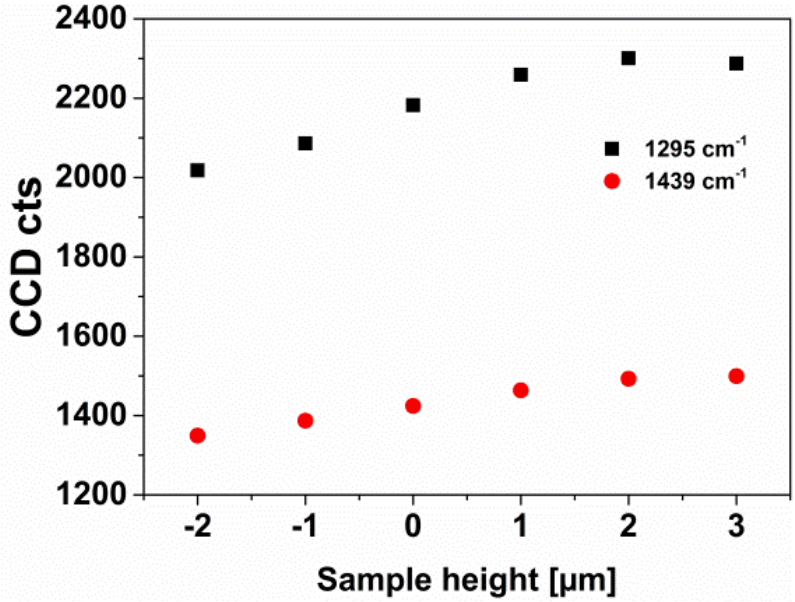

Figure 18: Effect of sample focusing on the scattering intensity the sample

A significant variation in band intensity is seen with the shift in focus above and below the sample.

Using an acquisition time of 2 seconds per spectrum and focusing the samples manually, the intensity of the band at 885 cm^{-1} in the band ensemble of E_{OCT} below 1000 cm^{-1} was correlated with the comonomer content as shown in Figure 19 below.

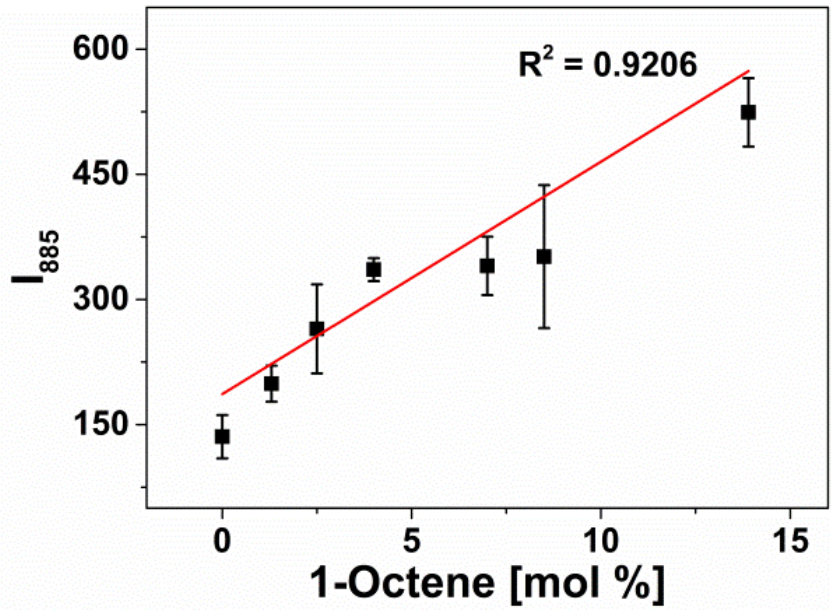

Figure 19: Band intensity I_{855} as a function of 1-octene content

The effect of the experimental parameters on the intensity of the band at 885 cm^{-1} for determining the comonomer content is evident in Figure 19 but the correlation with the comonomer content is non-linear. Thus, for developing a method to correlate these spectral changes upon comonomer incorporation and also eliminating the effect of the experimental parameters on the spectra, an internal intensity standard/reference for normalizing the intensity of the band ensemble is required. Hence, the ratio of the band intensities of the characteristic bands from the ethylene sequences to the characteristic bands emerging from the comonomer was investigated. An internal standard which minimizes the effect of the spectral overlap due to scattering from the comonomer sequences was determined. Normalizing the band intensity ratio would cancel out the effect of sample focusing, and thus reduce the number of parameters to find a suitable correlation for quantification. The high intensity bands characteristic of the PE segments at 1058 cm^{-1} (C-C stretching), 1126 cm^{-1} (C-C stretching), 1295 cm^{-1}(C-C twisting) and at 1439 cm^{-1}(C-C bending) were selected. The band ensemble characteristic for the comonomer from 700 cm^{-1}- 950 cm^{-1} shows four major bands at 844 cm^{-1}, 855 cm^{-1}, 875 cm^{-1} and 885 cm^{-1}, respectively. The ratio of the intensity of the strongest band amongst these at 885 cm^{-1} to the characteristic PE bands was probed to determine a correlation which

accounts for the effect of increasing comonomer content, the accompanying decrease in the ethylene content and intrinsic changes in the ratio of polymorphs. The band ratios with the respective standard deviation in the measurements in correlation with the comonomer content are presented in Figure 20.

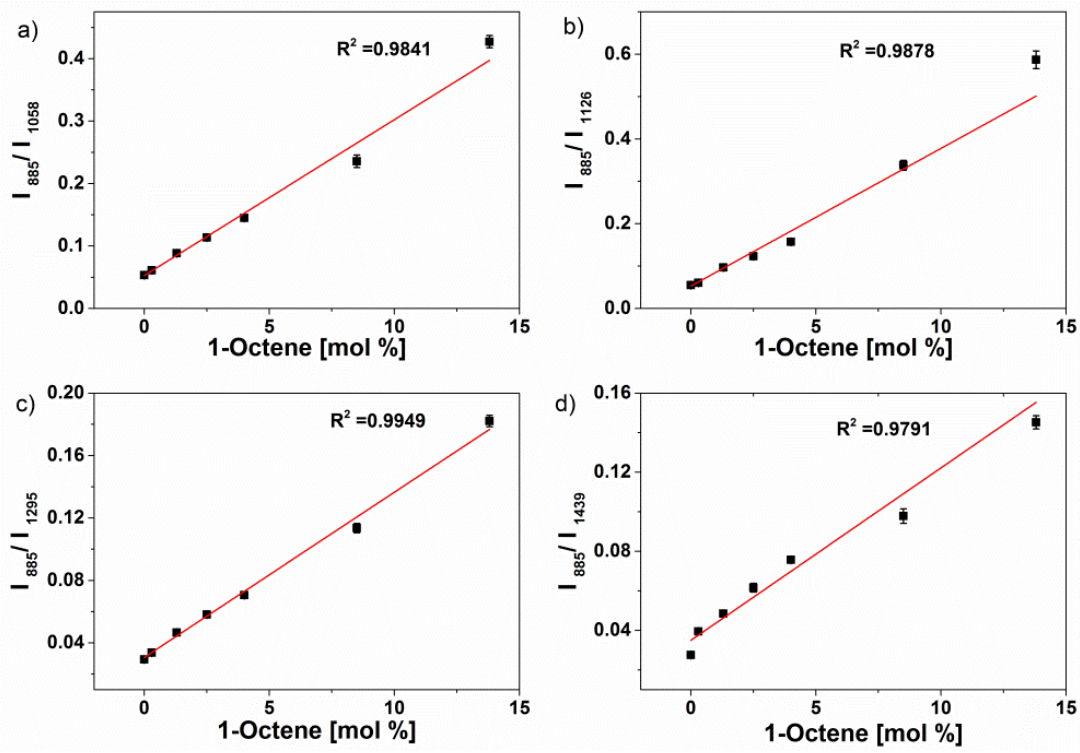

Figure 20: Band intensity ratios a) I_{855}/ I_{1058} b) I_{855}/I_{1126} c) I_{855}/I_{1295} d) I_{855}/I_{1439} plotted as a function of 1-octene content

As seen from Figure 20 the band at 1295 cm^{-1} in the C-C twisting region yielded the best correlation with an R^2 value of 0.9949. The band at 1439 cm^{-1} in the C-C bending region shows broadening and overlaps with a characteristic band of 1-octene at 1444 cm^{-1} yielding an R^2 value of 0.9791. This band is also seen to merge with the one at 1416 cm^{-1} used to determine the crystallinity of PE as discussed previously, and the combined effect of these two bands leads to a deviation from a linear correlation. The band at 1058 cm^{-1} in the C-C stretching region yields an R^2 value of 0.9841, but starts to develop a shoulder due to merging with the characteristic bands

of 1-octene at 1059 and 1080 cm^{-1} when the 1-octene content is increased. The other band in the stretching region at 1126 cm^{-1} gives an R^2 value of 0.9878 also merging with the band characteristic for the 1-octene comonomer at 1140 cm^{-1} showing non-linearity. Most of the characteristic Raman bands for 1-octene are in close vicinity to those for PE, however, the effect on the Raman scattering intensity of the C-C twisting mode was the least and was observed to fit excellently correlating with the comonomer content.

To verify the reproducibility and robustness of this method, ten independent measurements were carried out per sample, and a collective average of the band ratios was plotted. The deviation from the linear fitting was observed to be negligible, verifying the applicability and robustness of the method.

The Raman spectra of E_{BUT} with varying content of 1-butene (mol %) in the frequency range 600-1070 cm^{-1} are shown in Figure 21.

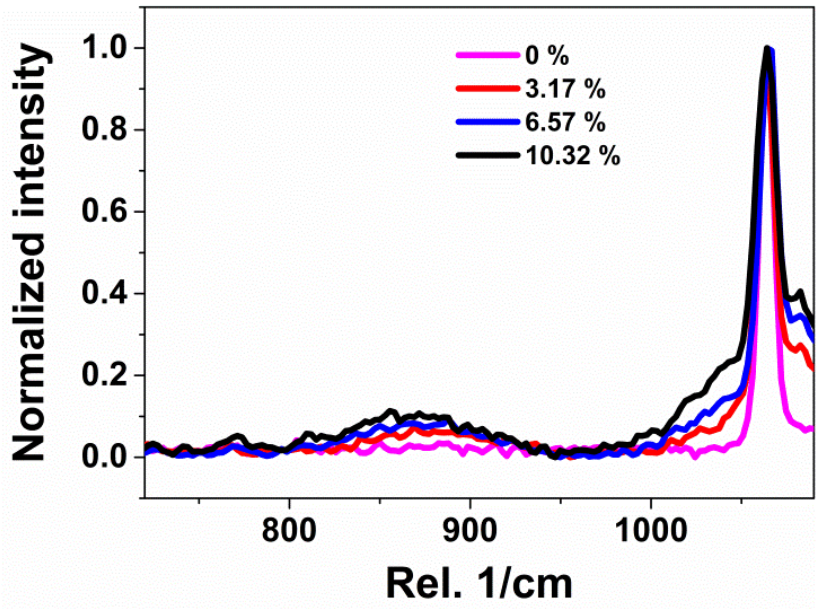

Figure 21: Raman spectra of E_{BUT} normalized to the high intensity band at 1058 cm^{-1}

With increasing comonomer content, similar changes in the Raman spectra as observed for E_{OCT} can be recognized for E_{BUT} with the decrease in intensity of ethylene sequences and the appearance of a band ensemble in the region below 1000 cm^{-1}. The latter shows a clear increase in intensity with increasing comonomer content, but was difficult to resolve in terms of individual bands due to the presence of several bands having similar intensity. On a closer inspection, the band at 869 cm^{-1} could be identified in the ensemble showing the highest variation in intensity with comonomer content. Using an analogous approach as for E_{OCT}, the bands from the three different modes of vibration for the ethylene sequences were selected to develop a method to quantify the 1-butene comonomer. The intensity of the band at 869 cm^{-1} was chosen for drawing out a correlation with the bands from the ethylene sequences to deduce a method for quantifying the content of E_{BUT}. Figure 22 shows the intensity ratio of the band at 869 cm^{-1} to those arising from the ethylene.

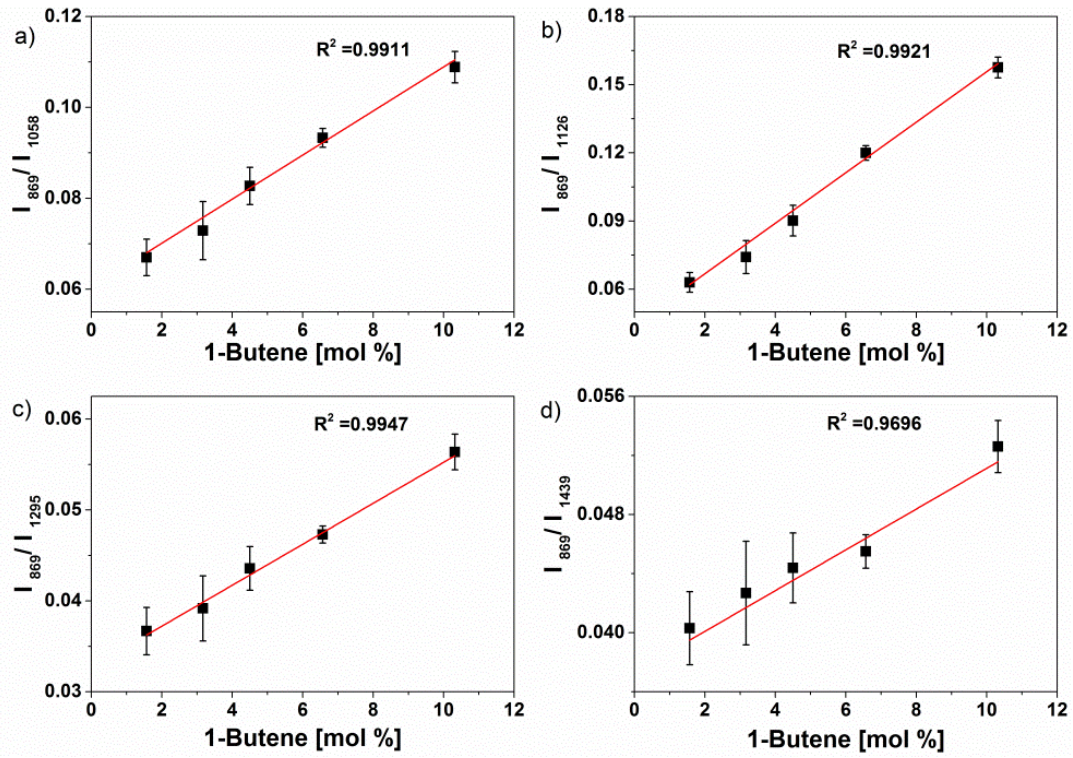

Figure 22: Band intensity ratios a) I_{869}/ I_{1058} b) I_{869}/I_{1126} c) I_{869}/I_{1295} d) I_{869}/I_{1439} as a function of 1-butene content

In this case as well, the intensity ratio of the band at 869 cm^{-1} to the band in the C-C twisting region at 1295 cm^{-1} showed a more accurate correlation with the 1-butene content than the bands in the stretching and bending regions. The band at 1439 cm^{-1} in the C-C bending region was particularly influenced by scattering stemming from the band of the 1-butene sequences giving an R^2 value of 0.9696. Hence, the effect of the spectral overlap of the scattering from the 1-butene sequences with the ethylene sequences and its relation with the characteristic band of the 1-butene sequences found the best synchronization with the band at 1295 cm^{-1} yielding an R^2 value of 0.9947 for quantification of E_{BUT}.

The Raman spectra of E_{HEX} with varying content of 1-hexene (mol %) in the frequency range from 600-1070 cm^{-1} are shown in **Figure 23**.

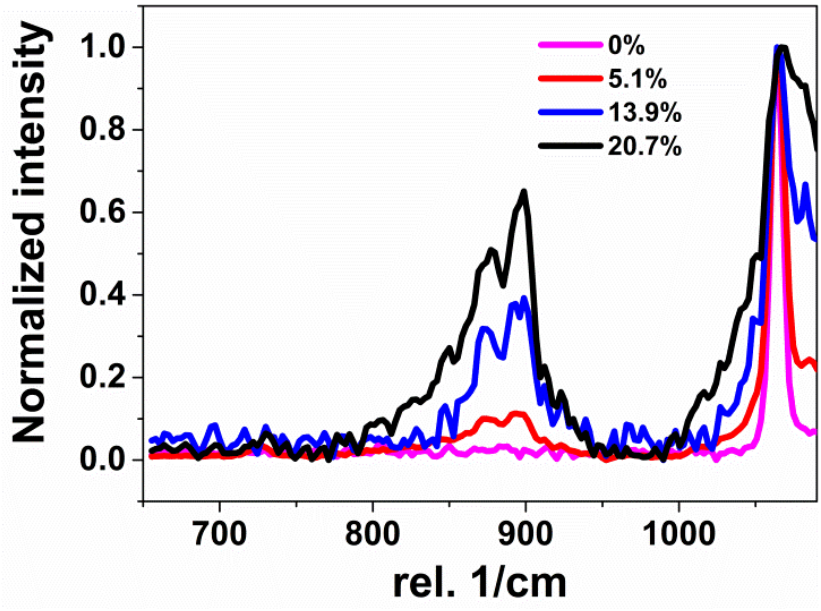

Figure 23: Raman spectra of E_{HEX} normalized to the high intensity band at 1058 cm^{-1}

E_{HEX}, similar to E_{OCT} and E_{BUT} also shows a band ensemble in the frequency region below 1000 cm^{-1} which grows in intensity with comonomer incorporation. The ensemble shows the presence of two prominent bands at 879 cm^{-1} and 893 cm^{-1}, with the one at 893 cm^{-1} being dominant, and in addition showing a variation in intensity

with 1-hexene content. Therefore, the latter was selected as representative of 1-hexene and was used to find a correlation with the characteristic bands in the different vibrational regions for the ethylene sequences as selected earlier. The effect of band overlap and changes in the bands from the ethylene sequences was studied and the best fit for obtaining the 1-hexene content through the Raman spectra of E_{HEX} was identified (Figure 24).

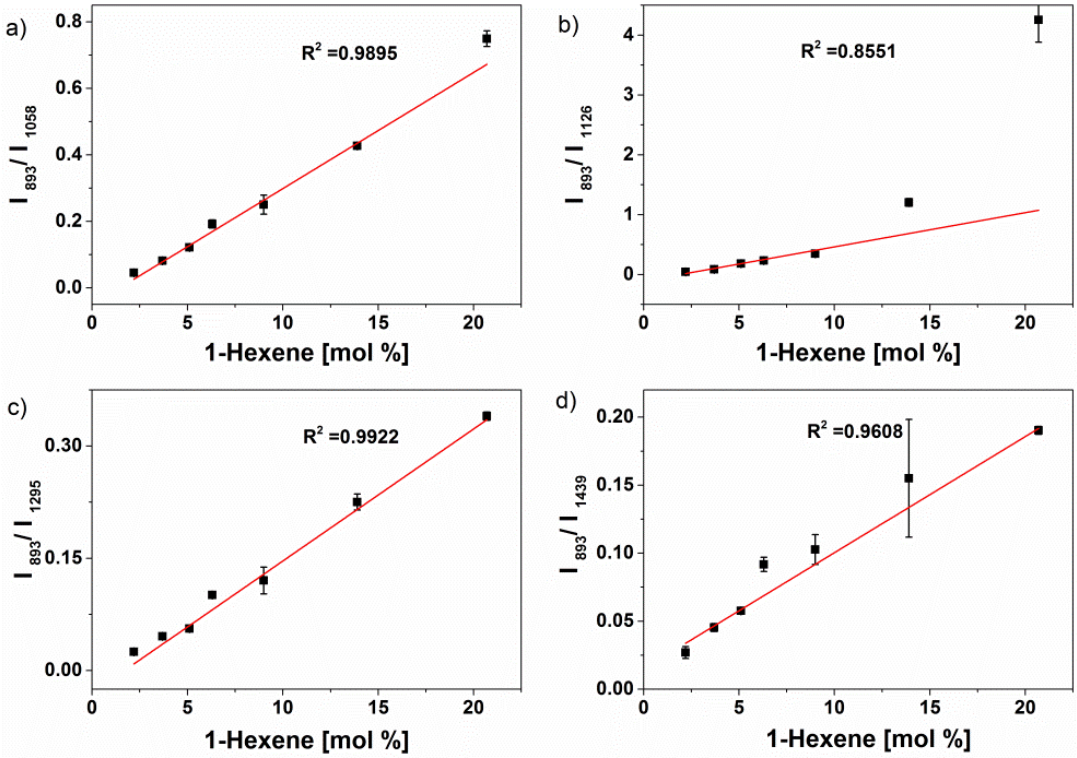

Figure 24: Band intensity ratios a) I_{893}/ I_{1058} b) I_{893}/I_{1126} c) I_{893}/I_{1295} d) I_{893}/I_{1439} as a function of 1-hexene content

In this case, similar to E_{OCT}, the best correlation was found with the intensity ratio of the band at 893 cm^{-1} characteristic of the 1-hexene comonomer to that of the band in the C-C twisting region at 1295 cm^{-1} yielding an R^2 value of 0.9922.

The Raman spectra of E_{OCTD} with varying content of 1-octadecene (mol %) in the frequency range from 600-1070 cm^{-1} are shown in Figure 25.

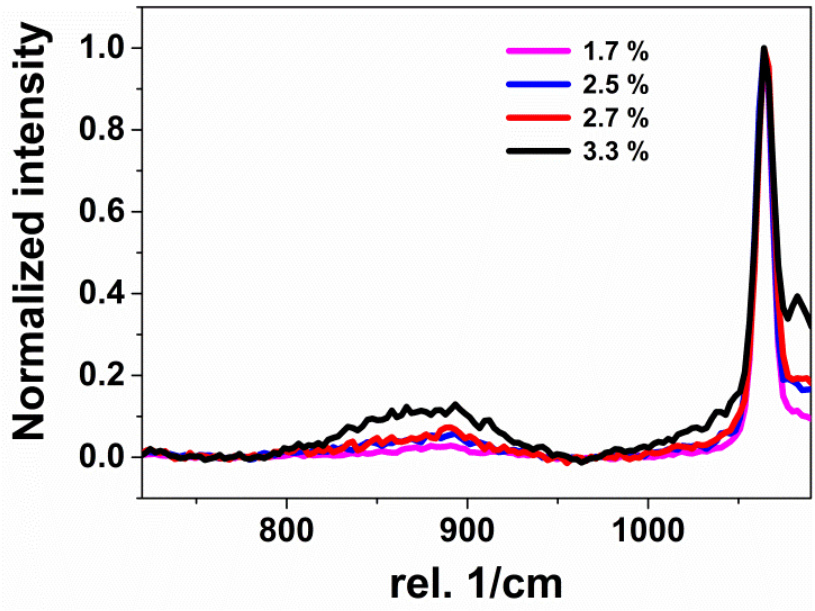

Figure 25: Raman spectra of E_{OCTD} normalized with regard to the high intensity band at 1058 cm^{-1}

The spectra show the appearance of a band ensemble in the low frequency region below 1000 cm^{-1} as seen previously for other 1-olefins. The increasing content of 1-octadecene is also characterized by an increase in the intensity of this ensemble, which becomes increasingly prominent with increasing comonomer content. Quantification of E_{OCTD} was carried out using a similar approach of choosing the band ratios of the most prominent band in the ensemble to the characteristic bands from the scattering caused by the bands specific for the ethylene sequences. The band ensemble in this case was clearly seen, and the highest intensity band at 896 cm^{-1} was used as a representative of the scattering from 1-octadecene and its correlation with the characteristic bands from the ethylene sequences was determined (Figure 26).

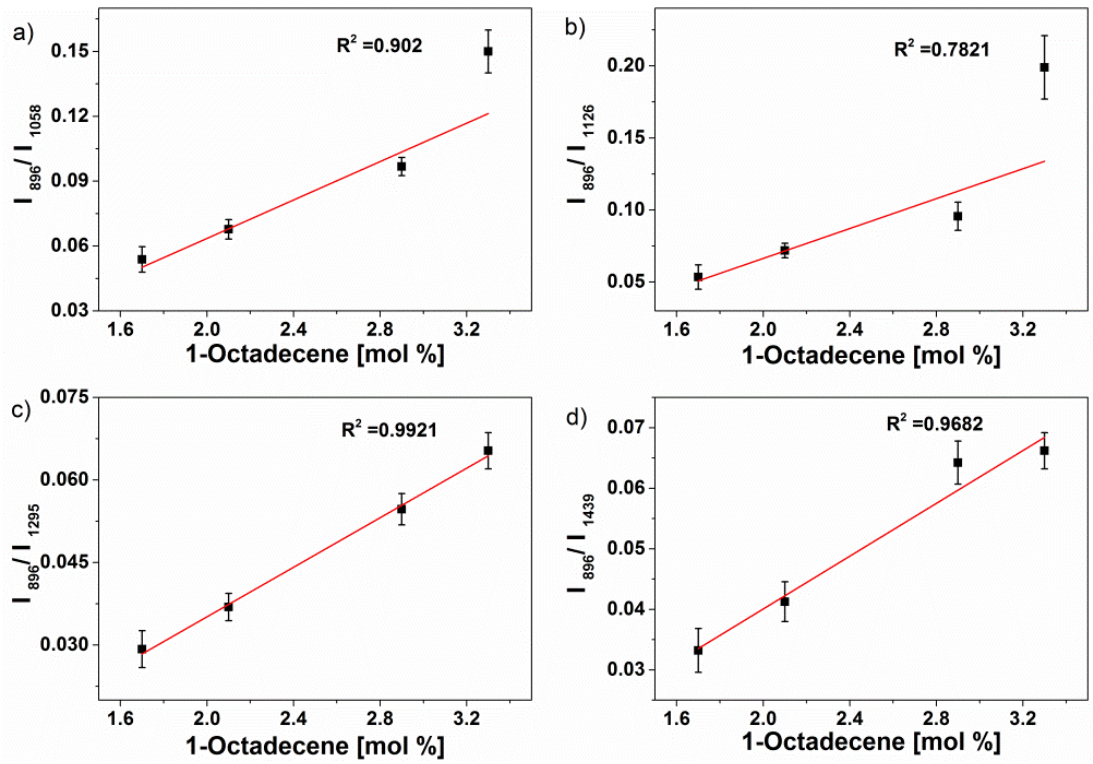

Figure 26: Band intensity ratios a) I_{896}/ I_{1058} b) I_{896}/I_{1126} c) I_{896}/I_{1295} d) I_{896}/I_{1439} as a function of 1-octadecene content

In this case for E_{OCTD} as well, the best linear correlation for determining the comonomer content was observed with the band in the C-C twisting region at 1295 cm^{-1} giving an R^2 value of 0.992. Here too, the effect of the spectral overlap of the scattering through 1-octadecene is pronounced in the C-C bending region.

Hence, it can be concluded that the band in the C-C twisting region at 1295 cm^{-1} can be used as an internal intensity standard for normalizing the intensity of the band ensemble to quantify the comonomer content of LLDPE. The Raman spectra of the comonomers from 1- butene to 1-octadecene have been studied and the intensity of the band at 1295 cm^{-1} to be used as an internal standard appropriate for quantification has been verified.

6.1.1 Quantification of the comonomer content in Copolymers of Ethylene with Cyclic Olefin Copolymers (COC)

An interesting question is, if such a method to quantify the comonomer content can also be applied to ethylene copolymers of low crystallinity. Cyclic Olefin Copolymers (COCs) are commercially important materials, which due to their superior optical, mechanical, thermal and water barrier properties find a wide range of applications ranging from packaging films, lenses, vials, displays, and medical devices. Norbornene is frequently incorporated as a comonomer with ethylene, including others such as cyclopentene and dicyclopentadiene [115, 116]. Copolymers of ethylene with straight chain aliphatic 1-olefins generally have lower comonomer content (up to 20 mol %) compared to COC's for which the commercially relevant comonomer content ranges from 20-60 mol %. Due to the high comonomer content, these materials are fully amorphous, and extending the applicability of this method to such amorphous materials would add another line of commercially important materials quantifiable non-destructively. At such a concentration of the comonomer the spectrum of the comonomer starts dominating, overlapping with the dominant bands of the ethylene sequences (Figure 27).

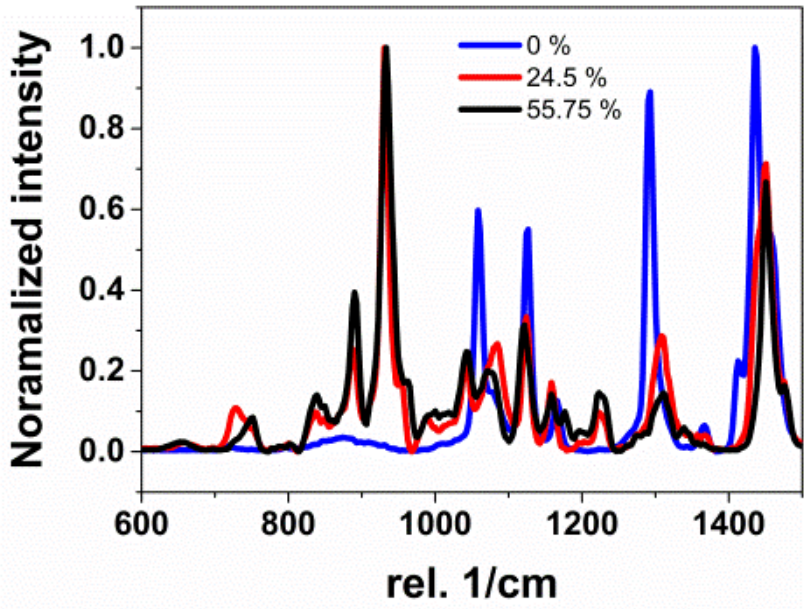

Figure 27: Raman spectra of E_{NOR}

The bridged cyclic structure in the copolymer gives rise to several high intensity bands from 500 cm^{-1}-1500 cm^{-1}. The bands solely characteristic of the ethylene sequences are not segregable easily apart from the band at 1439 cm^{-1} which can still be seen prominently. To determine the effect of the decrease in the percentage of the ethylene sequences and the increase in the norbornene content through the Raman spectra, the intensity of the band at 1439 cm^{-1} was selected and plotted with respect to the intensity of the band at 1313 cm^{-1} attributed to the cyclic comonomer.

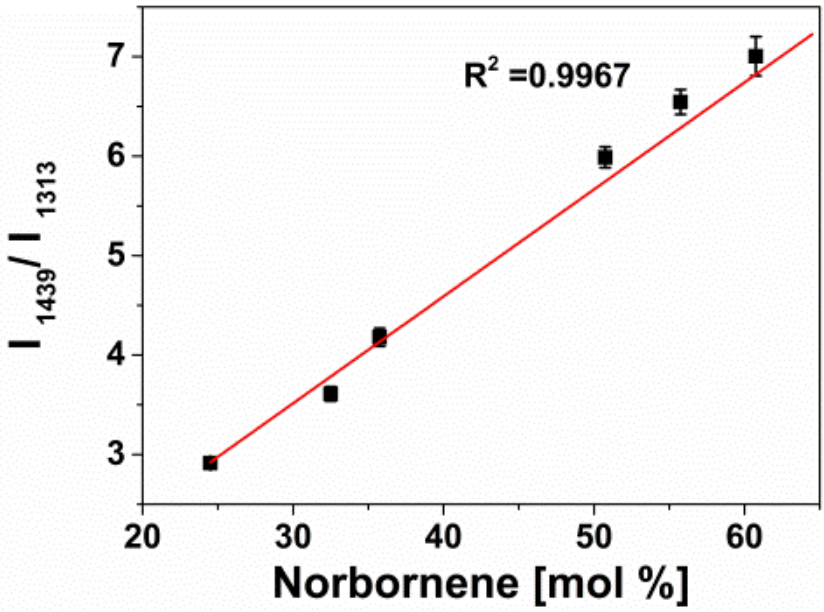

Figure 28: Band intensity ratio I_{1439}/ I_{1313} as a function of the norbornene content

A good linear correlation (Figure 28) substantiates the fact that the two bands chosen are appropriate to quantify the content of norbornene in COCs.

6.1.2 **Conclusions**

Quantification of the comonomer content in linear low density polyethylene is of enormous importance for many industrial applications such as quality control and sample identification. NMR spectroscopy has been widely used for structure

elucidation of copolymers, but quantitative measurements require significant amounts of sample, and sample preparation may pose a bottleneck, limiting its scope for applications in high throughput analysis and in cases, where measurements are limited by the amount of sample available. In this study, the potential of Raman spectroscopy has been exploited as a fast and non-destructive alternative for comonomer quantification requiring no sample preparation. The Raman spectra of ethylene/1-olefin copolymers, with comonomers ranging from 1-butene to 1-octadecene, show a band ensemble in the frequency region below 1000 cm^{-1} which results from the scattering from the comonomer sequences and increases in intensity with increasing comonomer content. Upon comonomer incorporation the spectra reflect the combined effect of the decrease in ethylene content, associated changes in the phase composition of polyethylene and increased scattering from the comonomer sequences. The band ensemble characteristic for the comonomer itself cannot be used for quantification since the intensity of the spectra is affected by the sample focus and the spectral acquisition time. These effects, together with the spectral changes upon comonomer incorporation, have been analyzed to identify an internal standard for normalizing the intensity of the band ensemble. The intensity of the band at 1295 cm^{-1} in the C-C twisting region was found to be appropriate for this purpose also accounting for the effect of the experimental parameters in the spectra. This method has also been extended for determining the comonomer content of a cyclic olefin copolymer (ethylene/norbornene) having low crystallinity where the bands arising due to scattering from the comonomer sequences start dominating. Hence, in this study the Raman spectra of copolymers of ethylene with 1-olefins ranging from 1-butene to 1-octadecene and the cyclic norbornene have been analyzed and a method has been developed to quantify the comonomer content. Due to the minimal sample preparation, fast spectral acquisition time and its non-destructive nature, the Raman spectroscopic approach would be very useful for quality controls. A strong need for such a technique also exists in liquid chromatography where the amounts of sample acquired are regularly very small.

6.2 Determining the percentage crosslinking in ethylene vinyl acetate photovoltaic encapsulants using Raman microscopy

The Raman spectrum of EVA in the range of the C-C stretching and the deformation vibrations of the CH_2 and CH_3 groups is shown in Figure 29, and the fundamental modes of vibration are assigned in Table 5 [75].

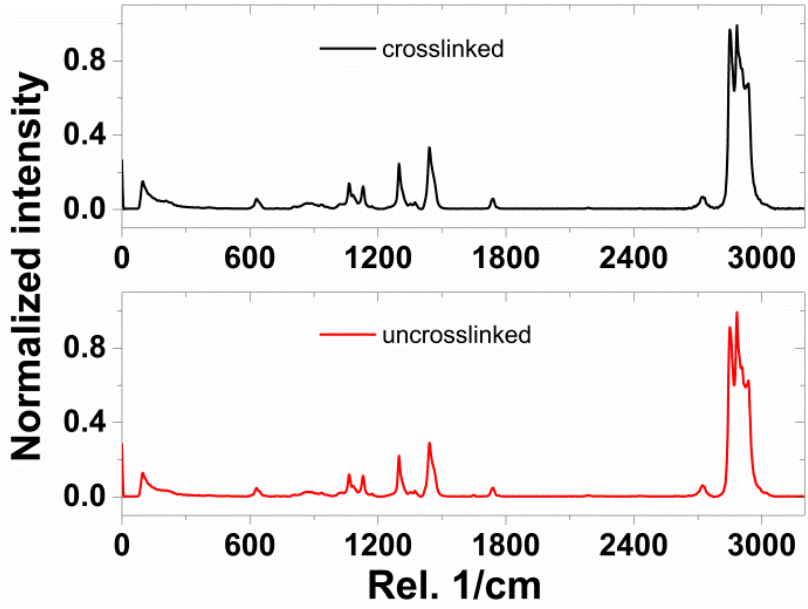

Figure 29: Raman spectrum of EVA

Table 5: Fundamental modes of vibration of the EVA spectrum

Wavenumber (cm^{-1})	Band assignment
2934, 2903, 2885, 2854 and 2725	Aliphatic C-H stretching
1740	C=O stretching of the acetate
1442 and 1300	C-H deformation
1200-1000	C-C stretching
640	C=O deformation

Upon crosslinking, pronounced changes in the form of additional bands are not observed, but significant changes in the region of the CH-stretching vibrations can be seen (Figure 30).

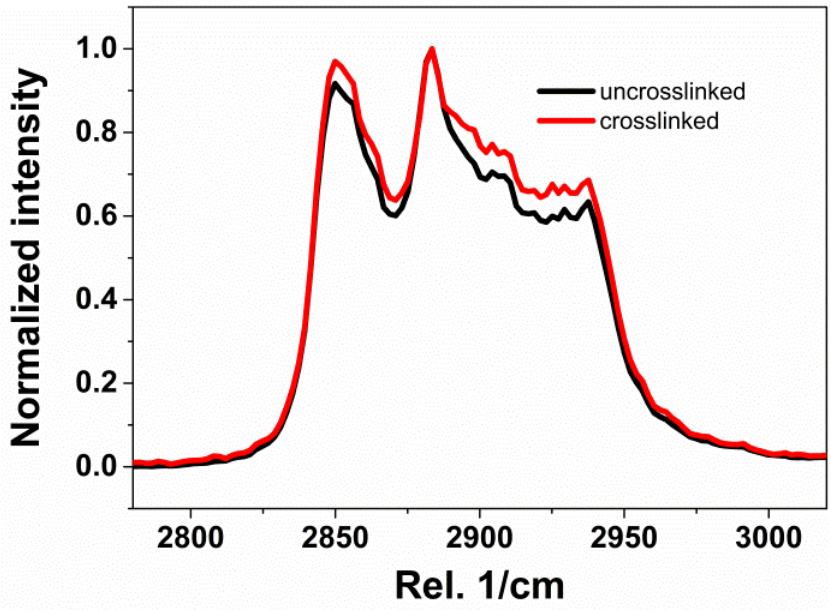

Figure 30: CH-stretching region of the Raman spectrum of EVA: spectral differences upon crosslinking

As seen from Figure 3, the intensity of the bands at 2934 and 2903 cm^{-1} is higher for the crosslinked sample compared to the non-crosslinked one. It has been previously reported that when normalizing the spectra to the highest intensity band at 2854 cm^{-1}, the relative intensity of the νCH_2 at 2934 and 2903 cm^{-1} increases upon crosslinking, while the relative intensity of νCH_3 at 2885 cm^{-1} decreases [75]. Crosslinking in EVA has been demonstrated to occur primarily via a radical reaction of the methyl group of the VA, transforming these into methylene bridges, which leads to the spectral changes as reported [75, 117].

Seven samples as detailed previously, having different lamination time, were prepared (V1-V7), and the ratio I_{2934}/I_{2885} was plotted against the lamination time (Figure 31).

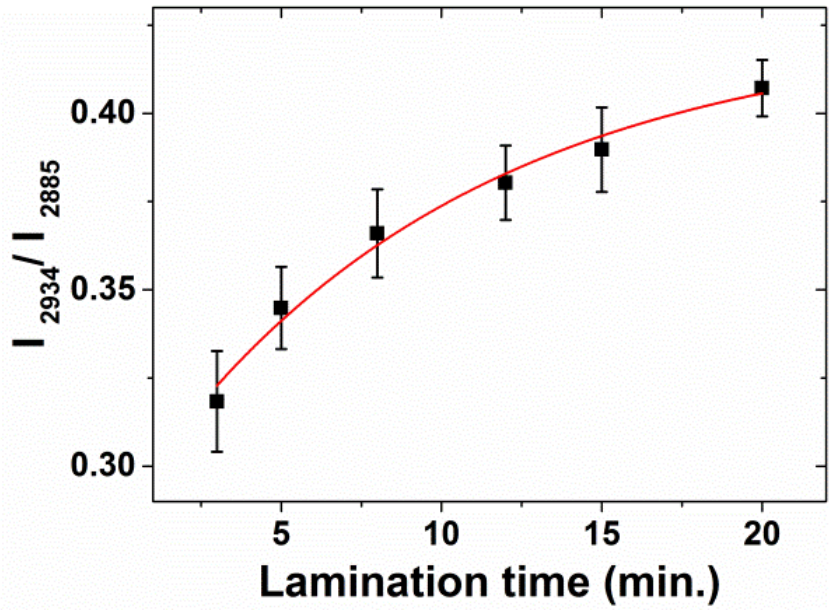

Figure 31: Variation of I_{2934}/I_{2885} with lamination time

The crosslinking starts exponentially and then converges towards a percolation value as seen in Figure 4, which is in accordance with the first order reaction mechanism proposed for the crosslinking of EVA [67].

To quantify the percentage of crosslinking using Raman spectroscopy, an interpretation of the band ratios has to be done with a method which can provide absolute values of crosslinking. This method can be used to assign band ratios to the percentage crosslinking and according to the calibration obtained, crosslinking in samples can be determined. DSC, FT-IR and Soxhlet extraction have been widely used to determine the degree of crosslinking in EVA laminates [75, 118-120]. Soxhlet extraction determines the percentage crosslinking as the ratio of the insoluble residue left in the hull to the initial mass of the sample. Figure 32 shows the percentage crosslinking as obtained from Soxhlet extraction (XC_{SE}) obtained for the sample series.

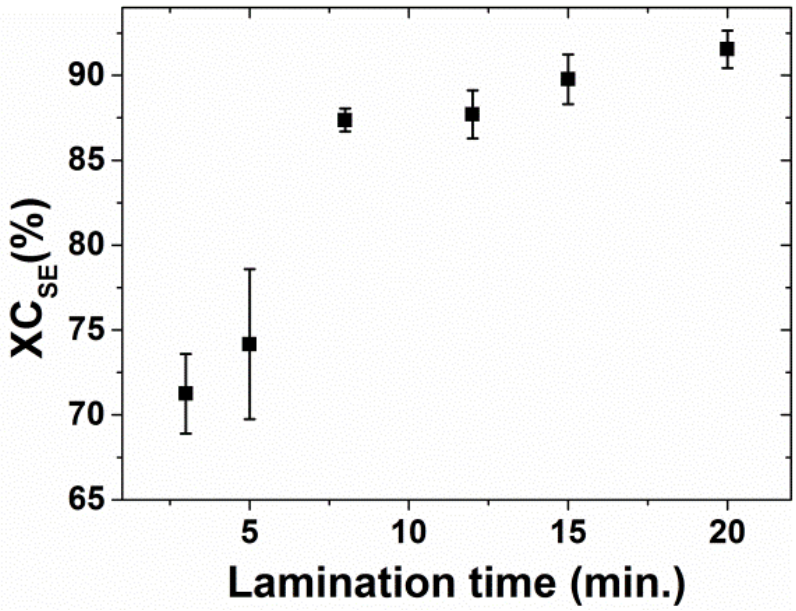

Figure 32: Percentage crosslinking determined through Soxhlet extraction (XC_{SE})

Even at low lamination times XC_{SE} is quite high, as can be recognized for the case of sample V2 which showed a crosslinking of ~73 % after just 3 minutes of lamination. Chernev et al.[75] reported a similar effect, wherein Soxhlet extraction yields high XC_{SE} values even at low lamination times.

The percentage crosslinking can also be derived from DSC measurements (XC_{DSC}). The DSC trace of the first heating cycle of EVA is shown in Figure 33.

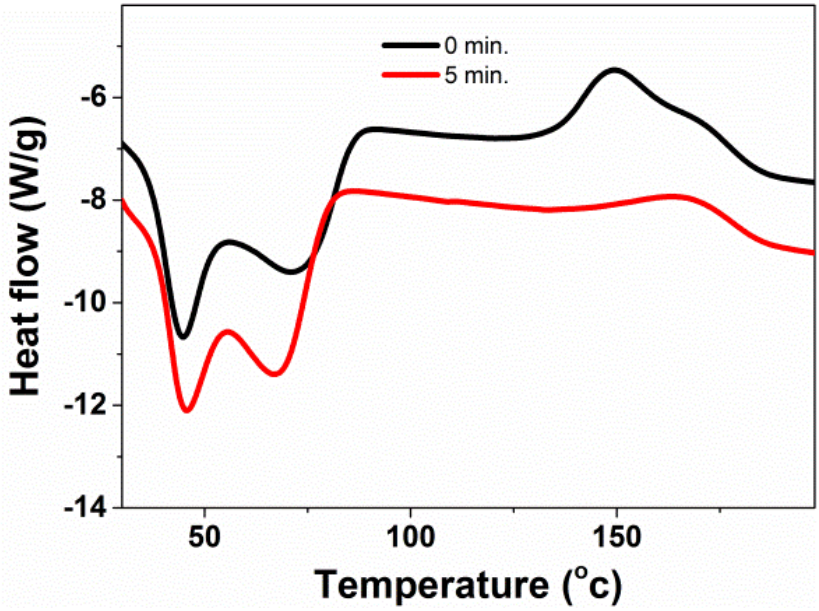

Figure 33: DSC curve showing the consumption of the crosslinker with reaction progress, seen with the decrease in the area of the exothermic peak between 40-100 °C

An endothermic double peak showing the melting of the EVA resin can be recognized between 40 - 100 °C and an exothermic event resulting from the consumption of the crosslinker can be seen between 120 - 190 °C The latter was used to calculate the percentage of crosslinking according to equation 12 by taking the enthalpy of the non-crosslinked sample (ΔHo) as a reference according to [70-74], where ΔHs represents the enthalpy of the samples V2-V7 with a higher lamination time.

$$XC_{DSC} = \frac{\Delta Ho - \Delta Hs}{\Delta Ho} \qquad 13$$

XC_{DSC} as a function of the lamination time is shown in Figure 34.

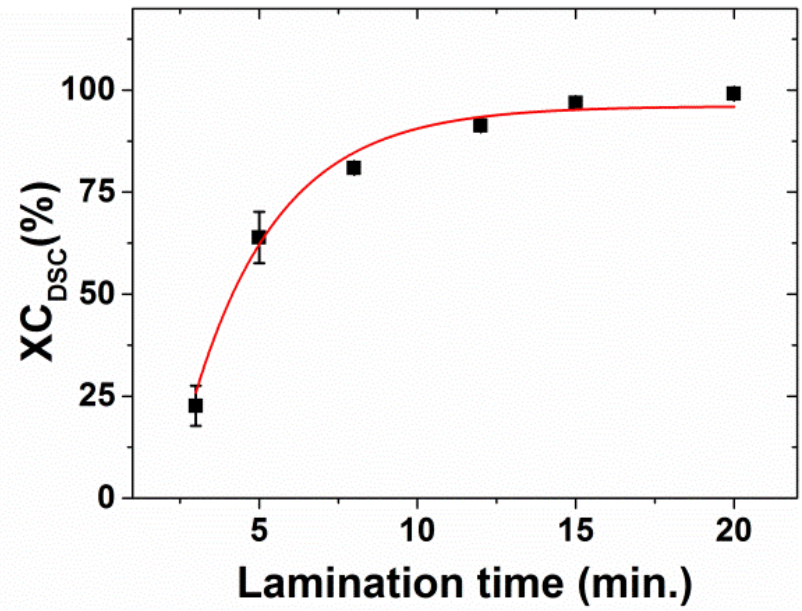

Figure 34: XC_{DSC} with the standard deviation calculated from three independent measurements of the EVA laminates.

The values obtained from the DSC also show a clear first order trend.

Infrared (IR)- spectroscopy has also been used previously to determine the percentage crosslinking in EVA laminates [75]. IR measurements were carried out on the laminates to determine the crosslinking content. Yet, the samples were too thick to be analyzed in transmission and hence were measured in Attenuated Total Reflectance (ATR) mode. The spectra are shown in Figure 35.

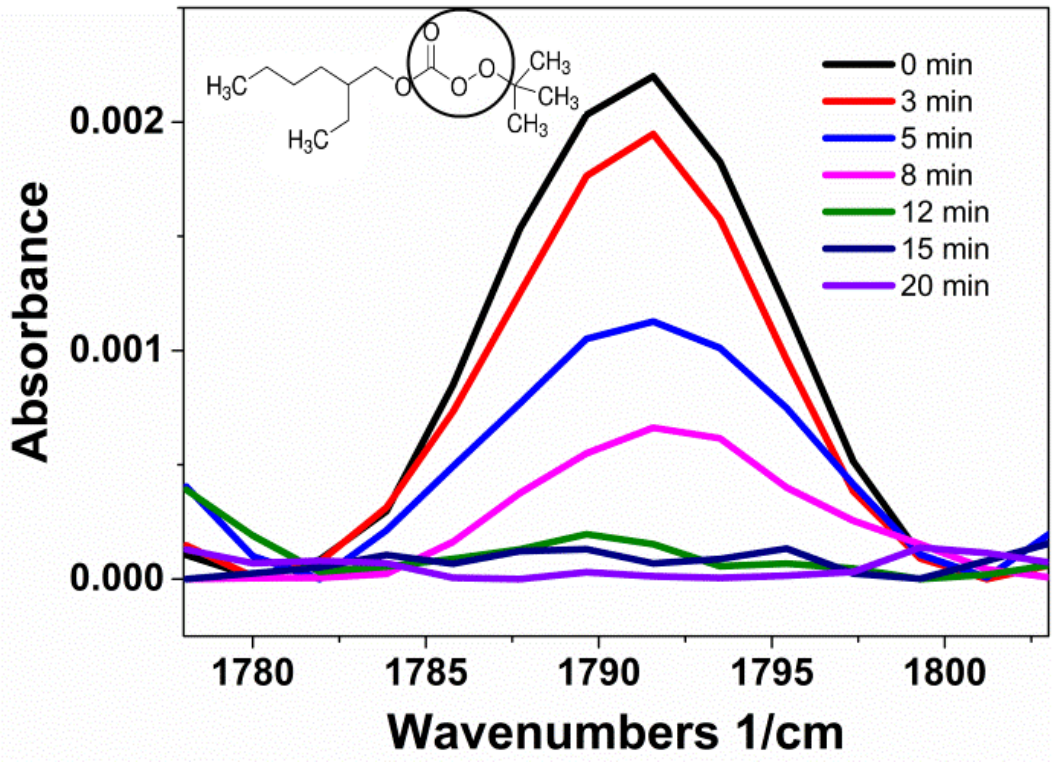

Figure 35: Intensity of the band at 1791 cm^{-1} in ATR measurements, attributed to the crosslinker.

An absorption at 1791 cm^{-1} can be recognized in the spectra, which gradually loses intensity at higher lamination time and finally vanishes at a lamination time > 8 minutes. This band can be attributed to the peroxy carbonate C=O stretching vibration [121] of the crosslinker (Figure 35). The amount of crosslinker is considered to be remaining in trace amounts and is not detectable beyond this stage, owing to the rapid consumption in the first order kinetics. Additionally, the ATR spectra have been shown to be affected by experimental parameters such as the applied pressure, the surface area being measured and the change in the refractive index with the penetration depth of the sample [76]. The non-detection of the crosslinker by FT-IR measurements owing to its rapid consumption and the limitations of the ATR method with regard to quantification as detailed previously made it unsuitable for drawing out any correlation between the percentage crosslinking and the reaction progress. Hence, the feasibility of studying the crosslinking behavior was compared between the values obtained for XC_{DSC} and XC_{SE} shown in Figure 36.

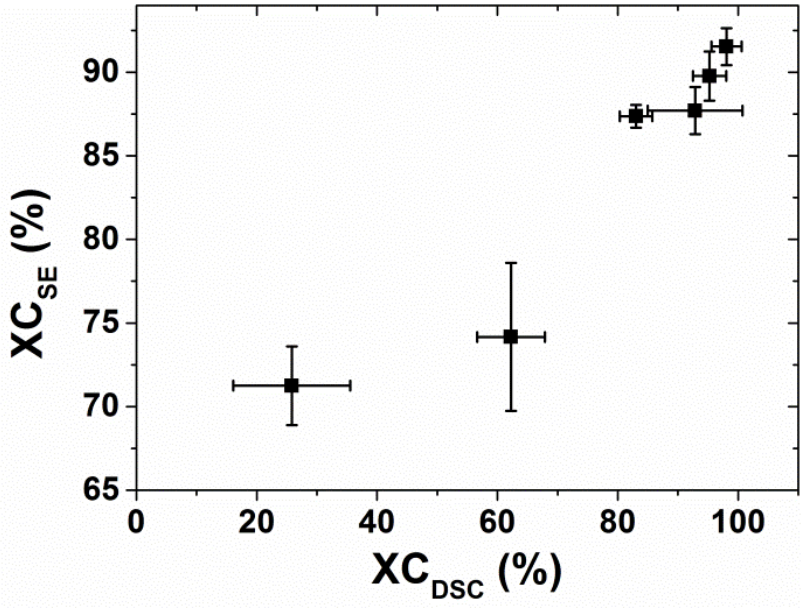

Figure 36: Comparison of XC_{DSC} compared to XC_{SE}

From Figure 36 it can be inferred that for lower lamination time the Soxhlet method overpredicts the value of crosslinking, while the DSC approach underpredicts the crosslinking at higher lamination times. This can be explained as the Soxhlet method measures the fraction of non-extractable polymer chains and even very few bonds formed during crosslinking may render a chain as non-extractable. The gel content does not discriminate between single and multiple crosslinked chains [117] and as a consequence, a high value of gel content is observed even at low lamination times.

The underprediction in DSC can be explained by insufficient sensitivity of the thermocouple for the exothermic event at minute concentrations of crosslinker. On a broader perspective, techniques such as DSC and FT-IR spectroscopy which rely on determining the percentage crosslinking through the amount of residual crosslinker are limited by their lacking sensitivity to the low amount of the crosslinker present in samples with higher lamination time. Hence, XC for sample V7 as obtained through Soxhlet extraction was used to translate the band ratios obtained from Raman measurements into absolute values of crosslinking.

A linear translation from the band ratio νCH_3 / νCH_2 into the percentage crosslinking can be postulated as

$$XC_R = M^*(I_{2934}/I_{2885}) + C \quad (14)$$

Where 'XC_R' denotes the percentage crosslinking obtained from Raman measurements, M denotes the slope of the straight line translation with C being the intercept. To determine the values of the unknown parameters M and C two boundary conditions are needed. These were selected as firstly being the band ratio 2934 cm^{-1}/2885 cm^{-1} of an non-crosslinked sample, V_0, determined to be 0.306. The second point of consideration was taken as XC_{SE} for the sample V7, determined to be 91.5 % and having a band ratio 2934 cm^{-1}/2885 cm^{-1} of 0.407. Using these two end points, Eq. 14 was solved for the unknown parameters M and C as shown below.

Point 1: $0 = M^*0.306 + C$
Point 2: $91.5 = M^*0.407 + C$

By solving these equations the correlation obtained between XC_R and the band ratio is

$$XC_R = 906.2I_{BR} - 277.3 \quad (15)$$

Using this correlation between XC_R and I_{BR}, the band ratios in Figure 31 were translated into percentage crosslinking and plotted against the lamination time (Figure 37).

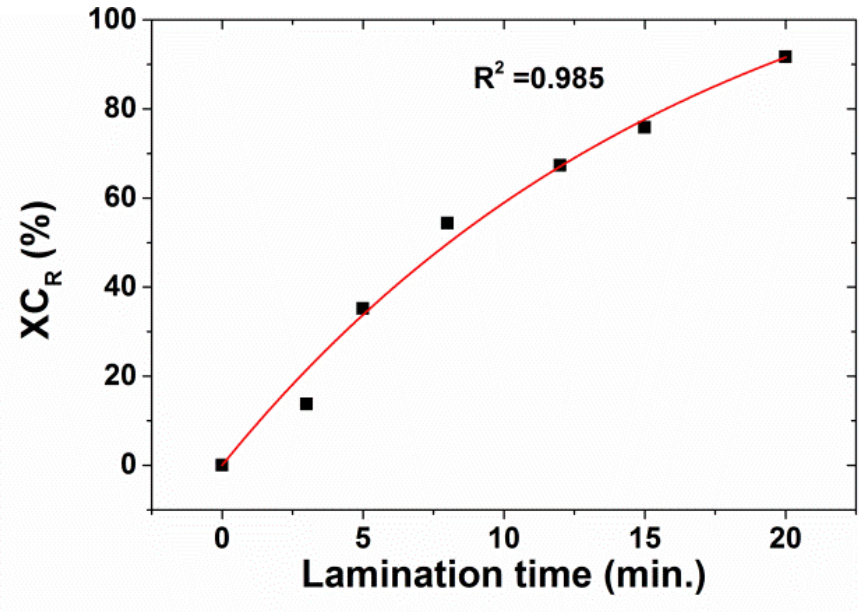

Figure 37: Raman degree of crosslinking determined using equation (15)

As seen from Figure 37, a good correlation to the first order fitting of the crosslinking reaction mechanism of EVA proposed by Schröder et. al [67] can be observed. This further suggests that the method developed to translate the band ratios into absolute crosslinking numbers based on the percentage crosslinking obtained through Soxhlet extraction can be accurately applied to determine the percentage of crosslinking in a quantitative manner when an EVA resin with similar VA content was crosslinked under identical conditions.

A crucial question when developing structure↔property relationships for films is how the degree of crosslinking is spatially distributed i.e., identifying inhomogeneities. To provoke these, sample V8 was crosslinked by using a lower amount of both the crosslinker and the crosslinking promoter. Raman microscopy was carried out over a selected area and the spectra collected over the entire region were analyzed. The intensity of the CH_3 stretching region was calculated and plotted for each spectrum obtained to identify the presence of such inhomogeneities (Figure 38).

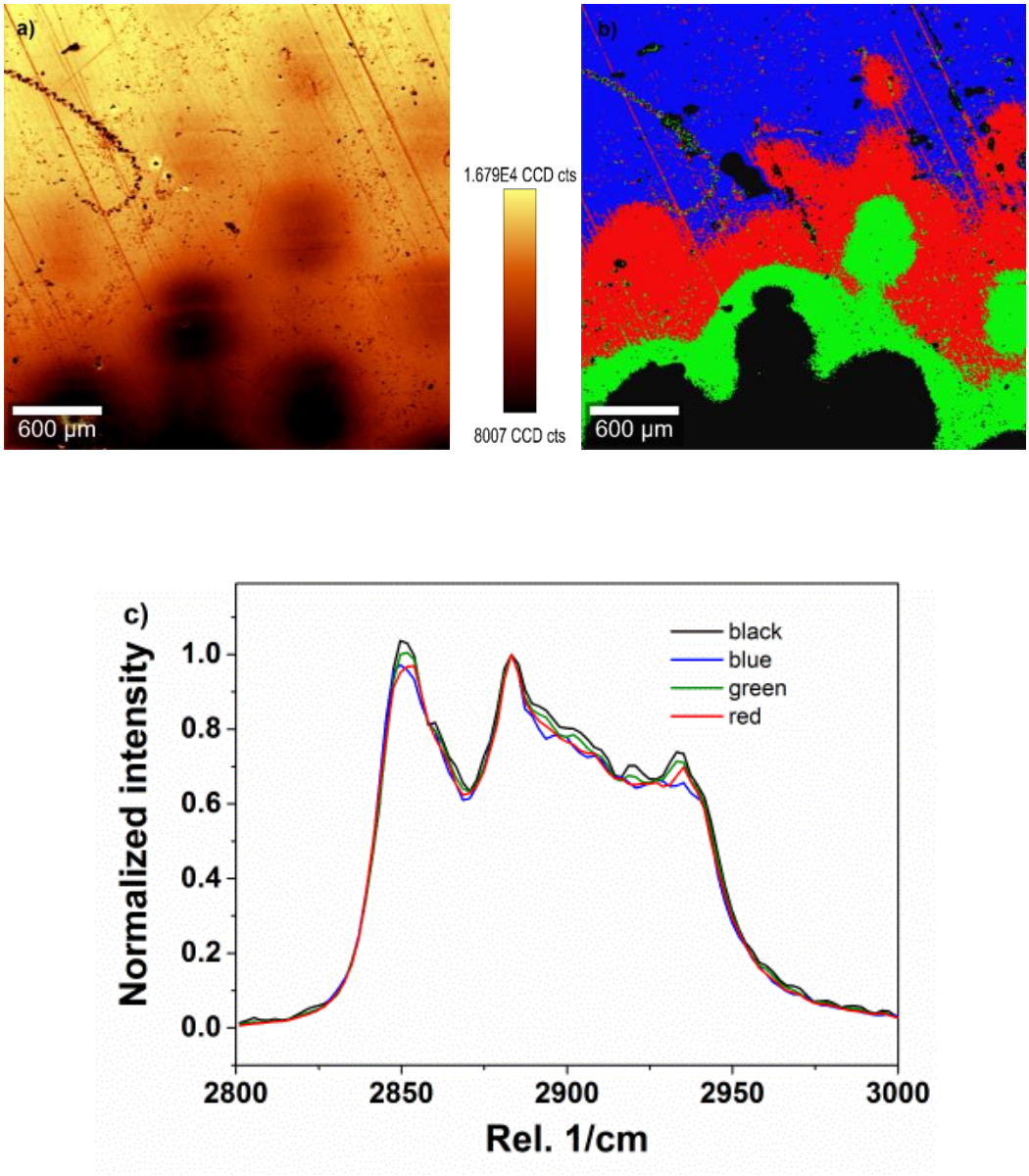

Figure 38: a) Intensity map of the CH_3 stretching region from 2800-3000 cm^{-1} b) Segregation of Raman spectra obtained based on spectral differences c) Raman spectra representative for the average in the individual clusters

The intensity map of the CH_3 stretching region in Figure 38a shows a clear variation in intensity, which suggests possible fluctuations in crosslinking over the area. Four distinct clusters were obtained by spectral segregation (Figure 38b) showing differences in the intensity of the bands in the CH_3 stretching region (Figure 38c). From the spectra it can be observed that the νCH_2 band at 2934 cm^{-1} and the νCH_3 band at 2885 cm^{-1} show a large variation in intensity within the clusters obtained.

These spectral differences were analyzed and the average band ratio I_{2934}/I_{2885} was calculated for each of the four clusters. Using the calibration model developed earlier these band ratios were then translated into values of XC_R. The blue region was seen to be non-crosslinked as the band at 2934 cm^{-1} was very low in intensity compared to the other regions. The other three regions, namely the red, green and the black area show an average degree of crosslinking of 27, 54.5 and 94.2 % respectively. An explanation for this would be an inhomogenous distribution of the crosslinker, augmented by the effect of an insufficient amount of crosslinking promoter, which ultimately lead to inhomogeneity in crosslinking across the sample.

The same sample was also investigated with regard to locally more confined inhomogeneities in the order of a few μm. An area 100 x 100 μm^2 was analyzed and spectra were collected every 0.5 μm. The data generated were segregated and clustered as described above. The intensity map of the CH_3 stretching region in this area is shown in Figure 39a.

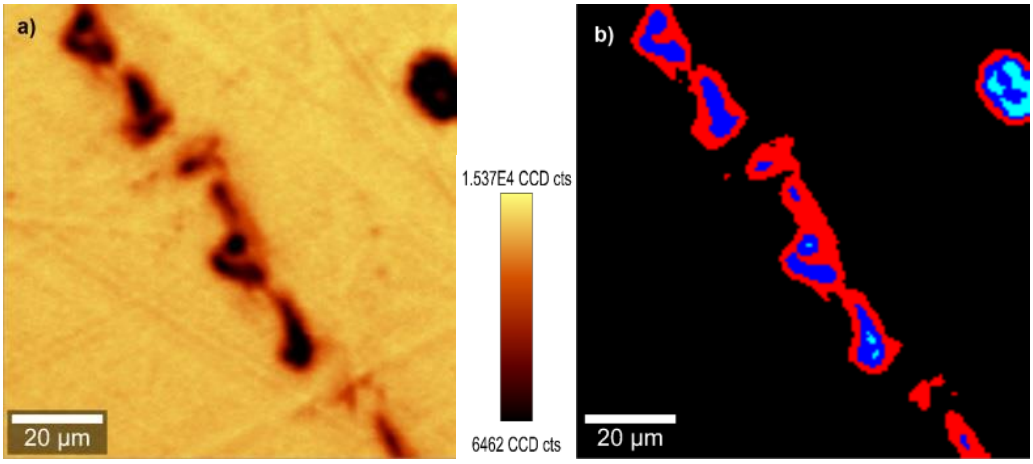

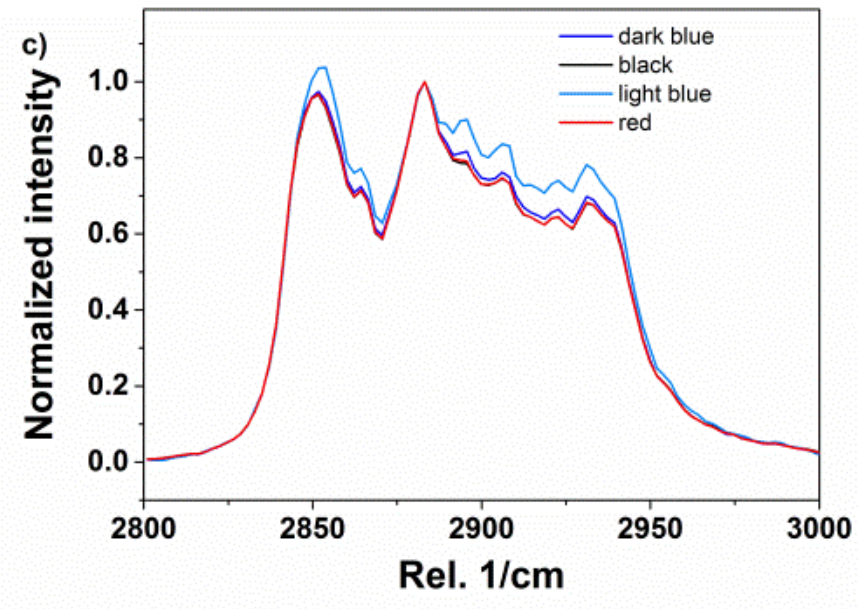

Figure 39: a) Intensity map of the CH_3 stretching region from 2800-3000 cm^{-1} b) Segregation of Raman spectra obtained based on spectral differences c) Raman spectra representative for the average in the individual clusters

The CH_3 stretching region shows a variation in intensity in the form of small inclusions/spots as seen in Figure 39a. The spectral dataset showing the clusters based on spectral differences is shown in Figure 39b and the average spectrum obtained for each of these clusters is shown in Figure 39c. Again, clear differences in crosslinking are observable with the intensity of the νCH_2 band at 2934 cm^{-1} and the νCH_3 band at 2885 cm^{-1}. The νCH_2 band shows an increase in intensity in the innermost region of the inclusion compared to the region where the spots are not present. The band ratio I_{2934}/I_{2885} was calculated and translated into percentage crosslinking based on the model proposed previously. The black, red, dark blue and light blue regions were found to have an average crosslinking of 16.2 %, 17.1 %, 30.6 % and 106.9 %. A tiny region shown in light blue can be recognized, which was highly crosslinked compared to the surrounding polymer. The occurrence of such pronounced inhomogeneities can be explained as the result of a local maximum in crosslinker concentration, causing this area to crosslink intensely.

After developing a method to study inhomogeneities in crosslinking on different length scales using model systems prepared between Teflon sheets, it is essential to transfer this model to glass-laminates. This was probed using sample V9. A major advantage of Raman microscopy is the fact that measurements can be carried out without destroying the glass laminates by measuring through the glass. Transparent silicate materials like glass do not generate intense Raman signatures, hence the Raman scattering is unfazed by the presence of a glass layer on the measuring surface [122-124]. The spectral dataset obtained upon mapping of V9 was analyzed as previously, and the intensity of the CH_3 stretching region was plotted to determine local inhomogeneities in crosslinking across the sample (Figure 40).

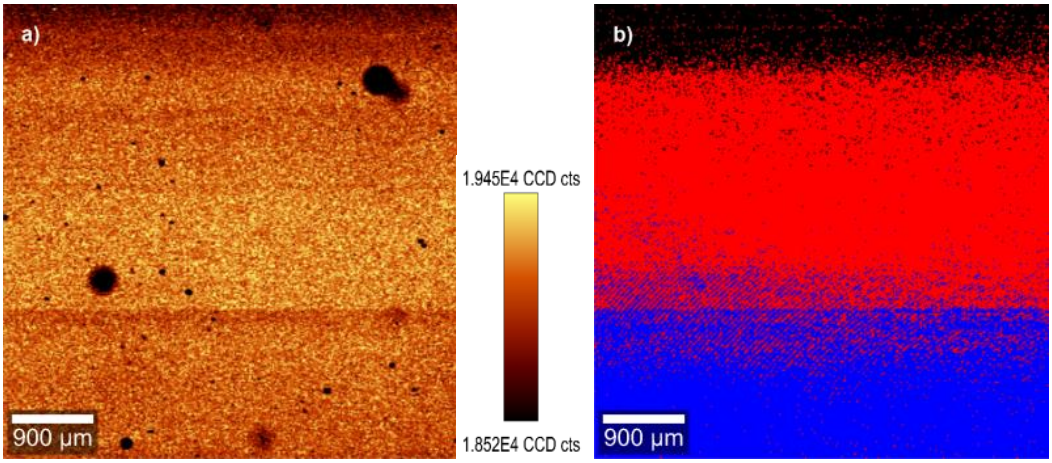

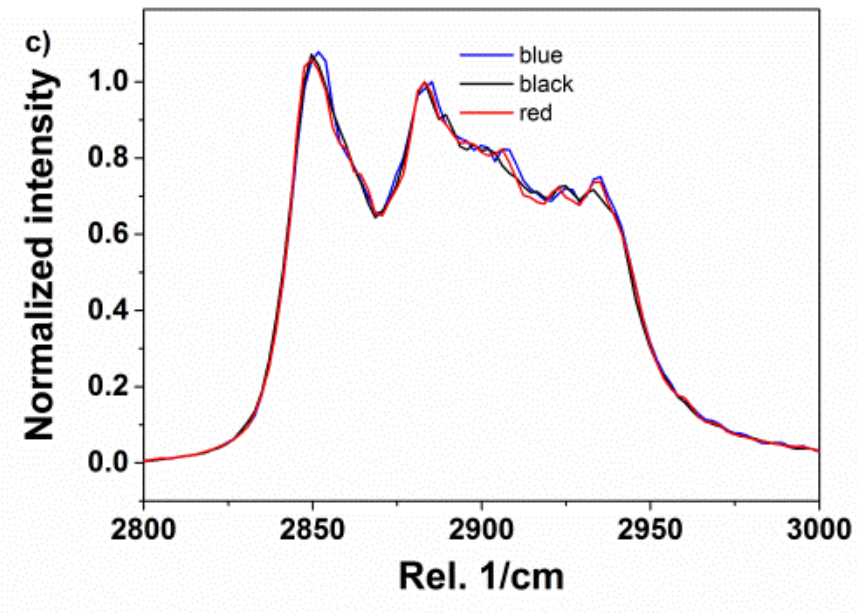

Figure 40: a) Intensity map of the CH_3 stretching region from 2800-3000 cm^{-1} b) Segregation of Raman spectra obtained based on spectral differences c) Raman spectra representative for the average in the individual clusters

The intensity of the CH_3 stretching region is inhomogeneously distributed suggesting differences with regard to crosslinking across the sample. The spectral dataset was then clustered (Figure 40c) and three distinct regions could be distinguished based on differences in the spectra as shown in Figure 40b. The clustered regions seen in this case showed three distinct layers, whereas the distribution seen previously for sample V8 was more irregular. The XC_R in the above three distinct black, red and blue clusters

was calculated and found to be 121.8 %, 248 % and 235.2 %, respectively. This implies that the major difference in crosslinking is present along the top edge of the sample, whereas the other two regions show almost similar values of XC_R. Such broad inhomogeneities can be well explained by differences in the cooling/heating patterns of the glass laminate being predominant at the sample edge.

Surprisingly, the values of crosslinking are considerably higher than those of sample V7. These differences were assessed by analyzing the spectra of a highly crosslinked region measured under the glass laminate. An overlay of the spectra of sample V7 and the spectrum of a non-crosslinked material with the sample crosslinked under glass is shown in Figure 41.

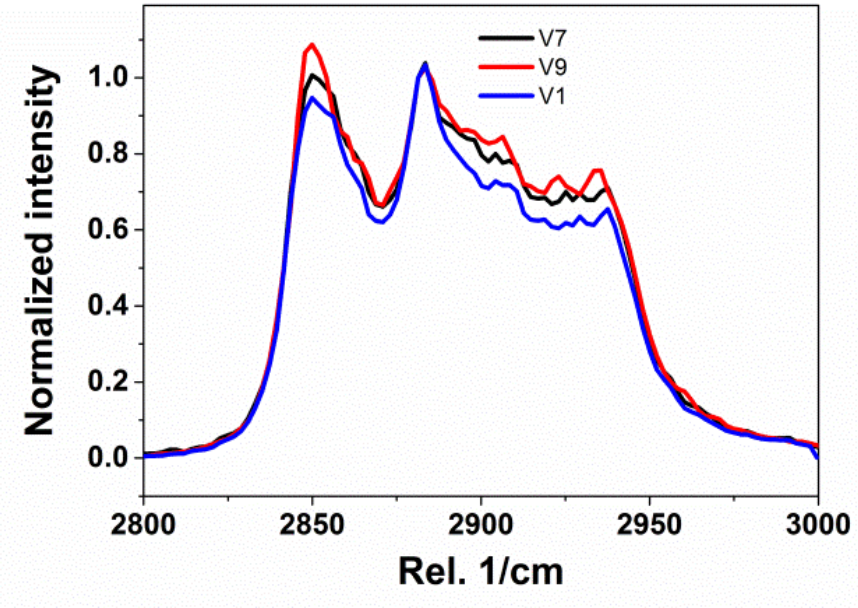

Figure 41: Comparison of crosslinking under glass to EVA sheets laminated under Teflon showing the variation in intensity of the bands at 2934 and 2903 cm^{-1}

Figure 41 clearly confirms a higher intensity for the bands at 2934 and 2903 cm^{-1} in the glass laminate compared to samples V7 and V1. The increase in the intensity of these bands reveals the consumption of more CH_3 units in the glass laminate, suggesting the formation of CH_2 bridges for multiple crosslinking. This can be due to

the fact that the crosslinking of sample V7 was carried out under Teflon sheets, which leads to differences compared to the process carried out under glass: In the first case the crosslinking process is inhibited by a sudden quenching of the samples as the sheets are removed. However, crosslinking under glass involves annealing of the laminates as the samples are removed from the oven, wherein multiple crosslinks are still forming in the material as it slowly cools down, insulated due to the low thermal conductivity (~0.9 W/m K) [125] of the glass covering. The glass covering also does not allow the trapped thermal energy to be dissipated easily being opaque to IR radiation [126]. Convective heat transfer is also much lower compared to the samples produced between Teflon sheets which can freely lose thermal energy to the surrounding air once the sheets are removed. This explains the higher amount of crosslinking as observed in the glass laminate.

6.2.1 Conclusions

Assessing the degree of crosslinking, XC, of ethylene vinyl acetate resin in photovoltaic modules remains a challenge, which has a great impact on the cell efficiency. Various techniques such as DSC, FT-IR and Soxhlet extraction have been used for this purpose. All these approaches lack spatial resolution per se, as they are limited to bulk differences in XC, whereas local inhomogeneities are averaged out. In the present study a method based on Raman microscopy has been developed to study local variations in crosslinking in PV modules and quantify these. The signal intensity of the respective bands in the spectra reflects the transformation of methyl groups into methylene bridges as a consequence of crosslinking, and thus the conversion. Yet, this information is of relative nature, and to translate it into absolute values, a calibration of the Raman bands was carried out using a non-crosslinked sample and the results from Soxhlet extraction for a highly crosslinked sample as reference. The method developed has then been applied to characterize inhomogeneities with regard to crosslinking in EVA films prepared between Teflon sheets on various length scales, ranging down to a few μm. As Raman microscopy is indifferent to measuring under glass, the developed method was then applied to study crosslinking inhomogeneities

in EVA/glass laminates. In this case the quantification of crosslinking yielded significantly higher values for XC_R compared to the model films prepared between Teflon sheets. Raman microscopy being the only technique sensitive to measuring multiple crosslinks in the samples delivers a higher XC value for this system compared to the system without the glass. This observation has been attributed to differences in the cooling pattern of the glass system, causing the formation of multiple crosslinks. This is a very important conclusion, as it clearly demonstrates the limitations for transferring results from a model system to the real process.

6.3 Investigating the morphological variations due to processing and thermo-mechanical treatment of polypropylene using Raman microscopy

Figure 42 shows the PLM image of an injection molded plate of non-nucleated PP-H. A 10 μm thick section was microtomed off and imaged to determine the presence of polymorphs of PP.

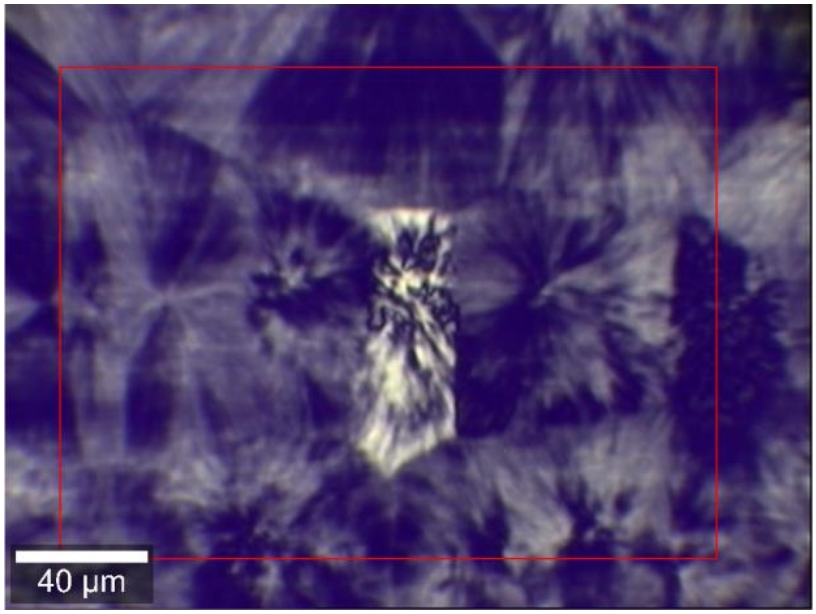

Figure 42: PLM image showing a β-spherulite surrounded by α-spherulites

The bright structure in the center corresponds to a β-spherulite showing a high and negative birefringence compared to the α-spherulites, which appear as the darker

structures surrounding the β-spherulite. Figure 43 shows a typical Raman spectrum of an α- and β-spherulite.

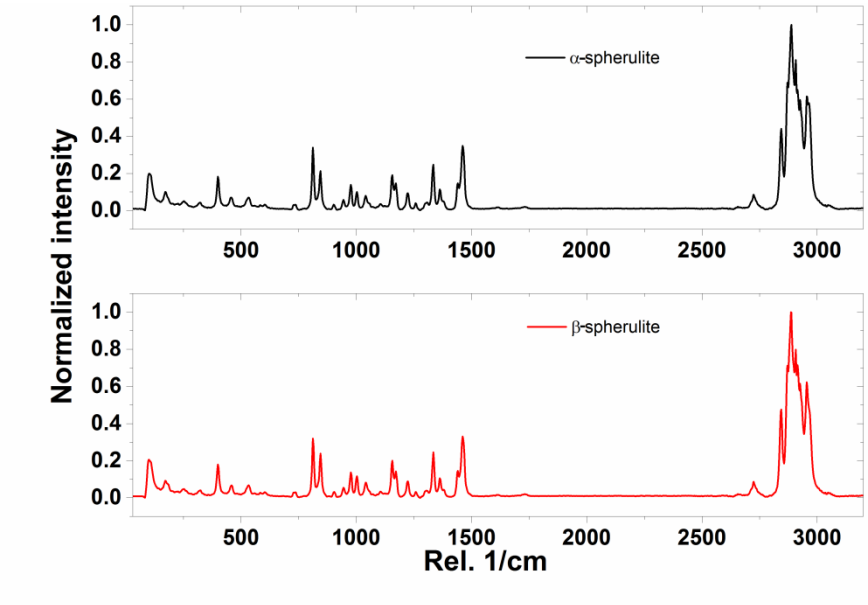

Figure 43: Raman spectra of α-and β-spherulites

The Raman spectra of α- and β-spherulites as shown in Figure 43 do not show any major differences and distinct bands, which can be assigned to a particular polymorph, cannot be observed. Hence, a qualitative identification of the spherulitic structure and the morphology based on band identification is not possible. However, a band shift to higher wavenumbers has been reported [103] for β-spherulites. Figure 44 shows the bands at 809 and 841 cm^{-1} for a β-spherulite and the surrounding network of α-spherulites.

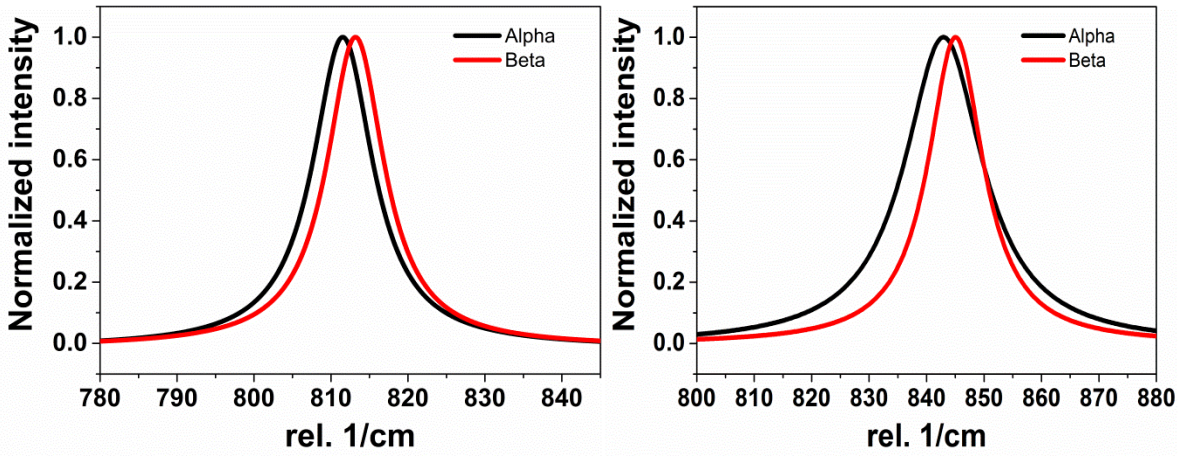

Figure 44: Raman spectra of both polymorphs at 809 and 841 cm^{-1}

The shift in the band position was calculated over the whole profile of a β-spherulite, surrounded by α-spherulites, and a contour plot was generated showing the position of the two bands at 809 and 841 cm^{-1}.

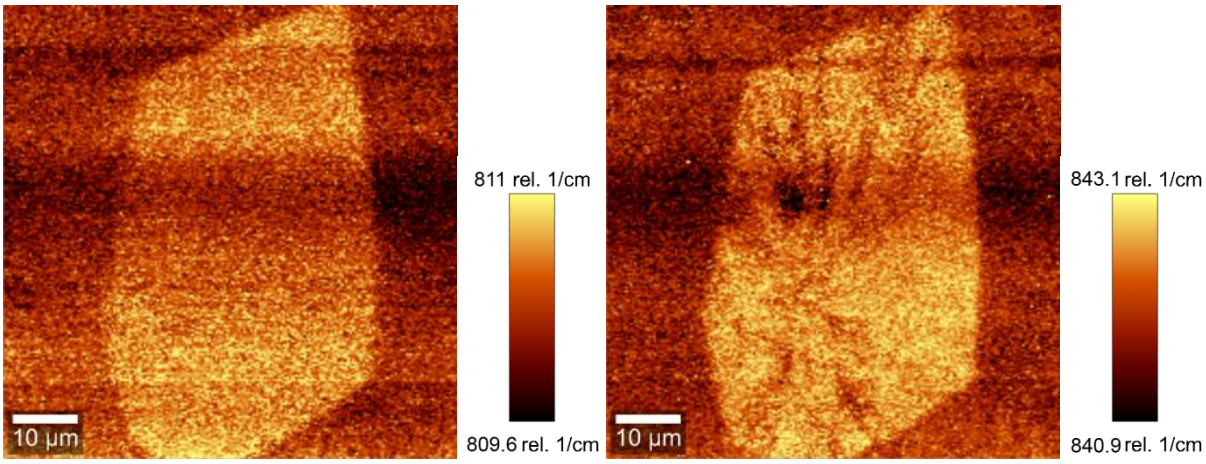

Figure 45: Contour plots showing the band position at a) 809 and b) 841 cm^{-1}

The complete structure of the β-spherulite can be easily distinguished from the surrounding α- polymorph as seen from the contour plots in Figure 4. The band at 809 cm^{-1} showed a maximum shift of 1.4 cm^{-1}, whereas the value was 2.2 cm^{-1} for the band at 841 cm^{-1}, which makes the latter more suitable to identify and profile the entire β-spherulite. Interestingly, no method has been reported so far to

unambiguously identify the presence and profile α-spherulitic structures with Raman spectroscopy. Herein, it was found that the band at 2843 cm^{-1} in the Raman spectrum of α-spherulites showed a positive shift of 2 cm^{-1} compared to the spectrum of β-spherulites and can be used to identify and profile the distribution of α-spherulites as shown in Figure 46.

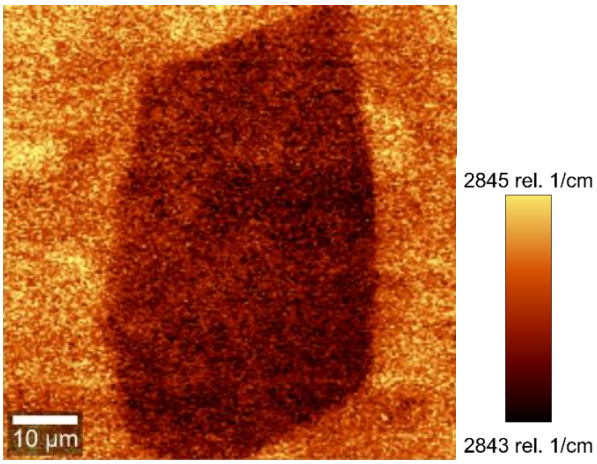

Figure 46: Contour plot showing the band position at 2843 cm^{-1}

As seen from the contour plot the shift in the band position at 2843 cm^{-1} is suitable for identifying and profiling α-spherulites, and a distinct profile of the surrounding α-spherulitic region could be generated. Hence it can be deduced that shifts in the Raman bands at 841 and 2843 cm^{-1} are suitable to profile the distribution of β- and α-spherulites, respectively.

As discussed previously, profiling X_c across the whole spherulite remains a challenge which has been previously carried out by etching and removing the amorphous regions in the sample [105]. The method proposed by Nielsen et al. [104] for determining the X_c of PP from the Raman spectra as discussed previously was applied. A Lorentzian fitting was carried out to calculate the band intensity as shown in Figure 47 and X_c was calculated using equation 1.

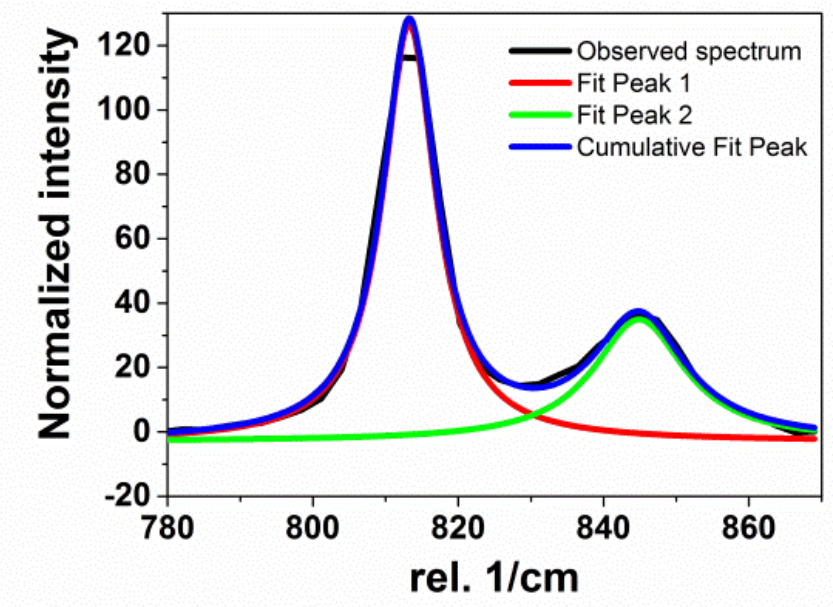

Figure 47: Band fitting of the Raman spectra of PP in the range 780-870 cm^{-1}

The Raman spectrum shown herein does not display any significant band at 830 cm^{-1}, suggesting that the fraction of chains in the non-helical conformation (defect phase) is negligible.

The Raman spectra were acquired over the region shown in Figure 48a, and each spectrum was fitted to obtain the intensity of the bands at 809 and 841 cm^{-1}. The spectral intensity acquired for each point was then used to calculate the crystallinity and a contour plot was generated as shown in Figure 48b.

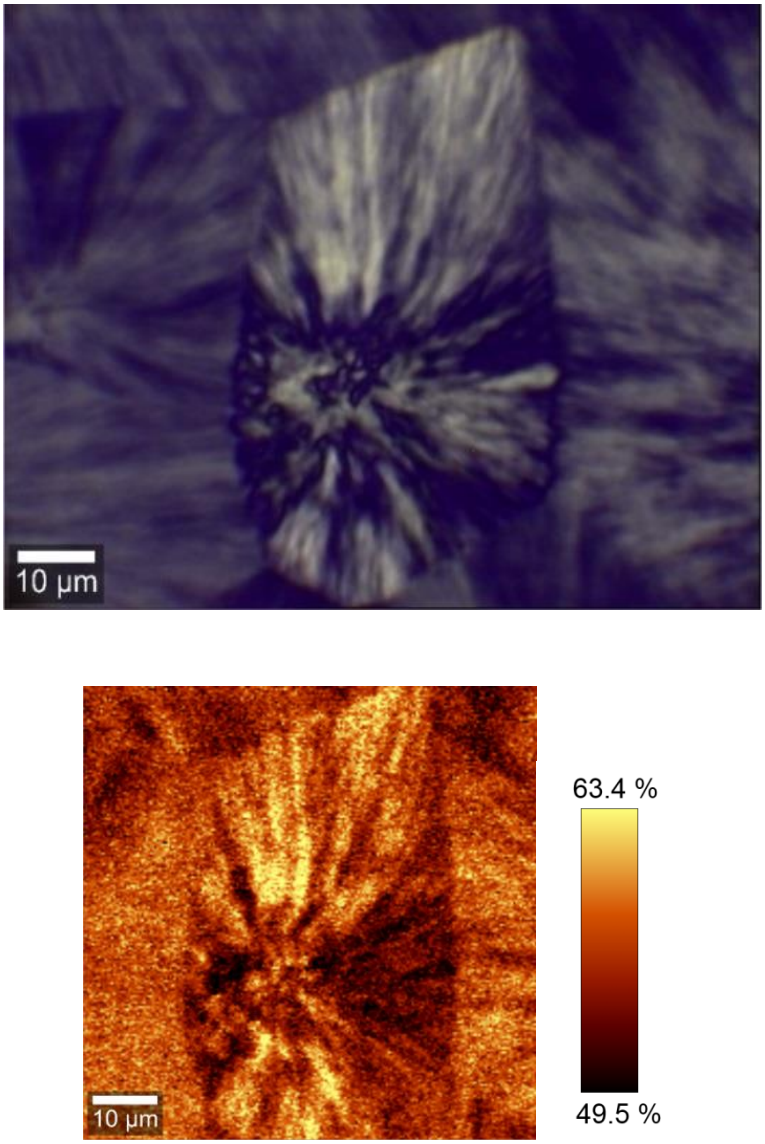

Figure 48: a) PLM image of a β-spherulite surrounded by α-spherulites b) Contour plot showing the distribution of X_c over the β-spherulite

The contour plot reflects the complete profile of the β-spherulite, surrounded by the α-variety and the distribution of X_c.

A similar mapping was carried out to study the distribution of X_c over a whole α-spherulite. Figure 49a shows an α-spherulite for which the Raman spectra were acquired and fitted to generate the profile of X_c in Figure 49b.

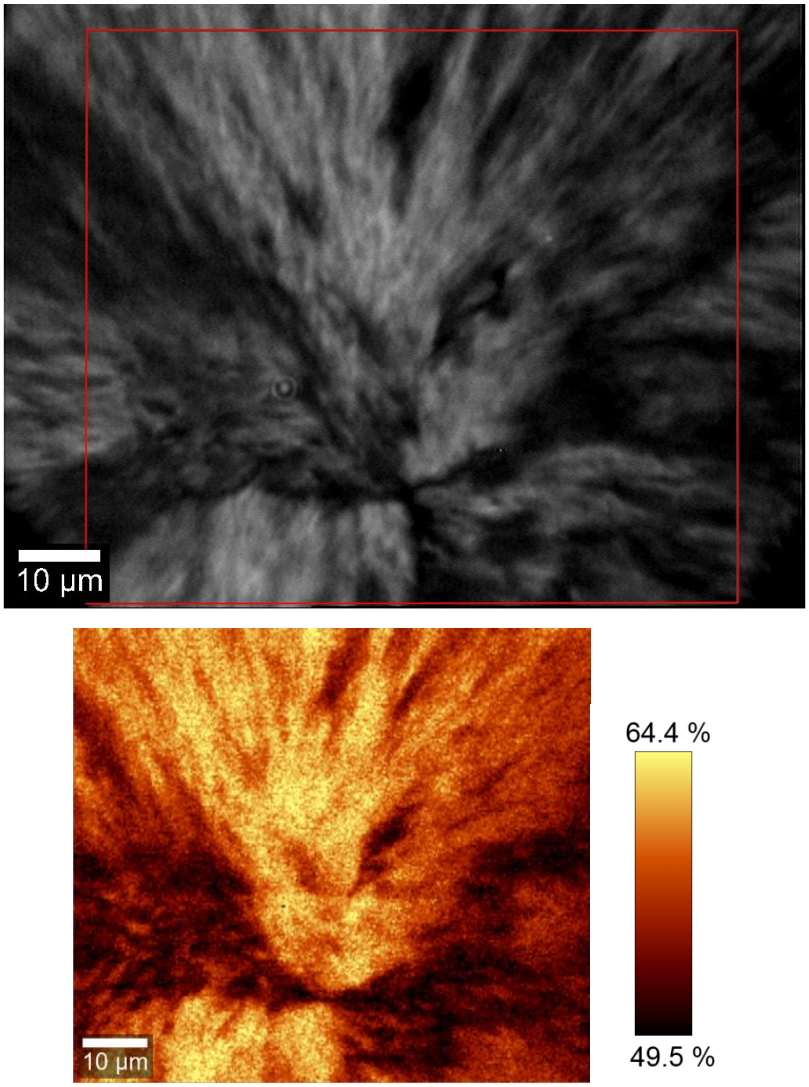

Figure 49: a) PLM image of an α-spherulite b) Contour plot showing the X_c across the α-spherulite

As can be seen, it is thus possible to study X_c over the entire spherulite using Raman microscopy and map the amorphous and crystalline domains. The radial morphology of the spherulite is evident in both cases and a condensed highly crystalline structure can be identified in the center of both the polymorphs [109, 127]. The fine variations in X_c with the amorphous regions present in small domains around the highly crystalline regions can easily be distinguished.

Surprisingly, it was observed that the band at 2954 cm^{-1} showed a shift in both the α- and β-polymorph as plotted in Figure 50.

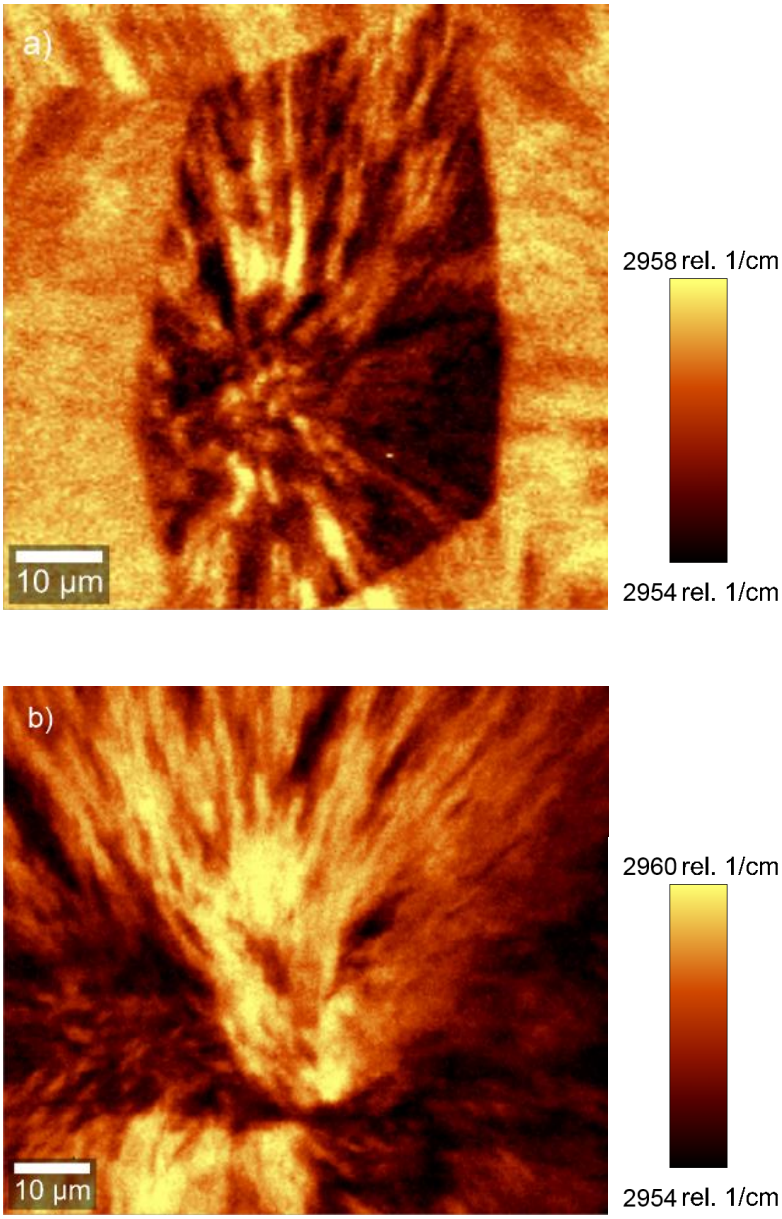

Figure 50: Contour plots showing the band position at 2954 cm^{-1} in the a) β-spherulite and b) α-spherulite

The contour plots of the band position show the crystalline domains in the samples. The domains observed in this case were more clearly visible compared to the X_c profiles determined previously and this method for probing the crystalline domains is applicable to both the α- and β-polymorph as shown. Herein, even the fine fibrilar spherulitic structure could be seen clearly in the contour plot. Hence, this band can be used to determine the distribution of the crystalline domains for both polymorphs of

PP. The band shift observed for the α-polymorph in this case was seen to be 2 cm^{-1} larger than the shift observed for the β-polymorph.

A need to study morphology and composition on very low length scales exists in welding, where a complex interplay between the local heating and cooling patterns as well as the mechanical forces due to shearing, leads to a new morphology. Thus, an in depth characterization of welds with regard to morphology and composition is an important step, and the data gained in this way may be used to improve the process of welding as well as for failure analysis, as welds are the region most susceptible to failure under load. For investigating these variations in welded materials, model welds were prepared by joining two plates of PP-H via butt welding and were investigated using DSC, FT-IR microscopy and Raman microscopy. Figure 51 shows the PLM image of the welding channel between two PP-H plates.

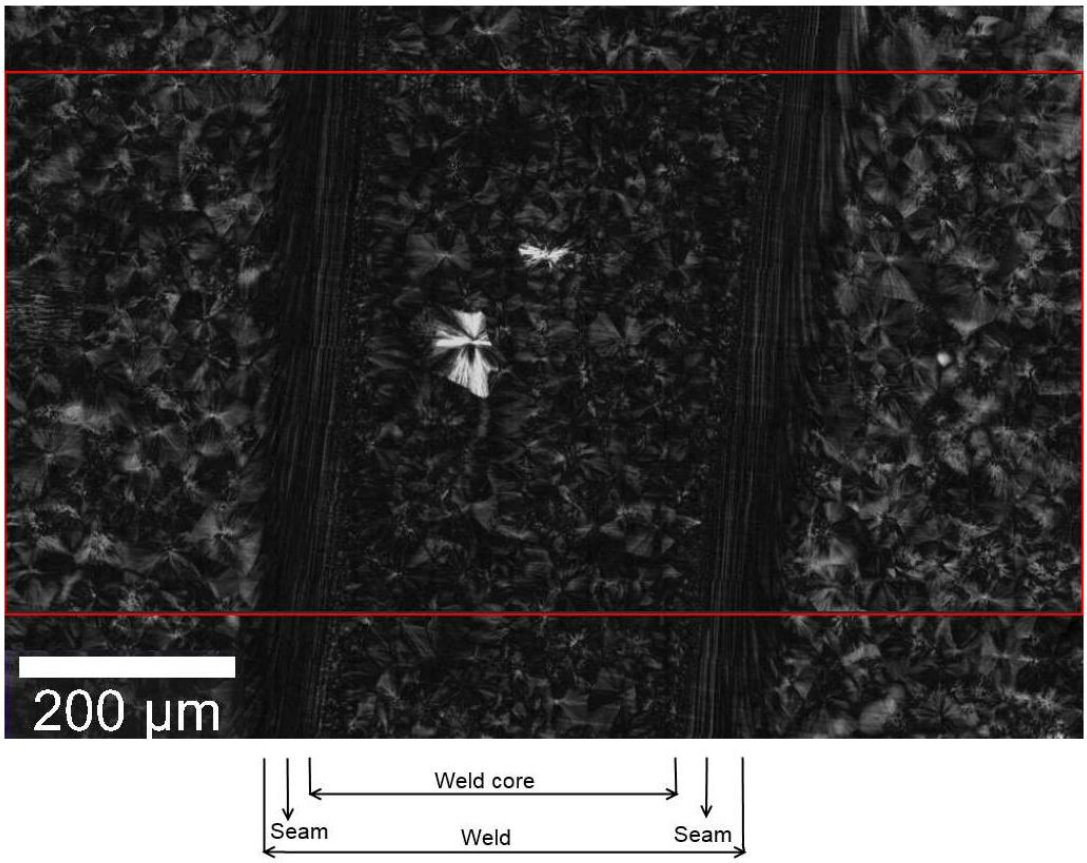

Figure 51: PLM image of the weld with assignment of the distinct regions

The region of the weld seams shows the presence of elongated spherulites formed due to the high shear rates experienced along the weld seams, which are in agreement with the observations made by Tüchert et al. [112]. Additionally, β-spherulites can be identified in the weld core, appearing with high brightness and showing negative birefringence, whereas the surrounding region was seen to exclusively consist of the α-polymorph. With PLM however, quantitative information about X_c cannot be obtained as the turn of the polarization plane is affected by several parameters, such as orientation of the macromolecules, birefringence and spherulite size [27]. Hence, to determine X_c, the weld region was investigated using μFT-IR and mechanical abrasion→DSC (Figure 52), which are both techniques widely used to profile X_C [27, 109].

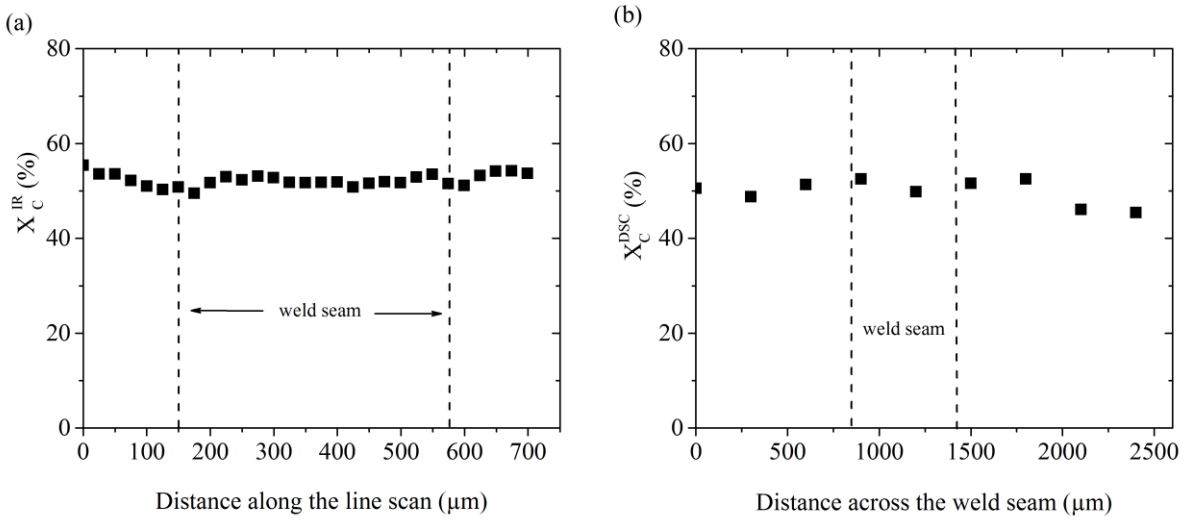

Figure 52: X_c profile across the weld measured through a) μFT-IR b) DSC

X_c does not show prominent fluctuations across the weld (Figure 52 a and b) with both techniques yielding a similar X_c profile. On a closer inspection, the X_c^{IR} profile showed small kinks across the weld seams, suggesting the possibility of a lower crystallinity in this region. However, the IR analysis is limited to a theoretical spatial resolution of ~ 10 μm, which can only be achieved by reducing the aperture size to 10 μm, which then reduces the signal intensity and necessitates longer acquisition time for gaining quantitative information. Thus, an aperture range of 100 μm with a sample thickness of 100 μm was found optimum to compromise spatial resolution and

measurement duration. This, however, averages out the information about the variation in X_c in the weld seams as only a few points across the weld seam can be considered. For the case of DSC analysis of mechanically prepared cross-sections, the amount of sample required to obtain quantitative information about X_c is around 5 mg. Taking into account the density of the polymer and the typical diameter of a DSC pan (~ 6 mm), the achievable spatial resolution is limited to ~200-300 μm. An inherent problem is to precisely localize the cuts and correlate them with the microscope image, which limits the applicability of this approach to welds.

The area marked in Figure 51 was then analyzed with Raman microscopy and the acquired spectra were fitted to study the X_c profile across the weld using the method detailed previously (Figure 53a). The profile for assessing the distribution of the crystalline domains across the welds was determined using the shift in the band position at 2954 cm^{-1} as shown in Figure 53b. The shift in the band position at 841 cm^{-1} was also profiled to study polymorphism across the weld as shown in Figure 53c.

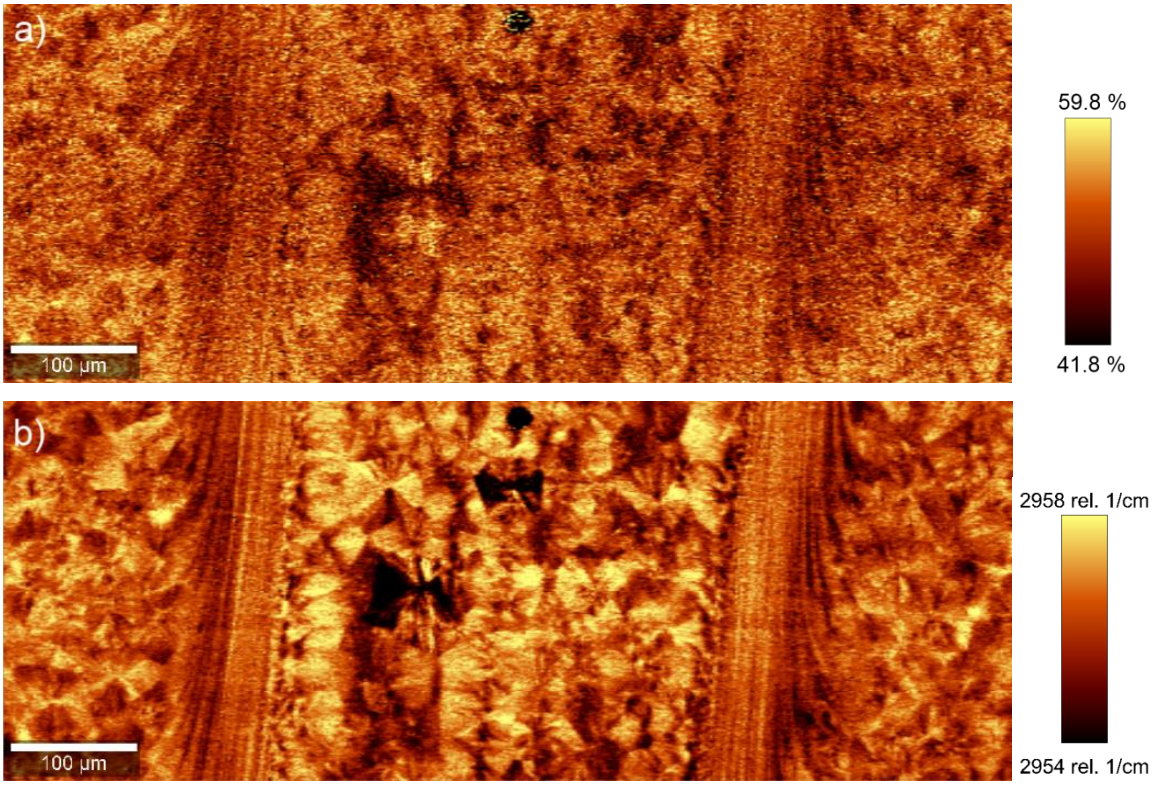

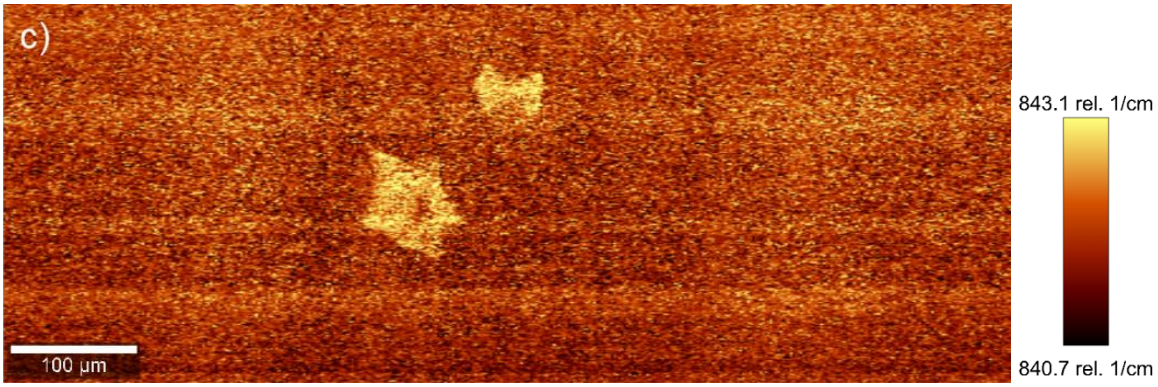

Figure 53: a) Map of X_c across the weld determined by Raman microscopy b) Crystalline domains probed by the shift in the band at 2854 cm^{-1} c) Profile of the β- polymorph determined from the band position at 841 cm^{-1}

As seen in Figure 53a, X_c determined across the weld shows a reduction in the crystallinity (~ 18 %) in the region of the weld seams compared to the surrounding PP-H plate. The reduction in X_c was observed in narrow channels along the weld seams, which in the investigations with μFT-IR and mechanical abrasion→DSC were averaged out due to the low spatial resolution. Figure 53b shows the crystalline domains, giving a better insight into the narrow channels of lower crystallinity present predominantly along the weld seams. The elongated spherulites, which are the result of the sheared melt flow, can clearly be seen, while the weld core and the surrounding plates on the other hand show distinct non distorted spherulites. Figure 53c shows the presence of the β-polymorph across the weld. Two β-spherulites can be identified in the weld core region, whereas the surrounding plates can be seen to consist exclusively of the α-polymorph.

The formation of β-spherulites is favored within a narrow range of crystallization temperature, thus the lower cooling rate in the weld core region compared to the weld seams allows a longer crystallization time, which leads to sporadic formation of β-spherulites in the weld core [128]. A higher cooling rate on the other hand favors the formation of α-spherulites [129]. This was also evident herein, where the weld seams showed an exclusively α-spherulitic structure.

After determining the variations in morphology across the welding channel between two PP-H plates, it is interesting to apply this methodology to welds between two miscible polymers, which differ in their composition and crystallization behaviour [112]. To study this, a plate of PP-H and another plate of PP-R, which are thermodynamically miscible [100], were joined by butt welding and this two material system (PP-D_W) was studied. The PLM image of PP-D_W in Figure 54a shows the weld, wherein the area marked in red was analyzed and the spectra collected were used to calculate X_c across the region (Figure 54b). The position of the bands at 2854 cm^{-1} and 841 cm^{-1} was profiled in Figure 54c) and d), respectively, and the spectral differences used to profile the distribution of the two weld components are shown in Figure 54e.

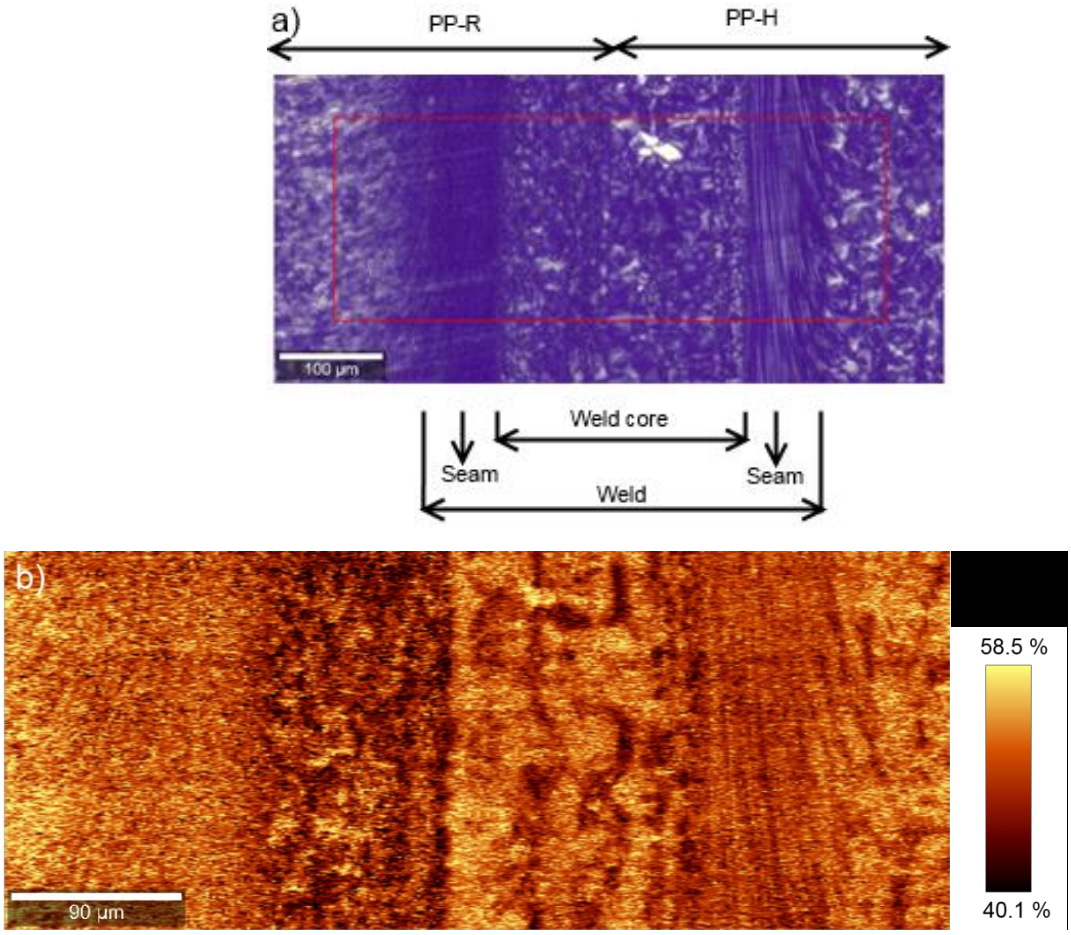

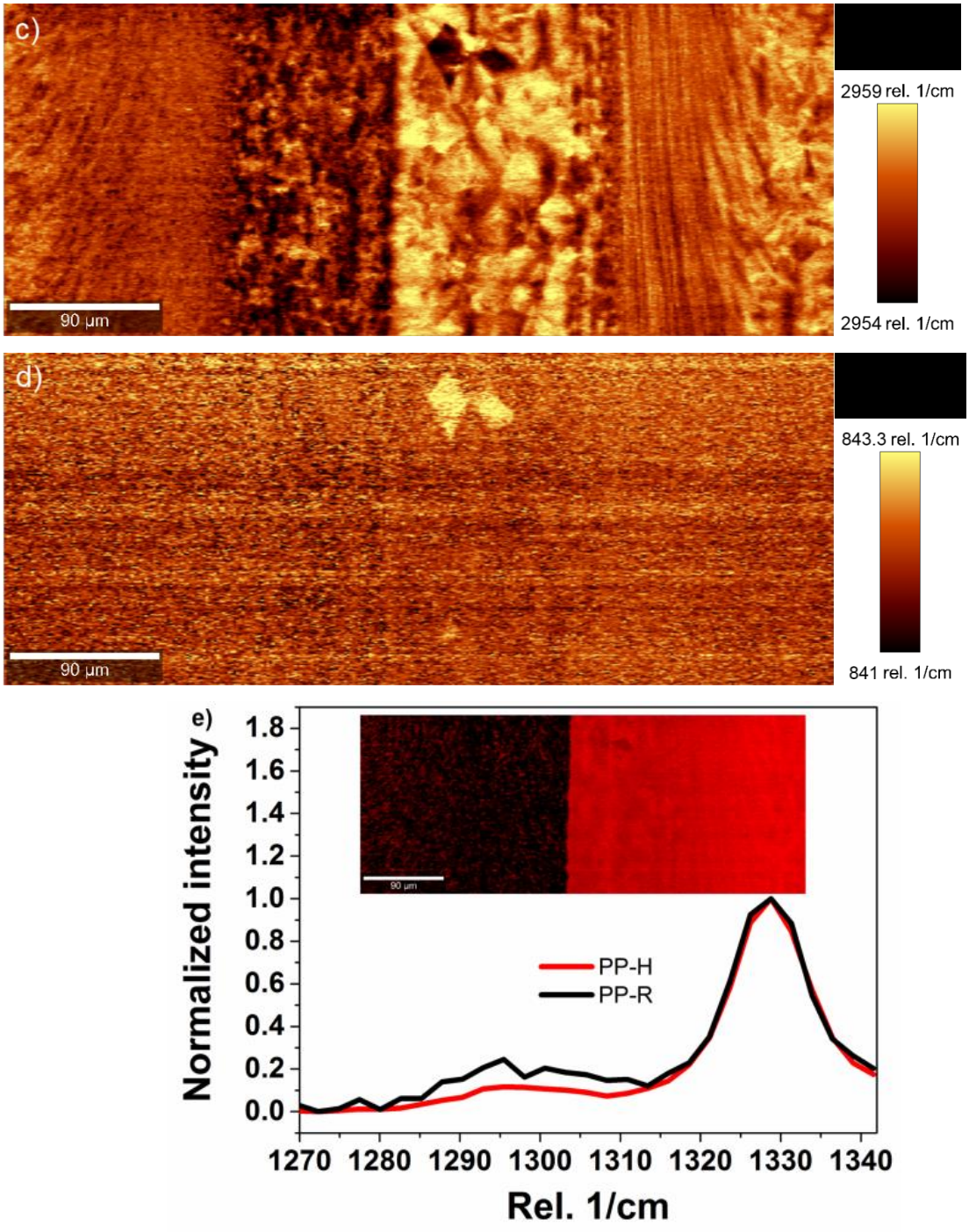

Figure 54: a) PLM image of PP-D_W b) X_c profile across the weld determined by Raman microscopy c) Crystalline domains probed by the shift in the band at 2854 cm^{-1} d) Profile of the β-polymorph determined from the band position at 841 cm^{-1} e) Distribution of PP-R and PP-H as derived from the spectra and differences in the spectrum of PP-R and PP-H.

From Figure 54b a clear border can be seen in the middle of the weld core suggesting a sharp difference in X_c of the two materials. On a closer view, the PP-H side can be further differentiated into three regions with respect to the X_c, namely the plate, the weld core and the weld seam, whereas on the PP-R side only the weld core and the area covering the weld seam and the remaining PP-R plate can be observed. This is more evident in Figure 54c, wherein the lower crystalline region in the PP-R weld core and the other regions can be clearly identified.

The differences in the chemical composition and the crystallization kinetics between PP-H and PP-R are responsible for the variations observed in the X_c. The three regions with the narrow channels of lower X_c along the seams observed on the PP-H side are consistent with the previous example of the weld between two PP-H plates. The PP-R side depicts only two areas, with the weld seams showing a similar X_c as the PP-R plate. This can be attributed to two reasons: Firstly, the incorporation of ethylene units in the polymer backbone of PP-R inhibits the process of crystallization as these units act as defects, preventing the chains from arranging themselves into an ordered crystalline structure[130, 131]. Secondly, the higher rate of cooling in the weld compared to the surrounding plates formed by injection molding also causes a reduction in X_c observed in the PP-R part of the weld core. The increase in X_c seen across the weld seam, making it similar to the X_c of the surrounding PP-R plate, can be attributed to the shear forces dominating the crystallization behavior along the weld seams [132]. The weld seams experience both the highest amount of shear and the highest rate of cooling, and in the case of PP-R the effect of the shear forces is seen to be dominating, thereby causing an increase in the X_c along the seam.

The formation of β-spherulites on the PP-H side can be easily identified in Figure 54d. The weld core region belonging to PP-R, however, did not show any β-spherulites. This is also in agreement with the crystallization behavior of PP-R, which has been known to crystallize exclusively in the α-polymorph [133].

An interesting question is that of mixing in welds, which can be studied for PP-D_W. PP-R shows a higher band intensity at 1298 cm^{-1}, which is a characteristic band in the C-

C twisting region of the Raman spectrum of polyethylene (PE) [50]. Hence, the higher intensity of this band in the spectrum of PP-R can be attributed to the presence of the ethylene units. Using these spectral differences, the distribution of the two components namely PP-H and PP-R was determined (Figure 54e). Two distinct domains for the materials are discernible and a clear boundary separating them was observed. This indicates that no intercalation of the two components takes place upon welding at the length scale accessible by Raman microscopy, inspite of them being thermodynamically miscible.

Thus, Raman microscopy has been shown capable of studying the complex morphology developing across welded materials. Variations arising in the welding channels with regard to the development of a different polymorphic structure in the weld core region and changes in the crystallinity along the weld seams due to the welding process have been studied and profiled. Using the Raman spectra of the individual components, their distribution in PP-D_W has also been determined.

6.3.1 Conclusions

Subtle differences in the Raman spectrum of the α- and β-polymorph of PP have been identified. These are manifest in the form of band shifts distinct for the specific polymorph. A new method has been developed, which can selectively ascertain the presence of the α-polymorph of PP. The band shifts in the spectra have been used to map and profile both the polymorphs distinctly. Using the method proposed by Nielsen et al., the degree of crystallinity across α- and β-spherulites has been profiled and contour plots showing the crystallinity distribution have been generated. A qualitative determination of the crystalline domains in PP plates has also been carried out using the band shifts in the Raman spectra. This method has been used to compare the crystallinity profiles for both α- and β-spherulites, and has been shown to be suitable for determining the crystalline distribution in PP.

The complex morphology generated in the welding channels as a result of butt welding of PP-H has been studied. Approaches such as mechanical abrasion→DSC and

μFT-IR are limited to their low spatial resolution where intricate variations across the weld seams are averaged out. Using Raman microscopy it could be shown that these variations in X_c were present in narrow channels along the weld seams and a gradient of ~18 % in the crystallinity could be observed. The effect of the welding on the polymorphic composition was also investigated and the cooling time in the weld core region was also found to be sufficient for the formation of the β-polymorph, which was identified and profiled using the band shifts as shown earlier. Another weld comprising of two miscible polymers, PP-R and PP-H, was investigated to study morphological variations occurring across the welds. The changes with respect to the X_c across the weld were pronounced in the PP-R weld core region, which showed a reduction in X_c and no formation of the β-polymorph was observed in this region. The part of the weld core belonging to PP-H however, showed a similar profile as observed for the previous weld sample comprising of only PP-H. Using Raman microscopy it was also possible to determine the spatial distribution of the two polymers and a clear boundary separating them was observed, indicating that no intercalation of the two components takes place upon welding.

7. Summary

Raman microscopy holds potential advantages over spectroscopic techniques like nuclear magnetic resonance and infrared spectroscopy. These include minimum sample preparation and fast measurement times. When used as an imaging technique (Raman microscopy) the spatial resolution is an additional advantage over infrared microscopy. The aspects of sample preparation and measurement times have been exploited to quantify the comonomer content in ethylene/1-olefin copolymers. In the thesis the aspect of spatial resolution has been explored for crosslinked ethylene/vinyl acetate (EVA) laminates and welds between polypropylene (PP). The results are summarized in the following:

Quantifying the comonomer content in ethylene-1-olefin copolymers is important to develop structure property↔relationships and unambiguously identify samples. Nuclear magnetic resonance spectroscopy has been widely used for this purpose, but quantitative measurements require significant amounts of sample, therefore limiting its scope for cases, where measurements are limited by the amount of sample available, such as liquid chromatography or forensics. In this study, experimental protocols for Raman spectroscopy have been developed to quantify the comonomer content in copolymers of ethylene and even numbered 1-olefins, ranging from 1-hexene to 1-octadecene. With increasing comonomer content the spectra reflect the combined effect of the decrease in ethylene content, the associated changes in the phase composition of polyethylene and the scattering from the comonomer sequences. The band ensemble characteristic for the comonomer itself cannot be used for quantification alone since the intensity of the spectra is affected by the sample focus and the spectral acquisition time. Therefore an internal standard for normalizing the intensity of the band ensemble is required, and the intensity of the band at 1295 cm^{-1} in the C-C twisting region was found to be appropriate for this purpose. This method has also been extended for determining the comonomer content of a cyclic olefin copolymer (ethylene/norbornene) having low crystallinity where the bands arising due to scattering from the comonomer sequences start dominating. Hence, the Raman spectra of copolymers of ethylene with 1-olefins ranging from 1-butene to 1-

octadecene and the cyclic norbornene have been analyzed and a method has been developed to quantify the comonomer content. Due to the minimal sample preparation, fast spectral acquisition time and its non-destructive nature, the Raman spectroscopic approach holds potential for quality control. A strong need for such a technique also exists in liquid chromatography where the amounts of sample acquired are regularly very small.

EVA resins are widely used as encapsulant for photovoltaic modules and the degree of crosslinking plays a critical role in the cell efficiency. A crucial question when developing process↔property relationships for the process of encapsulation is, how the degree of crosslinking, XC, is spatially distributed i.e., identifying inhomogeneities in the latter. Techniques such as DSC, FT-IR spectroscopy and Soxhlet extraction have been previously used for this purpose. Yet, all these approaches lack spatial resolution per se, as they are limited to bulk differences in XC, and local inhomogeneities are averaged out. In the investigations it could be shown that the sensitivity of FT-IR and DSC analysis, which is based on analyzing the amount of residual crosslinker, limits their applicability. In the present study a method based on Raman microscopy has been developed to study local variations in crosslinking of EVA laminates using model sheets crosslinked between Teflon sheets. The intensity of the respective νCH_2 vibration at 2934 cm^{-1} and the νCH_3 vibration at 2885 cm^{-1} reflect the transformation of the methyl groups of the VA comonomer into methylene bridges as a consequence of crosslinking, and thus the conversion. Yet, this information is of relative nature, and to translate it into absolute values, a calibration was carried out using a non-crosslinked EVA sample and the results from Soxhlet extraction for a highly crosslinked sample as reference points. The developed method has then been applied to study crosslinking inhomogeneities in EVA/glass laminates. In this case the quantification of crosslinking yielded significantly higher values for XC_R compared to the model EVA laminates. This can be explained by differences in the cooling pattern of the glass laminate, leading to the formation of multiple crosslinks, which are then recorded by Raman spectroscopy. This demonstrates the limitations for transferring results from a model system to the real process.

PP is widely used to produce pipes for civil engineering and construction. However processing of PP regularly leads to anisotropies induced in the melt due to shearing which in the solidified product embody themselves in the form of variations in the degree of crystallinity (X_c), the chain orientation and the polymorphic composition. The spatial variations induced in the polymer morphology have been identified and analyzed through the Raman spectrum of the α- and β-polymorph of PP. Changes in the form of band shifts distinct for the specific polymorph (β polymorph at 809 and 841 cm^{-1}) have been seen and a new method has been developed which can selectively ascertain the presence of the α polymorph in PP plates. A method for qualitatively determining the differences in the crystallinity across the spherulites has been developed using the shift in the position of the band at 2954cm^{-1}. This method has been used to compare the crystallinity profiles for both polymorphs.

PP welds show a large impact of the processing conditions on the morphology and thereby act as weak spots susceptible to rupture under application of load. Measurements using techniques such as DSC and FT-IR microscopy are limited to the high step width in measurements and intricate changes across the weld seams are averaged out. These were investigated with Raman microscopy and a gradient of ~18 % in the degree of crystallinity was seen to be present in narrow channels across the weld seams. The effect of the welding on the morphology was also investigated and the cooling time in the weld core region favored the formation of the β-polymorph, which was identified and profiled using spectral band shifts. A binate weld system of a PP homopolymer (PP-H) and a propylene copolymer with ethylene (PP-R) was investigated to study these morphological variations occurring across the welds comprising of two different materials. The crystallinity in the PP-R region of the weld core was affected more in this case and no formation of the β-polymorph was observed in the weld core region from PP-H. The weld core belonging to PP-H, however, showed a similar profile as observed for the previous sample. Using Raman microscopy it was also possible to map the spatial distribution of the two polymers and a clear boundary separating them was observed, indicating that no intercalation of the two components takes place upon welding.

The above work shows the prospects of utilizing Raman microscopy for characterization of plastic materials. The experimental protocols can be implemented in quality control of ethylene/1-olefins copolymers with regard to comonomer content. The homogeneity of crosslinking in EVA modules impacting the solar cell behavior can for the first time be determined at a μm level. The impact of the processing parameters on the morphology and crystallinity of PP welded materials have been analyzed and analytical information which could not be retrieved previously can now be accessed easily.

8. Bibliography

1. Dragaun, H.; Hubeny, H.; Muschik, H. *Journal of Polymer Science: Polymer Physics Edition* **1977,** 15, (10), 1779-1789.
2. Schuster, T.; Rode, K.; Brüll, R.; Heinemann, J.; Haupt, H. *J Appl Polym Sci* **2013,** 130, (6), 4182-4190.
3. Monami, A.; Langer, B.; Sadilek, J.; Kucera, J.; Grellmann, W. *Procedia Materials Science* **2014,** 3, (0), 276-281.
4. Van Krevelen, D. W.; Te Nijenhuis, K., *Properties of polymers: their correlation with chemical structure; their numerical estimation and prediction from additive group contributions*. Elsevier: 2009.
5. Zhang, X.; Takegoshi, K.; Hikichi, K. *Macromolecules* **1992,** 25, (9), 2336-2340.
6. Randall, J. C. *Journal of Macromolecular Science—Reviews in Macromolecular Chemistry and Physics* **1989,** 29, (2-3), 201-317.
7. Randall, J., *Polymer sequence determination: carbon-13 NMR method*. Elsevier: 2012.
8. Tiers, G.; Bovey, F. *Journal of Polymer Science Part A: General Papers* **1963,** 1, (3), 833-841.
9. Kakugo, M.; Naito, Y.; Mizunuma, K.; Miyatake, T. *Macromolecules* **1982,** 15, (4), 1150-1152.
10. Randall, J. C. *Macromolecules* **1978,** 11, (3), 592-597.
11. Cheng, H. N. *J Appl Polym Sci* **1988,** 35, (6), 1639-1650.
12. Zhou, Z.; Cong, R.; He, Y.; Paradkar, M.; Demirors, M.; Cheatham, M.; deGroot, A. W. In *Unsaturation Characterization of Polyolefins by NMR and Thermal Gradient NMR (TGNMR) with a High Temperature Cryoprobe*, Macromolecular Symposia, 2012; Wiley Online Library: 2012; pp 88-96.
13. Martin, C. R.; Rhoades, T. A.; Ferguson, J. A. *Analytical Chemistry* **1982,** 54, (9), 1639-1641.
14. Postma, A.; Davis, T. P.; Donovan, A. R.; Li, G.; Moad, G.; Mulder, R.; O'Shea, M. S. *Polymer* **2006,** 47, (6), 1899-1911.
15. Kuhn, W.; Barth, P.; Hafner, S.; Simon, G.; Schneider, H. *Macromolecules* **1994,** 27, (20), 5773-5779.

16. Chen, X.; Wudl, F.; Mal, A. K.; Shen, H.; Nutt, S. R. *Macromolecules* **2003,** 36, (6), 1802-1807.

17. Lehmann, J.; Kleinpeter, E.; Krechl, J. *Journal of inclusion phenomena and molecular recognition in chemistry* **1991,** 10, (2), 233-239.

18. Huth, J. R.; Bewley, C. A.; Clore, G. M.; Gronenborn, A. M.; Jackson, B. M.; Hinnebusch, A. G. *Protein Science* **1997,** 6, (11), 2359-2364.

19. Garigipati, R. S.; Adams, B.; Adams, J. L.; Sarkar, S. K. *The Journal of Organic Chemistry* **1996,** 61, (8), 2911-2914.

20. Look, G. C.; Holmes, C. P.; Chinn, J. P.; Gallop, M. A. *The Journal of Organic Chemistry* **1994,** 59, (25), 7588-7590.

21. Baker, M. J.; Trevisan, J.; Bassan, P.; Bhargava, R.; Butler, H. J.; Dorling, K. M.; Fielden, P. R.; Fogarty, S. W.; Fullwood, N. J.; Heys, K. A.; Hughes, C.; Lasch, P.; Martin-Hirsch, P. L.; Obinaju, B.; Sockalingum, G. D.; Sulé-Suso, J.; Strong, R. J.; Walsh, M. J.; Wood, B. R.; Gardner, P.; Martin, F. L. *Nat. Protocols* **2014,** 9, (8), 1771-1791.

22. Khoshhesab, Z. M. **2012**.

23. Fraser, R. D. B. *The Journal of Chemical Physics* **1953,** 21, (9), 1511-1515.

24. Fraser, R. D. B. *The Journal of Chemical Physics* **1958,** 28, (6), 1113-1115.

25. Beer, M. *Proceedings of the Royal Society of London. Series A. Mathematical and Physical Sciences* **1956,** 236, (1204), 136-140.

26. Brüll, R.; Maria, R.; Rode, K. *Macromolecular Chemistry and Physics* **2010,** 211, (20), 2233-2239.

27. Schuster, T.; Damodaran, S.; Rode, K.; Malz, F.; Brüll, R.; Gerets, B.; Wenzel, M.; Bastian, M. *Polymer* **2014,** 55, (7), 1724-1736.

28. Lamberti, G.; Brucato, V. *Journal of Polymer Science Part B: Polymer Physics* **2003,** 41, (9), 998-1008.

29. Raman, C. V.; Krishnan, K. S. *Nature* **1928,** 121, (3048), 501-502.

30. Wang, Q. **2013**.

31. Paradkar, R. P.; Leugers, A.; Patel, R.; Chen, X.; Meyers, G.; Lipp, E. *Encyclopedia of Analytical Chemistry*.

32. Paradkar, R.; Sakhalkar, S.; He, X.; Ellison, M. *J Appl Polym Sci* **2003,** 88, (2), 545-549.

33. Kaminsky, W. *Macromolecular Chemistry and Physics* **2008,** 209, (5), 459-466.

34. Chum, P. S.; Swogger, K. W. *Progress in Polymer Science* **2008,** 33, (8), 797-819.

35. Kaminsky, W. *Journal of Polymer Science Part A: Polymer Chemistry* **2004,** 42, (16), 3911-3921.

36. Coates, J., Interpretation of Infrared Spectra, A Practical Approach. In *Encyclopedia of Analytical Chemistry*, John Wiley & Sons, Ltd: 2000.

37. Wang, J.-S.; Matyjaszewski, K. *J Am Chem Soc* **1995,** 117, (20), 5614-5615.

38. Chum, P.; Kruper, W.; Guest, M. *Advanced Materials* **2000,** 12, (23), 1759-1767.

39. Hatfield, G. R.; Killinger, W. E.; Zeigler, R. C. *Analytical Chemistry* **1995,** 67, (17), 3082-3085.

40. Busico, V.; Cipullo, R. *Progress in Polymer Science* **2001,** 26, (3), 443-533.

41. Blitz, J. P.; McFaddin, D. C. *J Appl Polym Sci* **1994,** 51, (1), 13-20.

42. Harvey, M. C.; Ketley, A. D. *J Appl Polym Sci* **1961,** 5, (15), 247-250.

43. McNally, T.; Pötschke, P.; Halley, P.; Murphy, M.; Martin, D.; Bell, S. E.; Brennan, G. P.; Bein, D.; Lemoine, P.; Quinn, J. P. *Polymer* **2005,** 46, (19), 8222-8232.

44. Wei, L.; Jiang, W.; Goh, K.; Chen, Y. *Polymer Engineering & Science* **2014,** 54, (2), 336-344.

45. Livanova, N.; Popova, E.; Ledneva, O.; Popov, A. *International Journal of Polymeric Materials* **2000,** 47, (2-3), 279-291.

46. Yu.V. Zavgorodnev, E. A. S., G.Yu. Nikolaeva, K.A. Prokhorov,; P.P. Pashinin, L. A. N., T.M. Ushakova, E.E. Starchak,; Antipov, E. M. **2012**.

47. Gall, M.; Hendra, P.; Peacock, O.; Cudby, M.; Willis, H. *Spectrochimica Acta Part A: Molecular Spectroscopy* **1972,** 28, (8), 1485-1496.

48. Strobl, G.; Hagedorn, W. *Journal of Polymer Science: Polymer Physics Edition* **1978,** 16, (7), 1181-1193.

49. Glotin, M.; Domszy, R.; Mandelkern, L. *Journal of Polymer Science: Polymer Physics Edition* **1983,** 21, (2), 285-294.

50. Glotin, M.; Mandelkern, L. *Colloid Polym Sci* **1982,** 260, (2), 182-192.

51. Chernyshov, K.; Gen, D.; Shemouratov, Y.; Prokhorov, K.; Nikolaeva, G.; Sagitova, E.; Pashinin, P.; Kovalchuk, A.; Klyamkina, A.; Nedorezova, P. In *Raman Structural Study of Copolymers of Propylene with Ethylene and High Olefins*, Macromolecular Symposia, 2010; Wiley Online Library: 2010; pp 505-516.

52. Zavgorodnev, Y. V.; Prokhorov, K. A.; Novokshonova, L. A.; Ushakova, T. M.; Starchak, E. E.; Krasheninnikov, V. G.; Nikolaeva, G. Y.; Sagitova, E. A.; Pashinin, P. P.; Guseva, M. A.; Donfack, P.; von der Kammer, B.; Materny, A. *Laser Phys.* **2012,** 22, (4), 730-737.

53. Rull, F.; Prieto, A.; Casado, J.; Sobron, F.; Edwards, H. *Journal of Raman Spectroscopy* **1993,** 24, (8), 545-550.

54. Stuart, B. *Vibrational spectroscopy* **1996,** 10, (2), 79-87.

55. Simanke, A. G.; Galland, G. B.; Freitas, L.; da Jornada, J. A. H.; Quijada, R.; Mauler, R. S. *Polymer* **1999,** 40, (20), 5489-5495.

56. K. J, L., Encapsulant Material Requirements for Photovoltaic Modules. In *Polymers in Solar Energy Utilization*, AMERICAN CHEMICAL SOCIETY: 1983; Vol. 220, pp 367-385.

57. Dhere, N. G.; Raravikar, N. R. *Solar Energy Materials and Solar Cells* **2001,** 67, (1–4), 363-367.

58. Czanderna, A. W.; Pern, F. J. *Solar Energy Materials and Solar Cells* **1996,** 43, (2), 101-181.

59. Pern, F. J.; Glick, S. H.; Czanderna, A. W. *Renewable Energy* **1996,** 8, (1–4), 367-370.

60. Patel, R. M.; Wu, S.; Bernius, M. T.; Esseghir, M.; Mcgee, R. L.; Mazor, M. H.; Naumovitz, J., Electronic device module comprising polyolefin copolymer. In Google Patents: 2008.

61. Roos, A.; Herrmann, M.; Kalkofen, R.; Kelbch, S.; Frommont, H. J.; Bergmann, G.; Tappe, R., EVM Granulated Materials As Embedding Material For Solar Modules, Method For Its Production, Adhesive Foil As Well As A Solar Module, Method For Its Production And Production Device. In Google Patents: 2012.

62. Kempe, M. D.; Jorgensen, G. J.; Terwilliger, K. M.; McMahon, T. J.; Kennedy, C. E.; Borek, T. T. *Solar Energy Materials and Solar Cells* **2007,** 91, (4), 315-329.

63. Schlothauer, J.; Jungwirth, S.; Köhl, M.; Röder, B. *Solar Energy Materials and Solar Cells* **2012,** 102, (0), 75-85.

64. Hanoka, J. I., Methods for improving polymeric materials for use in solar cell applications. In Google Patents: 2001.

65. Hanoka, J. I.; Klemchuk, P. P., Encapsulant material for solar cell module and laminated glass applications. In Google Patents: 2001.

66. Damm, N., Verfahren zum Laminieren von im wesentlichen plattenförmigen Werkstücken. In Google Patents: 2013.

67. Kajari-Schröder, S.; Eitner, U.; Oprisoni, C.; Alshuth, T.; Köntges, M.; Brendel, R. In *Modelling the curing dynamics of ethylene-vinyl acetate*, 25th European Photovoltaic Solar Energy Conference, Valencia, Spain, 2010; 2010.

68. Lange, R. F. M.; Luo, Y.; Polo, R.; Zahnd, J. *Progress in Photovoltaics: Research and Applications* **2011,** 19, (2), 127-133.

69. Pern, F. J., Composition and method for encapsulating photovoltaic devices. In Google Patents: 2000.

70. Stark, W.; Jaunich, M. *Polym Test* **2011,** 30, (2), 236-242.

71. Bianchi, O.; Oliveira, R. V. B.; Fiorio, R.; Martins, J. D. N.; Zattera, A. J.; Canto, L. B. *Polym Test* **2008,** 27, (6), 722-729.

72. Klemchuk, P.; Ezrin, M.; Lavigne, G.; Holley, W.; Galica, J.; Agro, S. *Polymer Degradation and Stability* **1997,** 55, (3), 347-365.

73. Schubnell, M. *Photovoltaics International* **2010,** 7, 131-137.

74. Stark, W.; Jaunich, M.; Bohmeyer, W.; Lange, K. *Polym Test* **2012,** 31, (7), 904-908.

75. Chernev, B. S.; Hirschl, C.; Eder, G. C. *Applied Spectroscopy* **2013,** 67, (11), 1296-1301.

76. Theophanides, T. M., *Infrared Spectroscopy - Materials Science, Engineering and Technology*. InTech: 2012.

77. Garces, J. M.; Moll, D. J.; Bicerano, J.; Fibiger, R.; McLeod, D. G. *Advanced Materials* **2000,** 12, (23), 1835-1839.

78. Hufenbach, W.; Böhm, R.; Thieme, M.; Winkler, A.; Mäder, E.; Rausch, J.; Schade, M. *Materials & design* **2011,** 32, (3), 1468-1476.

79. Clive maier, T. C., *Polypropylene: The definitive user's guide and databook*. Plastic design library USA, 1998.

80. Natta, G.; Pino, P.; Corradini, P.; Danusso, F.; Mantica, E.; Mazzanti, G.; Moraglio, G. *J Am Chem Soc* **1955,** 77, (6), 1708-1710.

81. Bohm, L. L.; Enderle, H. F.; Fleißner, M. *Advanced Materials* **1992,** 4, (3), 234-238.

82. Karger-Kocsis, J., *Structure and Morphology*. Chapman & Hall: London, 1995; Vol. 1, p 351.

83. Addink, E.; Beintema, J. *Polymer* **1961,** 2, 185-193.

84. Jacoby, P.; Bersted, B. H.; Kissel, W. J.; Smith, C. E. *Journal of Polymer Science: Part B Polymer Physics* **1986,** 24, (3), 461-491.

85. Brown, N.; Bhattacharya, S. *Journal of Materials Science* **1985,** 20, (12), 4553-4560.

86. Tjong, S. C.; Xu, S. A. *Polymer International* **1997,** 44, (1), 95-103.

87. Tordjeman, P.; Robert, C.; Marin, G.; Gerard, P. *Eur. Phys. J. E* **2001,** 4, (4), 459-465.

88. Lotz, B.; Wittmann, J. C. *Journal of Polymer Science Part B: Polymer Physics* **1986,** 24, (7), 1541-1558.

89. Li, J. X.; Cheung, W. L.; Chan, C. M. *Polymer* **1999,** 40, (8), 2089-2102.

90. Khoury, F. *Journal of research of the National Bureau of Standards. Section A. Physics and chemistry.* **1966,** 70A, (1), 29-61.

91. Varga, J. *Journal of Material Science* **1992,** 27, (10), 2557-2579.

92. Marentette, J. M.; Brown, G. R. *Journal of Chemical Education* **1993,** 70, (6), 435.

93. Zheng, G.; Li, S.; Zhang, X.; Liu, C.; Dai, K.; Chen, J.; Li, Q.; Peng, X.; Shen, C. *Polymer International* **2011,** 60, (7), 1016-1023.

94. Lu, X.; Brown, N. *Polym Test* **1992,** 11, (4), 309-319.

95. Zhou, J.-J.; Liu, J.-G.; Yan, S.-K.; Dong, J.-Y.; Li, L.; Chan, C.-M.; Schultz, J. M. *Polymer* **2005,** 46, (12), 4077-4087.

96. Padden, F. J.; Keith, H. D. *Journal of Applied Physics* **1959,** 30, (10), 1479 - 1484.

97. García, R. A.; Carrero, A.; Martín, C.; Domínguez, C. *J Appl Polym Sci* **2011,** 121, (6), 3269-3276.

98. Mezghani, K.; Phillips, P. J. *Polymer* **1997,** 38, (23), 5725-5733.

99. The university of York, T. e. c. i. o. h. w. e. o. p. p. h.

100. Aminabhavi, T. M.; Phayde, H. T. S. *J Appl Polym Sci* **1995,** 55, (9), 1335-1352.

101. Wright, D. G. M.; Dunk, R.; Bouvart, D.; Autran, M. *Polymer* **1988,** 29, (5), 793-796.

102. Tadokoro, H.; Kobayashi, M.; Ukita, M.; Yasufuku, K.; Murahashi, S.; Torii, T. *The Journal of Chemical Physics* **1965,** 42, (4), 1432-1449.

103. Martin, J.; Bourson, P.; Dahoun, A.; Hiver, J. M. *Appl. Spectrosc.* **2009,** 63, (12), 1377-1381.

104. Nielsen, A. S.; Batchelder, D.; Pyrz, R. *Polymer* **2002,** 43, (9), 2671-2676.

105. Gatos, K. G.; Minogianni, C.; Galiotis, C. *Macromolecules* **2007,** 40, (4), 786-789.

106. Nozue, Y.; Shinohara, Y.; Ogawa, Y.; Sakurai, T.; Hori, H.; Kasahara, T.; Yamaguchi, N.; Yagi, N.; Amemiya, Y. *Macromolecules* **2007,** 40, (6), 2036-2045.

107. Nogales, A.; Hsiao, B. S.; Somani, R. H.; Srinivas, S.; Tsou, A. H.; Balta-Calleja, F. J.; Ezquerra, T. A. *Polymer* **2001,** 42, (12), 5247-5256.

108. Nogales, A.; Mitchell, G. R.; Vaughan, A. S. *Macromolecules* **2003,** 36, (13), 4898-4906.

109. Damodaran, S.; Schuster, T.; Rode, K.; Sanoria, A.; Brüll, R.; Stöhr, N. *Polymer* **2015,** 60, (0), 125-136.

110. Oliveira, M. J.; Hemsley, D. A. *British Polymer Journal* **1985,** 17, (3), 269-274.

111. Varga, J.; Ehrenstein, G. W.; Schlarb, A. K. *Express Polymer Letters* **2008,** 2, (3), 149-156.

112. Schmachtenberg, E.; Tüchert, C. *Macromolecular Materials and Engineering* **2003,** 288, (4), 291-300.

113. Stournara, M. E.; Ramprasad, R. *Journal of Materials Science* **2010,** 45, (2), 443-447.

114. Everall, N. J. *Applied Spectroscopy* **2000,** 54, (6), 773-782.

115. Leone, G.; Mauri, M.; Losio, S.; Bertini, F.; Ricci, G.; Porri, L. *Polymer Chemistry* **2014,** 5, (10), 3412-3423.

116. Hong, M.; Cui, L.; Liu, S.; Li, Y. *Macromolecules* **2012,** 45, (13), 5397-5402.

117. Hirschl, C.; Biebl–Rydlo, M.; DeBiasio, M.; Mühleisen, W.; Neumaier, L.; Scherf, W.; Oreski, G.; Eder, G.; Chernev, B.; Schwab, W.; Kraft, M. *Solar Energy Materials and Solar Cells* **2013,** 116, (0), 203-218.

118. Li, F.; Zhu, W.; Zhang, X.; Zhao, C.; Xu, M. *J Appl Polym Sci* **1999,** 71, (7), 1063-1070.

119. Li, H.-Y.; Perret-Aebi, L.-E.; Théron, R.; Ballif, C.; Luo, Y.; Lange, R. F. M. *Progress in Photovoltaics: Research and Applications* **2013,** 21, (2), 187-194.

120. Weiss, M. K. *Open Journal of Renewable Energy and Sustainable Development* **2014,** 1, (March 2014).

121. Socrates, G., *Infrared and Raman characteristic group frequencies: tables and charts*. John Wiley & Sons: 2004.

122. Ekins, S.; Sasic, S., *Pharmaceutical applications of Raman spectroscopy*. John Wiley & Sons: 2008.

123. Li-Chan, E.; Chalmers, J.; Griffiths, P., *Applications of vibrational spectroscopy in Food Science*. John Wiley & Sons: 2011; Vol. 1.

124. de la Guardia, M.; Garrigues, S., *Handbook of green analytical chemistry*. John Wiley & Sons: 2012.

125. Sergeev, O. A.; Shashkov, A. G.; Umanskii, A. S. *Journal of Engineering Physics* **1982,** 43, (6), 1375-1383.

126. Kitamura, R.; Pilon, L.; Jonasz, M. *Applied optics* **2007,** 46, (33), 8118-8133.

127. Samuels, R. J. *Journal of Polymer Science Part C: Polymer Symposia* **1967,** 20, (1), 253-284.

128. Lovinger, A. J. *Journal of Polymer Science: Polymer Physics Edition* **1983,** 21, (1), 97-110.

129. Rawashdeh, S.; Raheil, I. A. *Journal of Chemical Engineering & Process Technology* **2012,** 3, (5), 140.

130. Mileva, D.; Androsch, R.; Radusch, H.-J. *Polym. Bull.* **2008,** 61, (5), 643-654.

131. Papageorgiou, D. G.; Bikiaris, D. N.; Chrissafis, K. *Thermochimica Acta* **2012,** 543, 288-294.

132. Tribout, C.; Monasse, B.; Haudin, J.-M. *Colloid Polym Sci* **1996,** 274, (3), 197-208.

133. Varga, J.; Schulek-Tóth, F. *Journal of Thermal Analysis and Calorimetry* **1996,** 47, (4), 941-955.

Curriculum Vitae

Personal Data

Name:	Abhishek Sanoria
Address:	Schlossgartenstr. 6, 64289 Darmstadt
Date of Birth:	08.07.1989 in New Delhi, India
Telephone:	+49(0)17631573228
E-Mail:	abhisheksanoria@gmail.com
Country:	India

Work Experience

August 2013 - Present	**Position: Research Associate** **FRAUNHOFER LBF, DIVISION PLASTICS** DARMSTADT, GERMANY
Jan. 2013 – July 2013	**Position: Research Assistant** **EIGENÖSSISCHE TECHNISCHE HOCHSCHULE (ETH) ZÜRICH,** SWITZERLAND
May 2012 – July 2012	**Position: Research Assistant** **PAUL SCHERRER INSTITUTE/INKA BRÜGG,** SWITZERLAND
May 2012 – July 2012	**Position: Research Assistant**

	UNIVERSITY OF CAMBRIDGE, UNITED KINGDOM
May 2012 – July 2012	**Position: Research Assistant**
	LANXESS (RHEINCHEMIE) MANNHEIM, GERMANY

Education

August 2013 – Present	**Position: PhD Student**
	TECHNISCHE UNIVERSITY DARMSTADT, GERMANY
	CHEMISTRY DEPARTMENT
July 2008 – July 2013	**Integrated Master's Degree: Integrated 5 Years Master of Technology**
	INDIAN INSTITUTE OF TECHNOLOGY ROORKEE, (IIT ROORKEE), INDIA
	Branch: Polymer Science and Technology

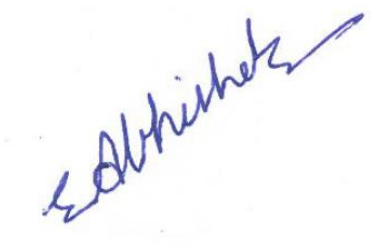

Darmstadt, 28 June 2016

Abhishek Sanoria
Schlossgartenstr. 6
64289 Darmstadt

28 June 2016

Eidesstattliche Erklärung

Affidavit

Ich erkläre hiermit an Eides Statt, dass ich meine Dissertation selbstständig und nur mit den angegebenen Hilfsmitteln angefertigt habe.

I hereby affirm that I have prepared my dissertation independently, and only with the specified resources.

Darmstadt, 28 June 2016

Abhishek Sanoria
Schlossgartenstr. 6
64289 Darmstadt

28 June 2016

Erklärung

Declaration

Ich erkläre hiermit, noch keinen Promotionsversuch unternommen zu haben.

I hereby declare that I have made no previous attempt to get a PhD.

Darmstadt, 28 June 2016